Centralized Thermal Storage Systems Model for Buildings of the Future: Development and Validation

Azeldin El-Sawi

A Thesis

In the Department

of

Building, Civil and Environmental Engineering

Presented in Partial Fulfillment of the Requirements

For the Degree of

Doctor of Philosophy (Building Engineering) at

Concordia University

Montreal, Quebec, Canada

September 2013

Concordia University

School of Graduate Studies

This is to certify that the thesis prepared

By: Azeldin El-Sawi
Entitled: Centralized Thermal Storage Systems Model for Buildings of the Future: Development and Validation

and submitted in partial fulfilment of the requirements for the degree of

Doctor of Philosophy (Building Engineering)

complies with the regulations of the University and meets the accepted standards with respect to originality and quality.

Signed by the final Examining Committee:

_____Dr. W. Ghaly, MIE, Chair

_____Dr. Mohamed El Mankibi, External-to-School

_____Dr. M. Paraschivoiu, MIE, External-to-Program

_____Dr. F. Haghighat, BCEE, Co-Supervisor

_____Dr. H. Akbari, BCEE, Co-Supervisor

_____Dr. S. Li, BCEE, Examiner

_____Dr. Z. Chen, BCEE, Examiner

Approved by _____

BCEE Department Chair or Graduate Program Director

_____ 2013_____

Dean, Faculty of Engineering and Computer Science

ABSTRACT

Centralized Thermal Storage Systems Model for Buildings of the Future: Development and Validation

Azeldin El-Sawi, Ph.D.

Concordia University, 2013

Thermal energy storage system (TES) is a promising technology for buildings heating and cooling applications. Energy storage systems have been widely used for reducing energy use from peak-demand to off-peak times. Among the various thermal storage technologies, phase change materials (PCMs) are the most commonly used approaches for storing thermal energy for buildings heating and cooling application. These materials enable buildings to store and retrieve a considerable amount of energy, typically by being integrated into structural components through a wide variety of TES techniques. A centralized energy storage system can provide a part of the heating and cooling requirements of a low-energy building. Relatively little general information pertaining to the thermal characteristics of latent heat thermal energy storage (LHTES) systems are available; further investigation is required to analyze the thermal performance of centralized LHTES systems in buildings. In this dissertation, a 3-dimensional mathematical model of a centralized LHTES system is conducted and validated for both a quasi-steady state and a transient conjugate heat transfer problem. The model is then used to carry out a parametric study to investigate the effect of

geometrical parameters, charging and discharging times and mass flow rates on the long-term system performance.

Based on the parameters that could affect the long-term system performance, artificial neural networks (ANN) are developed not only to reduce the computational time but also to relate the outlet air-temperature to the inlet air-temperature of LHTES. The database obtained from the numerical solution is first used to train the ANN and then utilized to evaluate the accuracy of the trained ANN. The developed model is then integrated with a building's mechanical ventilation system to investigate the potential improvement in occupants' thermal comfort level and energy efficiency arising from the integration of the LHTES. It was found that the temperature difference between the air as a heat transfer fluid (HTF) and the PCM melting point has a significant effect on the performances of a LHTES system. The thermal energy retrieved from the centralized LHTES system is the highest when the inlet air temperature is about 10K higher than the PCM mean melting temperature.

Acknowledgment

I would like to express my gratitude to Prof. Haghighat and Prof. Akbari for their supervision, guidance, and fruitful effort throughout this work. Their valuable comments and constructive criticism made my journey both more challenging and more rewarding during all the stages of my research. Their support and constant encouragement to purse my goals made it possible for me to overcome all the difficulties that I have faced throughout the course of this doctoral research. I would like also to thank the Public Works and Government Services Canada, and Hydro-Quebec for supporting this study.

Dedication

To my beloved parents, Mohammed and Salema, and to my family

for their continued encouragements

TABLE OF CONTENTS **Page**

NOMENCLATURE

A	porosity function
a	convection heat transfer coefficient, W/m^2. K
c	PCM's specific heat, J/kg.K
c_{eff}	effective specific heat, J/kg.K
ΔH	latent heat content
h	sensible enthalpy, J/kg
k	thermal conductivity, W/m.K
κ	permeability, m^2
f	liquid friction
g	gravity, $\mathrm{m/s}^2$
L	latent heat of phase change, J/kg
$Q_{C,Air}$	conventional ventilation load, kJ
$Q_{C,LHTES}$	ventilation load of LHTES system, kJ
$Q_{cooling}$	potential cooling load, kJ
P	effective pressure, Pa
q''	mean heat flux, W/m^2

R_a	Rayleigh number
S_b	buoyancy source term
S_h	latent heat source term
T_C	control temperature, K
T_m	mean melting temperature of the PCM, K
F_0	Fourier number, $F_0 = \alpha t / l^2$
l_c	characteristic length, m
Nu	Nusselt number
T	temperature, K
T_a	ambient air temperature, K
T_{out}	LHTES's outlet air temperature, K
t	time, s
$\underline{u}$	velocity (u, v, w), (m/s)
$\dot{V}$	volume air flow rate, m^3/s
$Temp_{LHTES}$	outlet air-temperature of the centralized LHTES system, ℃
$Time$	simulation time (hr)
$Temp_{Mixed}$	mixed air-temperature, ℃

$Temp_{out}$	ambient fresh air-temperature, ℃
$Temp_{return}$	re-circulated indoor air-temperature, ℃
ACH	air change per hour, 1/hr

Greek symbols

ϕ	expansion factor
$\rho_{(PCM)}$	density of PCM, kg/m^3
β	thermal expansion coefficient, 1/K
μ	viscosity, kg/m.s
λ	porosity
α	thermal diffusivity, m^2/s
ω	constant

Subscripts

i	initial
ref	reference
l	liquid
s	solid
PCM	phase change material
ANN	artificial neural network
CFD	computational fluid dynamics

Dimensionless Parameters

Grashof number (Gr), $R_a = g\gamma\Delta T l^3 \rho/\mu\alpha$, is the ratio of a buoyancy force to a viscous force;

Stefan number (*Ste*), $S_{te} = c\ \Delta T/L$, is the ratio of sensible heat to the latent heat;

Fourier number (F_0), $F_0 = \alpha t/l^2$, is defined as a measure of conducted heat within a body relative to stored heat;

Prandtl number (Pr), $Pr = \mu\ c/k$, is the ratio of momentum diffusivity to thermal diffusivity;

Biot number (Bi), $Bi = hl_c/k$, is the ratio of convection at the surface of the body to conduction within the body.

List of Figures

List of Tables

Chapter 1

Introduction

1.1 General

Due in part to the increasing demand for energy for heating and cooling buildings, fuel prices are continually raising, albeit gradually in many areas. Conventional cooling systems require a considerable amount of primary energy which increases building operation costs; much of that energy consumption is also linked to increased greenhouse gas (GHG) emissions. In developed nations, the building sector uses about 40% of the world-wide total energy and contributes up to 40% of annual GHG [1]. The search for new alternative energy sources has become more and more crucial. Some countries have insisted on a clear mandate to encourage new building practices that follow the standard regulation of net-zero energy buildings (NZEBs). NZEBs are defined as buildings that maintain their energy demand from sustainable sources. Clean energy can be obtained from natural resources such as sunlight, wind, geothermal sources as well as hydropower as alternatives to fossil fuel. Sustainable buildings utilize the renewable energy as a main source of energy to heat and cool spaces. However, most of the renewable energy sources are intermittent and need to be stored for use during peak demand time.

Thermal energy storage (TES) technologies play an important role in storing the excess energy from renewable sources in high production hours. Phase change materials (PCMs) are characterized by their relatively high latent heat. Due to the very small change in the volume of PCMs during the transition phase, implementing PCMs as

thermal storage and for regulated temperature applications has become a suitable option among other thermal storage mediums.

By using energy storage technologies, one can bridge the gap between supply and demand. Energy storage technologies help to reduce on-peak demand to off-peak times [1]. Reducing on-peak demand to off-peak timing can be translated to fewer power plant installations (or smaller power plants). Substantially, reducing demand takes advantage of night time free cooling ventilation TES, improving the performance and reliability of energy system [2]. As a result, the electricity supplied from power generation plants is expected to be minimized, thereby mitigating greenhouse gas emissions.

1.2 Introduction to phase change materials for thermal energy storage

Phase change materials (PCMs) can be used as a heat transfer medium to store energy. A variety of PCMs, with different thermo-physical properties, are used for latent heat thermal energy storage (LHTES) systems. Despite having some drawbacks, such as a sub-cooling effect [3], they present a high potential for various thermal storage applications. In this regard, the fundamentals of the phase change layout classification of PCMs are presented.

1.2.1 Phase change mechanism

Most pure materials have a distinct transition temperature at which the transforming process from liquid to solid takes place, and vice versa. That temperature is defined as its melting or freezing temperature, T_m. In the early stage of the melting process, the shape of the interface appears to be planar due to heat transfer by pure conduction. As time passes, the melting front starts to form a curvature shape and heat

transfer by natural convection comes to play a role when sufficient PCM melt has developed. PCMs have the ability to absorb and give off a huge amount of heat at their constant phase transition temperature at which their phase change phenomenon occurs.

Figure 1.1 illustrates the isothermal phase change process. At first, the temperature rises during the solid−phase as its sensible heat rises, until the temperature reaches the melting point. After a certain time, the heat is absorbed in the form of latent heat energy, and this stage continues until all of the solid−phase material changes completely to its liquid−phase. Next, the temperature continuously rises during the liquid−phase in the form of sensible heat. The latent heat, which is the heat stored during the phase change process, is evaluated using the enthalpy difference of the solid−liquid phase change. In this case, it is called the solid−liquid phase change enthalpy, or the melting enthalpy, or the heat of fusion. The term latent heat storage is more commonly used for those materials that have the ability of storing energy during their phase change.

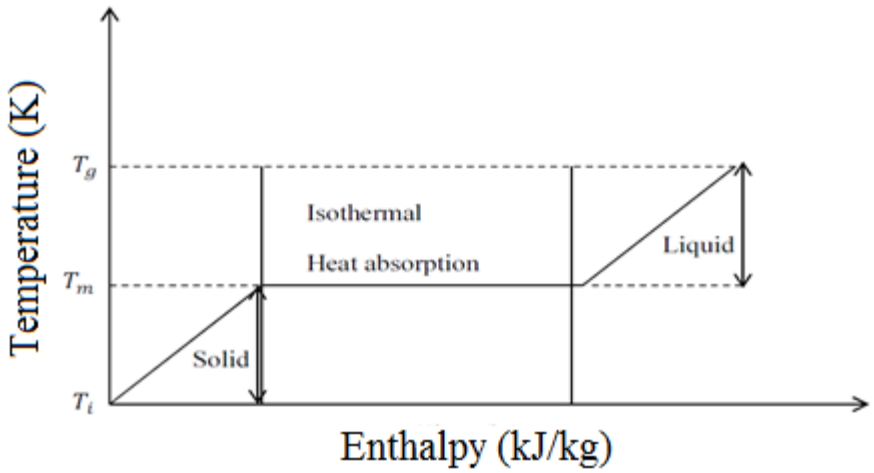

Figure 1.1 The layout of solid−liquid phase change materials [4]

1.2.2 Classification of phase change materials

PCMs can be divided into three subcategories based on their phase change state: solid−liquid, liquid−gas, and solid−gas PCMs. Practically, the solid−liquid PCMs are the best candidate to be utilized for TES in buildings [5]. According to Zalba et al. [6], the solid−liquid PCMs consist of organic, inorganic, and eutectic mixtures of PCMs, based on their constitutive materials. For instance, two types of PCMs are commonly used (i.e., paraffin wax and salt hydrate), which are categorized as organic and inorganic PCMs, respectively.

1.2.3 Latent heat thermal energy storage (LHTES)

Latent heat storage takes place when the heat energy due to a change in the phase of a storage material is absorbed or released. Phase change materials are considered as latent heat storage materials due to their release and absorption of heat at a nearly constant temperature. Sharma et al. [7] reported latent heat thermal energy storage systems can store 5-14 times more heat per unit volume than the sensible heat storage systems (i.e., water, masonry, and rock).

Over the past decade, LHTES systems and their applications have received broad attention from building researchers and practitioners, due to their relatively large heat storage capacities. The development of LHTES systems has been reviewed by Agyenim et al. [8]. They concluded that most phase change materials have low thermal conductivity. To improve the thermal conductivity, an enhancement technique is required. For example, different configurations of fins are widely used to enhance the charging/discharging of LHTES systems.

In fact, LHTES can be applied to both heating and cooling processes for a variety of applications (e.g., buildings and industries); an example of the latter is ice harvesting in the winter season in moderate climates, to be used during summer for preserving food. LHTES systems have received increasing attention, as they have a great potential to meet the comfort requirement conditions inside buildings with both more effective and more environmentally benign means of energy consumption. These systems enable practitioners and householders to reduce peak-demand use to off-demand periods. The energy consumption rate in the whole world is expected to increase by 1.4% every year from 2007 to 2020 [9]. In 2007, the building sector was reported to contribute to about 40% of global greenhouse gas emissions. There are three types of heat storage systems: sensible heat, latent heat, and thermochemical heat. Latent heat thermal storage systems are considered to be good options for buildings due to their high density storage. The most commonly used storage media (PCM) is paraffin. The thermal properties of paraffin are well-suited to building heating/cooling applications; they are commercially available, chemically stable, have relatively high fusion latent heat, self-nucleating behavior, and little super-cooling effect. Numerical models mimic these qualities to provide optimal selection of phase change temperature range. An overview of the energy saving potential and the possible peak load reduction in the built environment is presented in Table1.1.

Table 1.1 Overview of literature addressing reducing peak load and saving energy

Reference	Object configuration	Results	Analysis type
Alawadhi.[10]	Evaluated common brick wall building containing cylindrical holes filled with and without PCM in hot climate.	The heat flux was reduced by 17.55% by incorporating three cylinders of PCM at the centerline of the bricks.	Simulation
Weinlader et al.[11]	Investigated the effect of double glazing with PCM on day-lighting performance of rooms in winter and to reduce peak demand in summer.	The facade panel with PCM showed about 30% less heat loss in south oriented facades. Solar heat gains were also reduced by	Experimental

		about 50%.	
Evers et al. [12]	Study of two types of PCMs, paraffin-based and hydrated salt-based incorporated in a frame wall.	Paraffin-based PCMs reduced the average peak heat flux and the average total "daily" heat flow by up to 9.2% and 1.2% respectively. Hydrated salt-based PCMs did not exhibit any influence.	Experimental
Diaconu and Cruceru [13]	Implemented a PCM wallboard composed of three layers. External layer was PCM with high melting point; whilst the internal layer was PCM with melting point close to set point temperature of the test room. A conventional insulation layer was located in the middle layer.	Peak cooling load reduction was found (35.4%). The reduction of the total cooling load (energy savings for AC) and the value of the annual energy savings for heating were 1% and 12.8%, respectively.	Simulation
Hammou and Lacroix [14]	Performed a simulation of walls containing PCM spherical capsules with diameter 0.064m. The system under study consists of a 5 m ×5 m × 3 m room with a storage wall 0.192 m thick	The electricity consumption for space heating during four consecutive winter months was reduced by 32%.	Simulation
Kosny et al. [15]	Investigated the effect of using a multilayer attic insulation foam system with micro-encapsulated PCM on the heat flow during peak hours. Two types of PCM were tested with melting points of 26^{o}C and 32^{o}C.	The peak hour heat flow was reduced by 20%. Total heat flow through the enhanced roof was reduced by 90% compared to that of a conventional roof.	Experimental
Peippo et al. [16]	Analyzed the potential energy savings of a lightweight passive solar house with PCM (fatty acids) impregnated plasterboard.	Savings of annual energy were estimated to be 15%.	Simulation
Zhou et al. [17]	Set up a 3.9m×3.3m×2.7m test room to determine the possible energy savings during a heating season. PCM composite plates with phase change enthalpy 60kJ/kg and optimal thickness 30mm were used to line the inner walls and ceiling.	The energy savings over the entire heating season was 10% compared to without using a PCM.	Experimental
Ismail and Castro [18]	Investigated a building with brick walls and a PCM layer of 20mm lining in the ceiling of 100mm thickness to assess the reduction of energy consumed by central air conditioning.	The central air conditioning unit utilized 31% less energy.	Experimental and Simulation
Chen et al. [19]	Setup a room test with interior walls, ceiling, and floor consisting of PCM layers to investigate the heating energy savings throughout the complete winter season.	An energy savings of 10% over the winter heating season was achieved.	Experimental
Athienitis et al. [20]	Studied the integration of PCM into building envelope components for	The total heating load was reduced by approximately 15%.	Experimental and Simulation

	thermal storage in a passive solar test-room. Gypsum board impregnated with a phase change material was used. The PCM gypsum board contained about 25% butyl stearate by weight		
Stetiu and Feustel[21]	Simulated one room in an office building, with PCM wallboard interior walls and mechanical ventilation at night. The mass concentration of the PCM, paraffin, accounted for 20% of the wallboard by weight.	The peak cooling load was reduced by 28%.	Simulation
Boehm and Halford [22]	Modeling of a three-layer sandwich panel with external and internal layers composed of insulation and a middle layer of PCM.	The maximum reduction of peak load was found to be 19-57% compared to a panel composed only of insulation.	Simulation
Koschenz and Lehmann [23]	Set up two1.83m×1.83m×1.22m test rooms in order to determine the amount of heat flux that crossed through the walls.	The average reduction of the wall heat flux was found to be 11% to 21% for 10% PCM concentration, and from 1% to 15% for 20% PCM concentration. Wall orientation, weather, and climate conditions significantly affected the heat flux reduction rate. The cooling load was reduced by 8.6% to 10.8% over a daily basis.	Experimental

LHTES is a promising technology for building heating and cooling. A centralized LHTES system is a hybrid phase change material (PCM) closed system based on a multi-fin heat sink. The PCM is used as a heat transfer medium to store and release energy. A variety of PCMs, with different thermo-physical properties, are used for LHTES systems. For instance, two types of PCMs that are commonly used are paraffin wax and salt hydrate, which are categorized as organic and inorganic PCMs, respectively

1.3 Objectives

Considering the limitations in the literature, the objectives accomplished in this dissertation is summarized below:

- To develop and validate a 3-D numerical model of a LHTES system and to study its thermal behavior under various conditions. To carry out a parametric study to investigate the impact of geometrical parameters, PCM type, the HTF inlet air-temperature, the HTF mass flow rate, and the discharging time on the system thermal performance.
- To develop an Artificial Neural Network (ANN) to be utilized to predict the long-term performance of the centralized LHTES system.
- To investigate the long-term peak-demand reduction performance of the centralized LHTES system. A control strategy is applied to manage the charging and discharging processes. The centralized LHTES system is integrated with a mechanical ventilation system combined with night-time ventilation.

1.4 Organization of the dissertation

In addition to this introductory Chapter 1, Chapter 2 presents a comprehensive literature survey regarding the LHTES system and their features. The methodology used to solve the heat transfer and phase change phenomena is provided in Chapter 3. The development of the numerical model and its validation are elaborated in Chapter 4.

Chapter 5 presents the modeling of a centralized latent heat thermal energy storage system and its potential benefits in energy efficiency, load shifting, and in emergency heating/cooling load systems. A three-dimensional heat transfer model of a LHTES system is conducted to investigate the quasi-steady state and the transient heat transfer of phase change materials (PCMs). Through a parametric study, the effect of the

temperature, the PCM phase change temperature range, and the temperature difference of the incoming air and PCM melting temperature on PCM thermal performance is undertaken.

Chapter 6 presents an assessment and prediction of the thermal performance of a centralized latent heat thermal energy storage system utilizing an artificial neural network. A validated computational fluid dynamics simulation tool is used to study the long term performance of a centralized latent heat thermal energy storage (LHTES) system.

Integrating a centralized LHTES system into an energy building model is elaborated in Chapter 7. Finally, the conclusions, contributions, and recommendations for potential future work are summarized in Chapter 8.

Chapter 2

Literature Review

This section presents a comprehensive review of the previous studies regarding the integration of thermal energy storage in buildings. Considerable attention is paid to interpreting different aspects of heat transfer enhancement between PCMs and airflow. The most influential parameters of LHTES systems are reviewed, including the related experimental work. Additionally, specific design parameters and their characteristics are evaluated.

2.1 Heat transfer between air and PCMs

LHTES systems have been extensively examined in terms of their effective thermal performance both numerically and experimentally [24]. Despite the very low thermal conductivity of PCMs, which is considered an inherent disadvantage, considerable efforts have been made to improve their performance. Different techniques have been used to enhance the performance of these systems using extended surfaces, as reported by Jegadheeswaran and Pohekar [25], Fan and Khodadadi [26], and Baby and Balaji [27]. Two popular techniques are the use of fins with cooling storage units [28-34] and the application of multiple PCM methods [35]. Heat pipes [36, 37], and porous matrix of graphite [38, 39] have been embedded in PCMs to improve the thermal performance of LHTES systems. PCMs have also been combined with granules formed by mixing foamed glass beads and paraffin wax together to speed up melting and freezing processes [40]. The charging time was reduced by approximately 60% when aluminum

powder was added to the paraffin wax [41]. Aluminum foil has been used to increase the solidification rate under a boundary condition of constant heat flux in a shell-and-tube cold storage unit [42].

Mosaffa et al. [43] studied an isothermal solidification process for a rectangular finned thermal storage unit both numerically and analytically and predicted the liquid−solid location and the temperature distribution of a fin. They reported that a minor error was found when the one-dimensional analytical solution was used, and that the solidification time reduces with decreasing the temperature of the heat transfer fluid (HTF). Jeon et al.[44] reported the development of a PCM thermal energy storage system combined with radiant floor heating systems to reduce the building energy consumption. They showed that a proper melting point of PCMs plays a significant role in optimizing PCM performance. Due to the complexity of temperature distribution in the radiant heating system when combined with other means of heating, PCM technology needs to be experimentally examined.

2.2 Effect of PCM container design

The main advantages of PCM encapsulation are: providing a large heat transfer surface area, reducing PCM reactivity towards the outside environment, and controlling the changes in the storage materials' volume wherever phase change occurs [45]. An extremely challenging task is the optimal design of the container to reduce the solidification time and thereby improve free-cooling efficiency. Different configurations of PCM containers such as cylindrical, flat plate, spherical, and shell-tube encapsulation have been designed and examined. A cylindrical LHTES with a packed bed of spherical

encapsulated PCM was investigated for six cities across Europe with different climatic conditions [46]. In their numerical analyses, the effective heat capacity of a PCM, $\mathbf{C}_{\mathrm{eff(PCM)}}$, was approximated as an exponential function. The latent heat of the PCM in all cases was equal to 142kJ/kg. They found that the optimum PCM has a melting temperature equal to the average ambient air temperature, in the hottest month, for a phase change temperature range of 12K. Accordingly, the potential of free-cooling is proportional to the average daily amplitude of the ambient air temperature fluctuations. As a result, the optimal size of the LHTES for free cooling of buildings lies in between 1 and 1.5kg of PCM per $1m^3/h$ of fresh ventilation air.

Encapsulated PCM in a container of a prototype storage unit made of galvanized steel (0.5m×0.5m×0.01m) was experimentally examined by Waqas and Kumar [47] to investigate the influence of airflow rate and of inlet air temperature on thermal performance. They reported that a higher airflow rate causes a higher heat exchange during the solidification process. A flat slab LHTES unit for cooling applications with convective boundary conditions was analyzed to estimate the heat transfer between the plate and the air gap [48-50]. These studies indicated that enlargement of the air gap or of PCM slab thickness can lead to lower heat transfer rates. The performance of floor supply air conditioning system, using PCM was experimentally investigated to reduce the cooling load of an office building [40]. A floor supply air conditioning system was combined with a 30mm thick packed bed of granular PCM RT20 with a transition temperature phase in the range of 17-22℃. This study concluded that 89% of daily cooling needs can be shifted by storing the coolness during the night for a small experimental system with a floor area of $0.5m^2$.

Several experimental and numerical investigations of the melting and solidification processes have been performed on rectangular enclosures [41, 51-55], and on finned enclosures [28, 29, 31-34, 37, 43, 56]. Two different prototypes of PCM-air real-scale heat exchangers were experimentally evaluated by Lazaro et al. [57] to examine their potential to be used for free cooling application. The first prototype was constituted vertically of aluminum pouches filled with an inorganic PCM and was tested by changing the thickness of the PCM, while the second one had aluminum panels filled with organic PCM, assessed by passing different airflow rates. It was observed that the second prototype has more potential to be utilized for free cooling; the first prototype suffered a leakage problem due to the increase of PCM thickness. The role of buoyancy-driven convection during the constrained melting of PCMs inside a spherical capsule was computationally investigated using the commercially available Fluent code [58]. Their result showed the formation of a thermal stratification of the molten liquid on the top of the sphere due to the density differences among the layers of liquid. A system consisting of PCM in thin flat containers with air passed through gaps between them is proposed by Vakilaltojjar and Saman [59]. They determined that the system performance could be improved by utilizing smaller air gaps and thinner PCM slabs.

2.3 Specific design parameters and evaluation characteristics

A review of PCM-thermal storage systems is presented by Zalba et al. [60], listing all the common types of PCM that are used in building applications. Different proposed mathematical models for the analysis of PCM problems in conjunction with the numerical methods for solving them was reviewed by Dutil et al. [61]. Various

parametric studies have been carried out to study the impact of selected parameters on the thermal performance of a TES. The size of a cylindrical LHTES was optimized on the basis of (i) the calculated cooling degree-hours; and (ii) the optimal PCM melting temperature [46]. The optimal melting point was found to be higher than the average three summer months ambient air temperature by 2℃. Waqas and Kumar [47] examined the potential of nightly free cooling in different climatic locations, and found that lower ambient temperatures and higher air flow rates are the influencing factors. Tay et al. [62] introduced the heat exchanger effectiveness as an applicable parameter to describe the thermal process until the HTF temperature reaches the PCM temperature. The effectiveness of LHTES system can be defined as the ratio of the heat retrieved over the maximum heat that can be discharged. Therefore, the maximum effectiveness occurs when the outlet temperature of HTF is equal to the PCM temperature. The discharging process of a cool TES system was reported by Wu et al. [63]. They concluded that the released cooling energy increases when the HTF has either higher inlet temperature or lower volume flow rate. Waqas and Kumar [64] evaluated slabs of PCM (SP27) with a latent heat of 190kJ/kg, melting point 27℃, and mass of 10kg during the summer months in a hot-dry climate. These slabs were encapsulated in a storage unit and supplied with an airflow rate of 15-20m^3/hr. They demonstrated that the melting point of a PCM should be equal to the comfort temperature of the hottest summer month to maximize thermal performance of the storage unit. Dolado et al. [65] simulated a real-scale TES PCM-air heat exchanger system to investigate the heat transfer between the air and a slab made of macro-encapsulated phase change materials. They observed that melting or solidification time decreases when the air gap between the slabs is narrowed.

A flat plate configuration with an airflow channel width of 15mm was examined by Raj and Velraj [35]. Their simulation indicated that a charging time of 4hr and a discharging time of 6hr was found to be a suitable period for free cooling. Night ventilation with fatty acid PCM embedded in a Packed Bed Storage (PBS) system for an office building (3.3m×3m×3m) was modeled and experimentally studied by Kang et al. [66]. The PBS system was 2.4m×3m×0.12m, placed in the space in the suspended ceiling. Altogether, about 2000 PCM capsules with a total mass of 150kg and convective heat transfer coefficient of about 12-19$Wm^{-1o}C^{-1}$ were used. They concluded that night ventilation of a PBS system has a good potential to improve the thermal comfort of the indoor environment.

The effect of cooling and heating rates on the accuracy of the experimental measurement of the apparent heat capacity for RT20 paraffin was assessed by Arkar and Medved [67]. They used a Differential Scanning Calorimetric (DSC) test and presented the results for cylindrical LHTES systems. The numerical predictions showed a good agreement with the experimental investigations for a 0.1K/min cooling rate and a 0.2K/min heating rate. Experimental investigations of the melting process have been performed in a rectangular enclosure [54]. That study was limited to covering the following ranges: Raleigh Number, Ra = 2.02×10^7- 2.61×10^7, the product of Fourier and Stefan number (*Ste*), *Ste* F_0 = 0.001-0.125, and the Prandtl number, Pr = 804-1055. The critical Rayleigh number that indicates the switch from conduction to convection was found to be in the range of 7.869×10^6- 3.237×10^7.

The effect of an expected unstable flow structure on the waviness and enhanced melting of the solid PCM at the bottom of a transparent glass sphere filled with Paraffin

wax n-octadecane was examined by Tan et al. [58]. They reported that computational results closely matched the thermocouple readings at the bottom of the sphere and clearly predict a chaotic flow structure. They presented and analyzed the results obtained from the PCM freezing process for the recovery and storage of cryogenic gas cold energy in dimensionless forms, such as Biot number and the Stefan number. Tan et al. [68] reported that Biot number exerted the most influence on the frozen layer growth performance. A correlation of Nusselt number as a function of Rayleigh number was developed by Stritih [31] to determine the convective heat transfer coefficient for finned storage units.

A steady state analysis was carried out to assess the pressure drop across a PCM module heat exchanger by Raj and Velraj [69]. They observed that the increase in frontal velocity up to 2m/s has a considerable effect on boosting the surface heat transfer coefficient and reducing the solidification time. Shatikian et al. [32] numerically studied the melting process of paraffin placed in the partition of a small-scale unit. The simulation was conducted for different fin size thicknesses ranging from 0.15-1.2mm. The system was heated at its base to 6-24℃ above the mean melting PCM temperature. They reported that by normalizing the results in the term of Stefan, Fourier, and Rayleigh numbers can give more information about the melting phenomenon of a PCM.

In a study of a thermal energy storage/release system employing PCM conducted by Ye et al. [34], fins were set higher than the PCM, which filled about 85% of the allowed space. Meanwhile, the air filled 15% of the total enclosed space. A PCM layer of width W_{pcm}=4mm and vertical fins of height H_f=12mm and width W_f=1.6mm were considered. The results showed that temperature differences had a pronounced influence on the performance of energy storage when temperature differences were less than 20℃.

Mesalhy et al. [70] studied the effect of decreasing porosity on enhancing the melting process. They noted that the effective thermal conductivity could either raise or inhibit the liquid phase motion that naturally enhances the melting process.

Analysis of the thermal performance of a phase change thermal storage unit (PCTSU) showed that the HTF mass flow rate has a significant influence on the PCM melting process [71]. That analysis showed that the higher HTF mass flow rate leads to faster heat exchange with PCM parallel slabs, and that changing the slab geometry does not show any pronounced effect on the exchange heat transfer.

Colella et al. [72] performed a numerical analysis of a medium-scale latent energy storage unit for district heating systems, using a shell-and-tube LHTES unit filled with technical grade paraffin-graphite composite as phase change materials and water as a heat transfer fluid. Their 2-D numerical model in axial and radial coordinates was developed to solve the momentum and energy equations simultaneously, based on an enthalpy-porosity approach. The model domain had a structured mesh of 15×15 of vertical HTF pipes submerged in paraffin RT100 with solidification temperature of 99℃. The storage unit was subjected to heat flow in a range from 130kW to 400kW. They designed a storage unit to transfer heat from the district to the building heating networks. The simulation results were presented as a function of Re and Ste numbers. The impact of natural convection during the melting process was considered to be negligible. The simulations were performed for three different scenarios of HTF mass flow rates, 0.02kg/s, 0.01kg/s and 0.005kg/s, all started at the liquid phase of the PCM with 120℃ as a maximum fluid temperature in the primary distinct heating network. Colella et al. reported that combining the storage unit with the building heating network stores more

energy than combining it with the primary district heating network. The thermal conductivity of the PCM was improved by adding graphite with a 15% volume fraction, which was found to be suitable for the specific applications. However, the numerical mode was not validated because no data was available in the literature for similar.

2.4 Free ventilation with LHTES systems for building of future applications

Ubinas et al. [73] reviewed the studies that are pertinent to enhancing the thermal mass of lightweight buildings using phase change materials. They clearly showed that heavyweight buildings have a high thermal mass to offset the variations of daily temperature, while lightweight buildings do not have a sufficient thermal mass to balance their demand for energy. Using a control strategy combined with getting the full benefits from night ventilation during summer becomes very attractive for integrating PCMs into lightweight buildings. The PCM performance is affected by the building characteristics and the local climate.

Stritih and Butala [74] conducted experimental work to investigate the thermal performance of PCM storage unit. The objective was to lower the volume flow rate of air supplied and to extract the most possible latent heat, as shown in Figure 2.1. However, a high volume flow rate was recommended for ventilating purposes. A storage unit can save energy as it is used to cool down a building space in conjunction with a conventional cooling system. The heat transfer problem was simply formulated using two-dimensional transient diffusion equation. Stritih and Butala [75] reported that the comparison between the numerical model and the measurement data showed a discrepancy in the transient range and had a good agreement at the steady-state range at selected simulation times, as

shown in Figure 2.2. Additionally, the airflow rate and the specific heat were considered constant throughout the simulation time, as in experimental observations. Typically, the value of the specific heat was provided from DSC measurements at a heating rate of 0.1K/min.

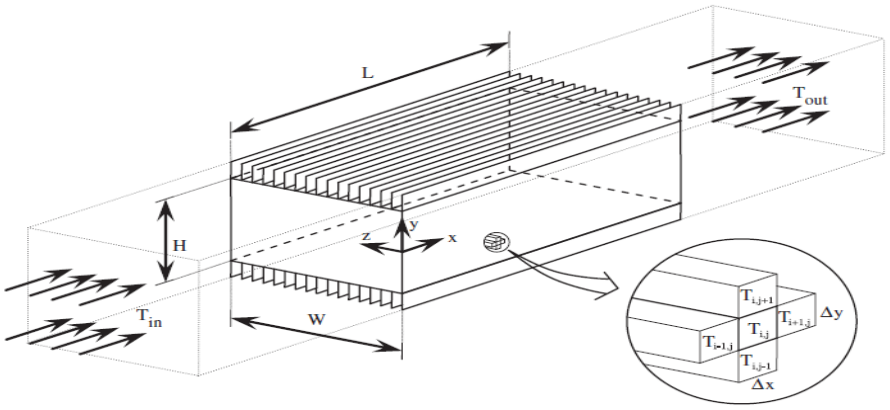

Figure 2.1 Cold thermal storage with PCM [74]

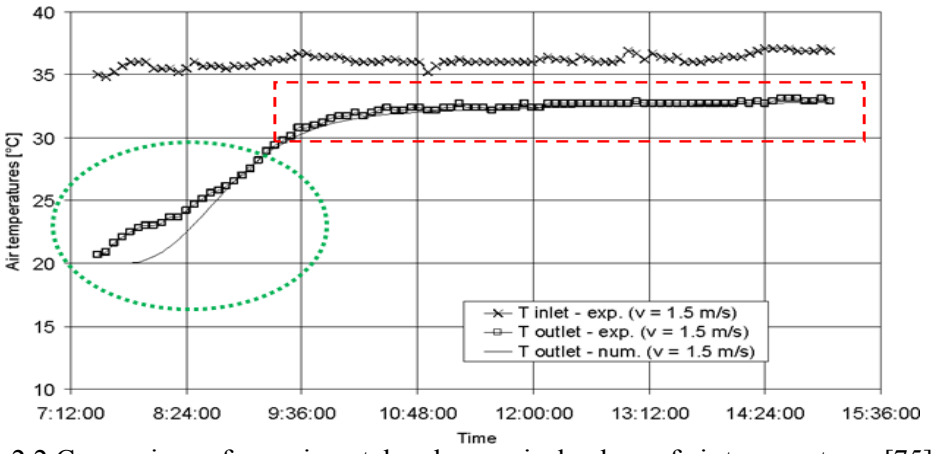

Figure 2.2 Comparison of experimental and numerical values of air temperatures [75]

Yam et al. [76] proposed a model to study a naturally ventilated building thermal mass coupled with the non-linear relation between the airflow rate and the indoor air temperature. They showed that when working with natural ventilation for thermal mass inside buildings, two factors need to be considered. First, the ventilation airflow rate,

which was not constant in their situation due to temporary ventilation needs, and second, the natural ventilation flow rate, which was affected by changes in the wind and added thermal forces. They reported that the ventilation air flow rate depends on the temperature difference between indoor and outdoor air, and so the ventilation air flow rate and indoor air temperature are coupled in non-linear relation.

Costa et al. [77] developed a theoretical model for assessing the thermal behavior of a one-dimensional latent heat energy storage system, including conduction and convection heat transfer modes without fins, and of a two-dimensional diffusion model modified by taking into account only conduction mode in fins, as shown in Figure 2.3. A fully implicit finite difference method and an enthalpy formulation were used to solve the heat transfer PCM problem. However, the thermo-physical properties of the PCM and fin material were considered to be constant and not a function of temperature. For simplicity, the convective term in the energy equation was ignored. They showed that the melted fraction rate was increased by four times when fin was applied. The rate of heat transfer was thus enhanced due to the improved performance of PCM thermal conductance.

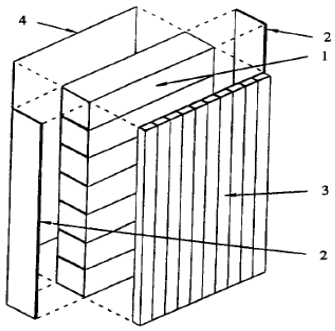

Figure 2.3 Schematic of latent heat storage system. 1) aluminum PCM containers; 2) transparent polycarbonate envelope; 3) tubes for fluid flow; and 4) wall of the electric heater [77]

Henze and Humphrey [33] numerically and experimentally investigated the thermal performance of a finned PCM device, shown in Figure 2.4. They developed a simplified numerical model, assuming that the problem solved as a quasi-linear, and transient. The following assumptions were made: the fins were modeled to be thin, and hence their temperature was a function of the x −direction, the conduction heat transfer mode in solid phase was neglected because the operating initial temperature of the storage cell was set equal to the melting temperature of the PCM, only the latent heat of fusion was taken into account, and all the solid and liquid phase thermo-physical properties were considered to be constant. Heat transfer by natural convection from the fins to the PCM was assumed, due to instabilities created above the fins and the surface of solid−liquid interface. *Nu* was correlated to be used over all of the parameter range studied in the experiment. To verify the accuracy of the model, the model predictions were compared with model the experimental data: the results were in fairly good agreement. Their results indicated that the rate of heat transfer could be further enhanced if the space between fins was decreased. They also showed that the melted fraction and shape of a liquid−solid interface could be represented as a function of time.

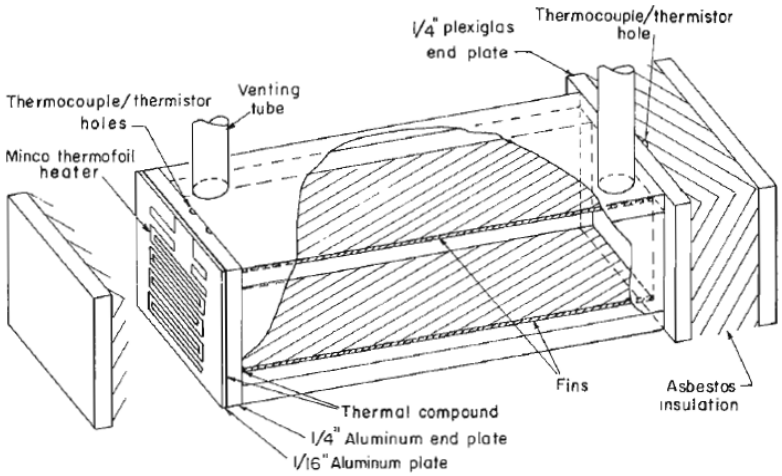

Figure 2.4 Experimental test section [33]

In a cooling system studied by Zalba et al. [78], the main influencing parameters such as the ratio of energy/volume in encapsulates, the load/unload rate of the storage unit, and the installation cost were determined experimentally for acceptable solutions of an engineering problem design. The results showed that the most influential parameters of the solidification process are the inlet air temperature, the thickness of the encapsulation, and the air flow rate. In the melting process, the inlet air temperature has a prevailing effect. Based on the data obtained from these experiments, empirical formulations were established to determine the solidification and the melting times. The selected PCMs for this full-scale experiment were RT25 and C22, and the encapsulation material was Polyethylene High-Density (PE-HD). However, enhancing the heat transfer between the PCM and the HTF was required, which allowed the PCM melting point to be in the desirable range of 22-23℃. A fan with variable speed was also required.

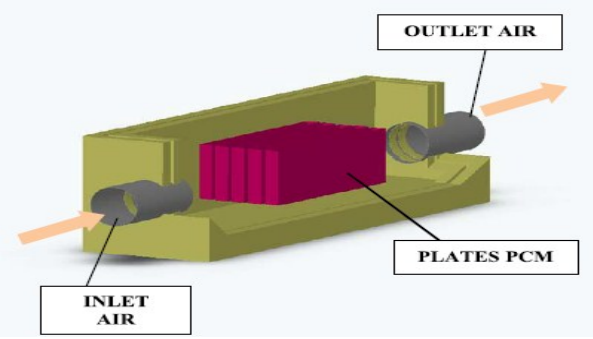

Figure 2.5 Configuration of the TES device [78]

The free cooling of a low-energy building using a LHTES system integrated into a mechanical ventilation system was studied by Arkar and Medved [79] as illustrated in Figure 2.6. Spherical encapsulated of RT20 paraffin (PCM) was filled in the LHTES system's cylindrical device. To obtain the optimum phase-change temperature a periodic inlet ambient-air temperature was used as an input parameter to a developed numerical packed-bed model. A temperature-response function was deployed, which means that the outlet air-temperature of the LHTES system was approximately formed as Fourier functions and then integrated into the TRNSYS building thermal response model. The distributions of the air axial velocity and of the bed porosity were considered uniform and applied into coupled energy equations for the air and the PCM. A specific air-flow rate and a bed porosity were chosen to be $0.7m^3/hr$ and 0.38, respectively. Intensive night-time cross ventilation (with an air-change rate of $5\ h^{-1}$) was required. This study indicated that a PCM with a melting temperature between 20 and 22℃ has a significant potential to be implemented for free cooling in areas with a continental climate (cold in winter and hot in summer). A LHTES system with $6.4kg/m^2$ floor area of PCM, with a diameter of 25mm and storage aspect ratio L/D of 1.5 can achieve a desirable level of thermal comfort during the summer period for a building model space of $430m^3$. The spherical

capsules of PCM were handled as a continuous medium despite the physical problem that it was constituted of several individual parts.

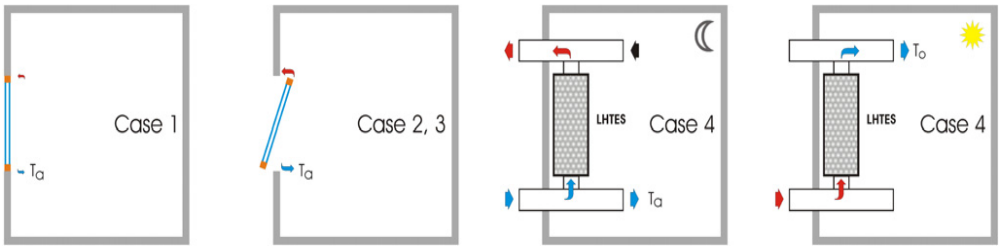

Figure 2.6 Different natural and free cooling ventilation modes [79]

Arkar et al. [80] investigated the application of using free cooling principles by integrating two cylindrical LHTES systems into a mechanical ventilation system for heavyweight and lightweight low energy buildings. One was utilized for cooling the fresh supply air and the other for cooling the re-circulated indoor air. The LHTES systems contain spherical capsules filled with PCM (paraffinRT20) as shown in Figure 2.7. The LHTES system's outlet air-temperature was manipulated to be in the Fourier series form and then modeled in TRNSYS to calculate the building's thermal response. The temperature response functions considered the storage size, the air flow rates, and the PCM's thermal properties. A verified numerical model was used to describe the heat transfer equations for the air and the PCM. Arkar et al. reported that the free cooling technique has the potential to minimize the size of mechanical ventilation systems.

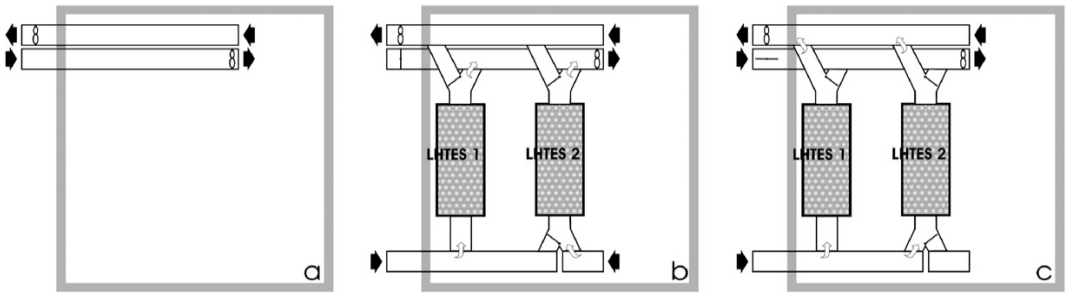

Figure 2.7 Different mechanical ventilation modes. (a) Mechanical ventilation or night cooling, (b) free cooling daytime operation, (c) free cooling night-time operation [80]

Lamberg et al. [81] performed a validation of the numerical results predicted by FEMLAB with the experimental data for a cold storage unit containing paraffin as PCM. Two internal fins were embedded in the storage unit as shown in Figure 2.8. The energy equation was approximated by replacing the velocity convective term with a correlated formula for the convection heat transfer coefficient during the melting process. The continuity and momentum equations were ignored. FEMLAB software was used to couple non-linear and time-dependent partial differential equations. They reported that the effective heat capacity method was the most efficient way to simulate the melting and solidification processes for a small (2°C) phase changing range.

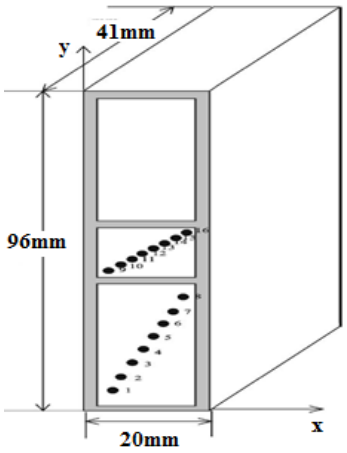

Figure 2.8 Storage with fins [81]

2.5 Summary and conclusion

The melting and solidification characterization processes have mainly been investigated for small-scale plate-fin units or partitioned systems. However, there are a few studies of an enhanced LHTES system with extended surfaces penetrating into PCM medium. One- or two-dimensional transient diffusion energy models have often been used for the characterization of PCM heat transfer behavior, which may not be accurate enough to describe this phenomenon. Also, the thermo-physical properties of phase change materials (PCMs) exhibit nonlinear behavior with temperature changes. In addition, the PCM properties that are provided in the literature are not sufficient to be used in nonlinear PCM heat transfer problems.

Due to the complexity of the governing equations involved in the phase change problem, most of the available numerical solutions have been modeled in one- or two-dimensional systems to simulate the characterization of the charging and/or discharging processes for almost one day under constant boundary conditions. Therefore, an extensive numerical simulation needs to be carried out to study the long-term performance of a centralized LHTES system under realistic conditions.

Chapter 3

Modelling of LHTES

This chapter provides a general overview of the modeling of phase change materials. Numerical methods to solve phase change problems are presented. More focus is placed on the developing and modeling a centralized LHTES system, including the governing equations, boundary and initial conditions that describe the nature of phase change behavior. The integration of this centralized LHTES system model into a building model is thoroughly described.

3.1 Modelling phase change material

Heat transfer in PCM storage is a transient, non-linear phenomenon with a moving solid–liquid interface, generally referred to as the "moving boundary" problem. Due to the non-linear nature of such a problem, numerical analysis in general is the best option to get a proper solution [61, 81]. An enthalpy formulation for the convection/diffusion phase change was developed by Voller et al. [82]. They concluded that their method combined with the Darcy source technique for velocity correction would be suitable for existing heat-transfer numerical methods. The definitions of the source items need to be added to the heat and momentum equations. Voller et al.[83] developed a new source-based method for modeling solidification phase change systems. This method updates the liquid fraction step-by-step by implementing the linearization of the discretized source term. As a result, it can achieve more accurate computation.

The difficulty in modelling the phase change problem is due to its inherent non-linear nature at moving interfaces where the absorbed or released latent heat is dominated by the displacement rate at the boundary. The equation below, known as the Stephan condition, describes this process:

$$\lambda\rho\left(\frac{ds(t)}{dt}\right) = k_s\left(\frac{\delta T_s}{\delta t}\right) - k_l\left(\frac{\delta T_l}{\delta t}\right) \tag{3.1}$$

where λ is the latent heat of fusion, ρ is the density, $s(t)$ is the surface position, k is the thermal conductivity, t is the time, and T is the temperature. Subscripts s, l imply the solid and liquid phases, respectively.

Many simulation models have been developed in the past decade, such as a fast implicit finite-difference method for the analysis of phase change problems. Voller et al. [84] introduced a rapid implicit solution technique for the enthalpy formulation of conduction-controlled phase change problems. Their method was developed to solve the nonlinear equations resulting from implicit time integrations of the enthalpy formulation. A major advantage of new source scheme was to update the liquid fraction from the sensible enthalpy field. The technique was compatible with a number of commercial codes, where the solvers are based on TDMA (tri-diagonal matrix algorithm) line-by-line algorithms to return the exact sensible enthalpy field. However, non-isothermal phase change problems are neglected. Shamsundar and Rooz [85] reported that the Gauss-Seidel point-by-point method provided a straightforward way in which an implicit solution of a phase change problem can be achieved. Voller [86] developed the enthalpy method to analyse one-dimensional conduction phase change problems. This technique is called node-jumping scheme in which the space grid keeps constant but the time step

varies. As a result, the phase change boundary maintains on a node point. The finite-difference scheme in conjunction with TDMA iterations was used to solve the enthalpy formulation of conduction phase change problem. Also, the liquid fraction is updated at nodes where the phase change is taking place.

Swaminathan and Voller [87] introduced a general enthalpy method for modeling solidification processes. A general implicit source-based enthalpy method was utilized for the analysis of solidification systems. They reported that with their proposed scheme there is no need to set under-relaxation parameter that is required to achieve a faster convergence in the enthalpy update and the enthalpy is a function of temperature. Thus, nonlinear system needs to be solved by two steps. First step is to linearize the discrete equations using the outer Newton linearization according to the current known values (T or h). Second step is to solve the inner linear equations using a direct iteration method (e.g., Gauss elimination) or a point-by-point iterative method (e.g., Gauss-Seidel) as the value of the liquid fraction is not known. For this problem, an appropriate governing equation for 2-D presented by Swaminathan and Voller [87] for the system is

$$\frac{\partial H}{\partial t} = \nabla . (k \nabla T) \tag{3.2}$$

where k is the mixture conductivity given as

$$k = (1 - g)k_s + g k_l \tag{3.3}$$

and H is a mixture enthalpy written as

$$H = (1 - g)H_s \quad + g H_l \tag{3.4}$$

and g is the volume fraction of the liquid, and the subscripts s and l represent solid and liquid phases, respectively.

The specific heat is a function of temperature alone, while the latent heat of fusion is constant. The enthalpy can thus be written as

$$H = (1-g)\int_{T_{ref}}^{T} \rho c_s dT + g\int_{T_{ref}}^{T} \rho c_l dT \; + g\rho L \qquad (3.5)$$

where c is the specific heat, ρ is the density, L is the latent heat of fusion, and T_{ref} is an arbitrary reference temperature.

3.2 Numerical methods

There are two methods to describe the thermal behavior of phase change phenomenon: the enthalpy method and the effective heat capacity method. The problem of phase change is solved by considering one governing equation for the two phases; the interface condition is automatically satisfied, creating a mushy zone between the two phases.

3.2.1 Enthalpy method

The enthalpy method assumes that the enthalpy in the energy equation is composed of sensible and latent parts, where the sensible enthalpy h_s is calculated by

$$h_s = h_{ref} + \int_{T_{ref}}^{T} c(t)d\,T \qquad (3.6)$$

In a realistic condition, the phase change usually occurs in a non-isothermal temperature range, such as in the case of paraffin. In such cases, tracking the solid−liquid interface might be difficult. To overcome this difficulty, the problem is reformulated according to the Stefan condition, which applies a new form of equations. These equations are applied over the entire fixed domain. This can be performed by calculating what is called an enthalpy function $H(T)$ of the materials. Then, instead of temperature,

the enthalpy $H = h_s + h_l$ is set for phase change. This method has been used successfully to solve a wide range of phase change problems, as reported by Agyenim et al. [8], Dutil et al. [61], Qiangbet al. [88], Tao and He [89], and Waqas and Kumar [47].

3.2.2 Effective (apparent) heat capacity method

To avoid tracking the interface, the apparent heat capacity method is used. In this method, the latent heat is calculated by integrating the heat capacity over the temperature, and the computational domain is considered as one region. Furthermore, there is a direct relation between the effective heat capacity of a material and the specific heat during phase change. However, the effective heat capacity becomes an inverse relation with the width of the melting and solidification temperature range [16]. Thus, the time steps must be small enough so that this temperature range is not overlooked in the calculation. If it is assumed that the heat of fusion is released equally throughout the entire phase change process, the effective heat capacity, or the C_{eff} term can be written as:

$$C_{eff} = \frac{L}{T_{liquid} - T_{solid}} + C \qquad if \quad T_{liquid} \leq T \leq T_{solid} \tag{3.7}$$

and

$$C_{eff} = C \quad if \quad T < T_{solid} \;\; or \;\; T > T_{liquid} \tag{3.8}$$

In addition to the assumption of evenly distributed heat of fusion, other relationships between the heat absorbed or released (the effective heat capacity) and temperature were used. Heim and Clarke [90] assumed a linear relationship for effective heat capacity, while Diaconu and Cruceru [91] expressed it in a Gauss function as shown in Figure 3.1.

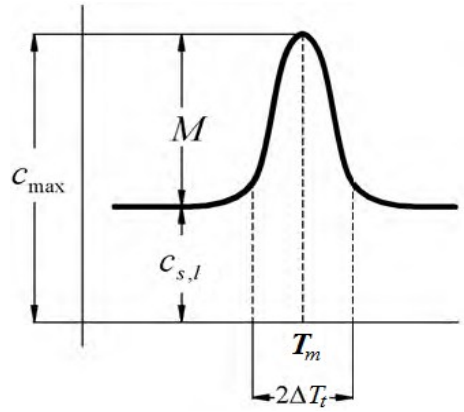

Figure 3.1 Gauss function approximation for the specific heat capacity of PCM

$$C = C_{s,l} + \frac{M}{\Delta T_t} \exp\left[-\left(\frac{T - T_m}{\Delta T_t}\right)^2\right] \qquad (3.9)$$

where ΔT_t is the temperature range of the phase transition, M is the melting peak factor, which is equal to $L/\sqrt{\pi}$, and $C_{max} = C_{s,l} + \frac{M}{\Delta T_t}$ as presented by Diaconu, B.M. and M. Cruceru [91].

Yuan and Medina [92] presented a work dealing with a problem of phase change processes that start from a partially melted state. A typical wall temperature with paraffin-based PCMs was studied experimentally. The effective heat capacity of the PCM was determined using the differential scanning calorimeter (DSC) test method over the phase change temperature range. Based on the test results, a modified model for paraffin-PCM was developed to be used in cases of complete or partial melting.

Cao and Faghri [93] formulated the enthalpy-based energy equation into a non-linear equation with a single variable for the temperature transforming model (TTM). However, with this method it is difficult to suppress the melting front velocity at zero in the solid phase. The ramped switch-off method (RSOM) was considered to be the simplest technique to set the velocity equal to zero in the solid phase by setting values for

momentum and velocity-correction equations able to inhibit any motion. In a solid−liquid interface, the RSOM undergoes a discontinuity in velocities, while the TTM manages to create a mushy zone where the temperature is continuous. Zhanhua and Yuwen [94] studied the effects of three different solid velocity correction schemes, the ramped switched-off method (RSOM), the ramped source term method (RSTM) and the variable viscosity method (VVM) on a temperature transforming model (TTM). They reported that the discretized TTM can be used efficiently to obtain convergence if a grid size was selected with a not-too-small time step. Additionally, applications of RSOM and RSTM-TTM lead to the same results, which are more precise than with the VVM.

3.3 A numerical study of centralized latent heat thermal energy storage

The design and characterization of a large-scale LHTES system has not yet been investigated numerically. A full description of the LHTES unit is presented, following by a discussion of numerical modelling of the system. Additionally, the thermo-physical properties of the PCM are modeled. The second part of my research focuses on investigating the best performance of a PCM unit through which parametric study of all thermal factors will be carried out. The third part will be devoted to determining the optimal size of such a unit based on varying the ventilation air flow rate.

3.3.1 Physical model

The schematic diagram of the three-dimensional physical model for a centralized storage unit filled with phase change materials is shown in Figure 3.2. The hybrid PCM closed system is designed to be placed into ceiling or basement boards. The justification for using a LHTES system rather than integrating PCMs into walls, floors and/or ceilings

is to avoid the question of a weakness in the mechanical strength of a building structure itself. Two different industrial fins, made of aluminum, are used to increase the thermal power of the storage unit and are connected to the metal box from the internal and external sides of the lower and upper faces. All dimensions of the computational domain are referenced to the experimental study conducted by Stritih and Butala [74], as shown in Table 3.1. The fins are placed on the external side of the box to increase the area exposed into convection heat flux; meanwhile, those fixed inside the box are aimed at boosting the thermal conduction heat flux. The box is filled with paraffin, which has a melting point of 22℃ and heat storage capacity of 172 kJ kg^{-1} within an operating temperature range of 11-26℃ and a specific heat of 1.8/2.4 (solid/liquid) kJ kg^{-1} K^{-1}.

Table 3.1 Storage unit properties

Storage unit properties	
Dimensions	500×220×90 (mm)
Total mass	16.2 kg
Mass of the shell	12.6 kg
Mass of PCM	3.6 kg
Phase change temperature	20-22^{o}C
Operation temperature	15-30^{o}C
Cold storage capacity (11-26^{o}C)	172 kJ kg^{-1}
Cold stored in PCM	732.6 kJ
Cold stored in shell	11.3 kJ

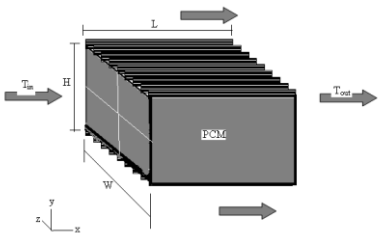

Figure 3.2 Physical model

Fin	Height (mm)	Thickness (mm)	Distance (mm)
External	11	2	6
Internal	21	2	7

3.3.2 Numerical model description

The schematic diagram of the three-dimensional computational domain storage unit filled with PCM is shown in Figure 3.3. The aluminum fins are arranged orthogonal to the axis of the unit. The heat transfer fluid flows in the vicinity of such a unit. In other word, the model has three zones; fluid or solid zones as described herewith:

1- An Air box, a flow channel through which the air flow passes through the fins and around the whole system;

2- The PCM box, which is defined as a fluid/solid; and

3- The Fin box, which is defined as a solid.

All the boxes are coupled to each other as one geometrical body. The Air and PCM boxes are coupled so that thermal energy goes through and from the air to a fin and then from a fin to the PCM.

Due to the symmetrical structure of the unit considered, the computational domain has been simplified to deal with only one symmetry unit cell in which the planes of symmetry are in the middle of the fin and are mid-way between the two subsequent fins, as illustrated in Figure 3.3.

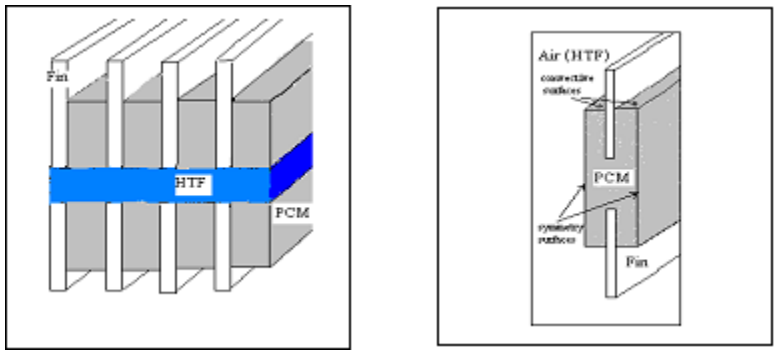

Figure 3.3 Computational domain of the developed model

The detailed properties of the fins are listed in Table 3.1. The governing equations of phase change phenomenon are applied to describe the heat flow through the developed model at different inlet conditions (i.e., inlet air-temperature and air flow rate). The developed model is designed to overcome the limitations that may be encountered due to the complexity of the involved physical phenomena, e.g., the convection effect in the liquid phase, moving of the solid in melted mixture, and volumetric expansion due to changes in the phase. Previous studies, however, have ignored one or more of the influential parameters of the phase change process.

3.3.3 Modeling the physical properties of PCMs

The developed model is verified by using experimental data as reported by Stritih and Butala [74]. The developed model is also compared to a numerical model performed by Stritih and Butala [75]. Through a parametric study, the most influential parameters are investigated to characterize the performance of the developed model system. The density and dynamic viscosity of the liquid PCM depend on its temperature. The density is introduced as

$$\rho_{(PCM)} = \frac{\rho_l}{\phi(T - T_l) + 1} \qquad (3.10)$$

where $\rho_{(PCM)}$ is the density of a PCM; ρ_l is the reference density of the PCM at its melting temperature; T_l , and ϕ is the expansion factor. The value of $\phi = 0.001\mathrm{K}^{-1}$ is selected based on the analysis of the detailed data presented by Humphries and Griggs [95].

The dynamic viscosity of the liquid PCM was introduced as Reid et al. [96]:

$$\mu = \exp\left(A + \frac{B}{T}\right) \ (\mathrm{kg/m.s}) \qquad (3.11)$$

where $A = -4.25$ and $B = 1790$ are coefficients.

Since the phase transition from solid to liquid usually occurs at a certain temperature range, the latent heat is a function of temperature. In most cases, the latent heat should be used in the form of an effective heat capacity or a as a specific enthalpy based on experimental results. The effective heat capacity is measured using the differential scanning calorimeter (DSC) method with a heating rate of 0.1K/min, as reported by Arkar et al. [80] in Figure 3.4. As given in both Eqs. (3.10), and (3.11), the density and viscosity of a PCM are dependent on the temperature. The correlations for the density and viscosity of a PCM are generated as illustrated in Figures 3.5 and 3.6.

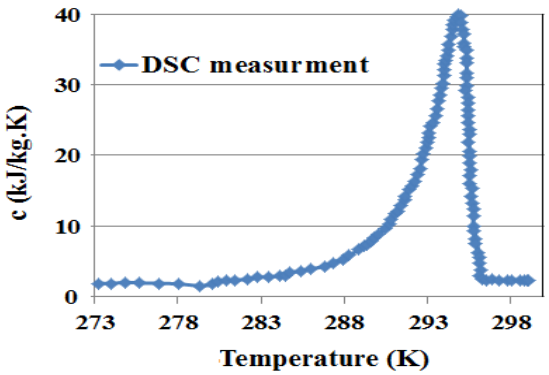

Figure 3.4 DSC measurements for the effective heat temperature capacity of RT20

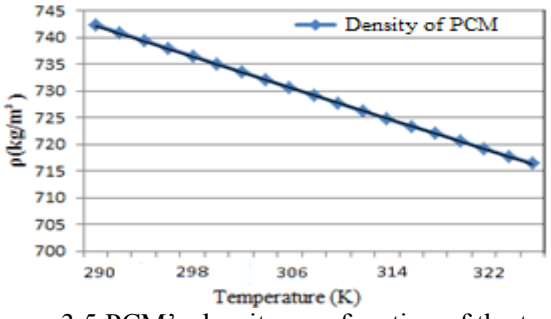

Figure 3.5 PCM's density as a function of the temperature

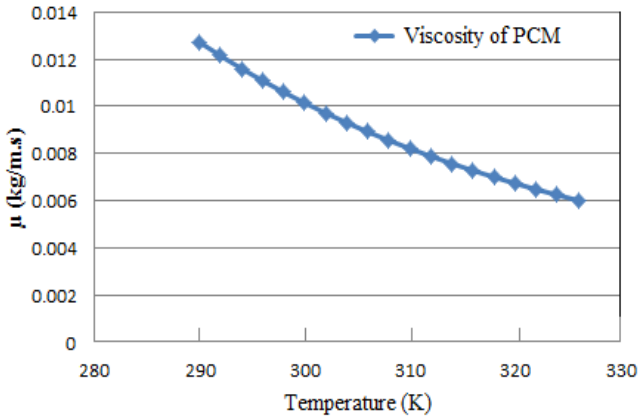

Figure 3.6 PCM's viscosity as a function of the temperature

3.3.4 Heat and mass transfer formulation for LHTES system

The enthalpy porosity method is employed to solve a multi-dimensional phase change heat transfer model where both enthalpy and temperature are unknown parameters and a unified energy equation is built. The enthalpy-porosity technique for modeling convection-diffusion phase change has the advantage of coupling the momentum and energy equations belonging to a fixed-grid solution and avoiding having to consider variable transformations. Furthermore, the main advantage of this approach is that it converges quickly and produces an accurate result with modest computational requirements. In fact, a numerical solver algorithm is employed for solving the momentum and continuity equations [97], resulting in determining the velocity field. The liquid fraction and temperature changes are assumed to have a linear relationship in the mushy regions. In order to track the solid−liquid interface positions, the method updates the liquid fraction at each unit cell at each time step in the entire computational domain [83].

A numerical technique is employed to simulate PCM heat transfer within a range of a certain temperature, which typically had been done by using the enthalpy porosity theory to deal with the solid−liquid interface. The porosity effect was found to be similar to the liquid volume fraction of the porous media at the mushy regions (Brent et al. [53]). From the viewpoint of a multiphase flow model such as the volume of fluid method (VOF) or the mixture and Euler model, only the VOF and a solidification/melting model can be applied simultaneously. A VOF algorithm to solve the problem of updating the volume fraction is discussed in general terms by Hirt and Nichols [98], and remains one of the most widely used interface tracking methods.

In the interest of simplicity, the following assumptions are considered:

- The axial conduction and viscous dissipation in the fluid are considered to be negligible;
- The PCM is considered to be homogenous and isotropic;
- The thermo-physical properties of the PCM such as the density, the viscosity, and the specific heat vary with temperature but the thermal conductivity is assumed constant. The density of the heat transfer fluid (air) varies with temperature and the other thermo-physical properties of the air are considered constant; and;
- The occurrence of PCM melting is considered at a single mean melting temperature T_m.

A model of a centralized finned thermal energy storage system to investigate heat flow behavior is carried out. The simulation can be carried out under all operating conditions of pressure and temperature and with various ventilation air flow rates over a wide range of time. Furthermore, the model will be evaluated against experimental data

available in the literature. Thus, a detailed parametric investigation will be carried out in this work. A large amount of data could be generated using the proposed model, and then the results obtained could be analyzed and discussed. In order to interpret the outcomes of the transient simulations, flow visualization will be presented based on the parameters of interest.

The energy equation could be written in terms of the sensible enthalpy, as follows:

$$h = \int_{T_{ref}}^{T} c\, dT \tag{3.12}$$

$$\frac{\partial \rho h}{\partial t} + div\left(\rho \underline{u} h\right) = div((k/c) grad h) + S_h \tag{3.13}$$

where k is the thermal conductivity, c is the specific heat capacity, and S_h is the latent heat source term. In order to describe the fluid flow of full liquid and mushy regions, the conservation equations of momentum and mass are required. By assuming a Newtonian laminar flow, such equations can be presented in the following forms:

$$\frac{\partial (\rho u)}{\partial t} + div\left(\rho \underline{u}\, u\right) = div(\mu\, grad\, u) - \frac{\partial P}{\partial x} + Au \tag{3.14}$$

$$\frac{\partial (\rho v)}{\partial t} + div\left(\rho \underline{u}\, v\right) = div(\mu\, grad\, v) - \frac{\partial P}{\partial y} + Av + S_b \tag{3.15}$$

$$\frac{\partial (\rho)}{\partial t} + div\left(\rho \underline{u}\right) = 0 \tag{3.16}$$

where $\underline{u} = (u, v)$ is the velocity, P is the effective pressure, S_b is the buoyancy source term, and μ is the viscosity. The buoyancy source term can further be expressed as

$$S_b = \rho_{ref} g \beta (h - h_{ref})/c \tag{3.17}$$

where β is the thermal expansion coefficient and h_{ref} and ρ_{ref} are the reference values of enthalpy and density, respectively [53].

The Boussinesq approximation is assumed, in which the density is constant in all terms excluding a gravity source term, and the buoyancy source term can account for the effects of natural convection, as follows:

$$Ra = \frac{g\gamma\Delta T l^3 \rho}{\mu\alpha} \tag{3.18}$$

$$\gamma = -\frac{1}{\rho}\frac{\partial \rho}{\partial T} \tag{3.19}$$

$$\alpha = \frac{k}{\rho c}$$

$$C_{eff} = \begin{cases} C_{s;} & T < T_l \\ \dfrac{L}{(T_s - T_l)} + C, & T_l \leq T \leq T_s \\ C_l & T > T_s \end{cases}$$

$$k = \begin{cases} k_{s;} & T < T_l - \Delta T \\ k_s \dfrac{k_l - k_s}{2(T_s - T_l)} + [T - (T_l - \Delta T)] & T_l - \Delta T \leq T_l + \Delta T \\ k_l & T > T_l + \Delta T \end{cases}$$

If the value of the Rayleigh number is below 10^8, the flow is laminar; meanwhile, turbulent flow is reached when the Rayleigh number lies between 10^8 and 10^{10}. The fluid density changes satisfy the Boussinesq approximation, but only in regard to the volume-related items in the momentum equations.

One of difficulties encountered using a fixed grid approach during the analysis of solidification and melting processes is how to account for mass and heat transfer conditions in the vicinity of the phase change. Indeed, the basic approach to resolve such problem is to assign appropriate volume source terms combined with the governing equations (momentum and energy). In the enthalpy-porosity approach, the energy

equation source term (S_h) which accounts for the latent heat evolution could be written in the following form:

$$S_h = \frac{\partial(\rho \Delta H)}{\partial t} + div\left(\rho \underline{u} \Delta H\right) \tag{3.20}$$

where $\Delta H = F(T)$, the latent heat content, is recognized as a function of temperature. Indeed, the convective term $div\ (\rho \underline{u} \Delta H)$ would disappear when the isothermal case is satisfied. In fact, the value of $F(T)$ can be generalized as follows;

$$F(T) = \begin{cases} L, & T \geq T_{liquid} \\ L(1 - f_s), & T_{liquidus} \geq T \geq T_{solid} \\ 0, & T < T_{solid} \end{cases} \tag{3.21}$$

where f_s is the local solid fraction.

The total enthalpy of the material can be introduced as

$$H = h + \Delta H \tag{3.22}$$

where

$$h = h_{ref} + \int_{T_{ref}}^{T} c\, dT \tag{3.23}$$

and h_{ref} is the reference enthalpy, T_{ref} is the reference temperature; and c is the specific heat. The total enthalpy, H, is the sum of the sensible heat, $h = c\,T$, and the latent heat ΔH. The liquid friction, f, can be expressed as

$$f = 0 \quad if \quad T < T_{solid}$$

$$f = 1 \quad if \quad T > T_{liquid}$$

$$f = \frac{T - T_{solid}}{T_{liquid} - T_{solid}} \qquad if \qquad T_{solid} < T < T_{liquid}$$

In terms of the latent heat of the material, the latent heat content can be written in the following form:

$$\Delta H = fL \tag{3.24}$$

In the enthalpy-porosity technique, the mushy region (the partially solidified region) is treated as a porous medium. For the purpose of the methodology, it is worthwhile to consider the whole cavity as a porous medium. In fully solidified regions, the porosity λ is set to be equal to zero and takes the values $\lambda = 1$ in fully liquid regions, and lies between 0 and 1 in mushy regions. Accordingly, the flow velocity is linked to the porosity state and is defined as:

$$\underline{u} = \lambda \underline{u}_i \tag{3.25}$$

where u_i is the real flow velocity. Equation (3.24) can be extended to yield

$$\underline{u} = \begin{cases} \underline{u}_i, & for\ liquid\ region \\ (1 - f_s)\underline{u}_i, & for\ mushy\ region \\ 0, & for\ soild\ region \end{cases} \tag{3.26}$$

To describe the flow of a fluid through a porous medium, it is necessary to introduce Darcy's law as:

$$\underline{u} = -\left(\frac{\kappa}{\mu}\right) gradP \tag{3.27}$$

where κ is the permeability, which is considered as a function of the porosity. Based on Darcy's law, the Carman-Koseny equation can be derived as;

$$gradP = -\frac{C(1-\lambda)^2}{\lambda^3}\,\underline{u} \tag{3.28}$$

A (in Eqs. 2.13, and 2.14) can be presented as

$$A = -\frac{C(1-\lambda)^2}{\lambda^3+\omega} \tag{3.29}$$

The value of C is related to the morphological properties of the porous medium, and it is assumed constant at 1.6×10^5. The constant ω is used to avoid dividing over zero and is set to be 10^{-3} [82].

3.3.5 Boundary and initial conditions

The initial and boundary conditions are referenced to those of Stritih and Butala experiment [74]. The whole initial computational domain is set to be at the ambient temperature. In addition, the boundary condition on each side of the wall is adiabatic. The symmetry boundary conditions can be applied in half of a computational domain to reduce the calculation time, as shown in Figure 3.3. The following initial and boundary conditions are applied to solve the governing equations:

1. Initial conditions

$$t = 0, \qquad T = T_i = 288.15\text{K}$$

$$u = 1.5\text{m/s}$$

2. Symmetry boundary conditions at a side:

$$\left.\frac{dT}{dx}\right|_{x=0} = \left.\frac{dT}{dx}\right|_{x=L} = 0, \qquad \left.\frac{dT}{dy}\right|_{y=-H/2} = \left.\frac{dT}{dy}\right|_{y=H/2} = a\left(T_{out,i} - T_{in,i}\right)$$

3.4 Single-zone building integrated into a LHTES system

3.4.1 The test room description

The thermal building simulation model is for a single-zone model. This model is a prototype of a test room with dimensions of 11.44m (length) ×5.69m (width) ×2.76m (height). Each room wall is divided into several layers, which allows the modeling of

multi-layer walls, as shown in the Appendix (A). The zone under study is a living room with 11.44m×5.69m of floor area and one exterior wall. The exterior wall, a façade (5.69m×2.76m), faces south-north. The window area is 2.08m^2 in south wall, double pane. The opaque part of the façade has a U-value of 0.34W/m^2 K, while the double-pane window has a U-value of 2.95W/m^2K. The ceiling insulation level amounts to a U-value of 0.93W/m^2K. The floor has a U-value of 1.31W/m^2K. Two adjacent rooms in the vicinity of the considered model are assumed to be adiabatic. The test room is occupied by two people generating about 120W. During the occupancy time there is a scheduled additional load of 230W (appliances). For more details on the simulation boundary conditions, please refer to Appendix (B). Typical Meteorological Year (TMY) weather file data is used. The weather data (ambient temperature and solar radiation intensity) are generated using TRNSYS Type TMY2 software.

3.4.2 Thermal storage unite integrated into a single building zone ceiling space

A schematic diagram of a direct-gain solar room and a general sketch of the installation are depicted in Figure 3.7. The thermal storage unit was modeled on a portion of the ceiling. The unit was used to absorb the daytime energy while the PCM changes from solid to liquid, and later in the evening when the room temperature falls, the stored energy is retrieved, resulting in solidified PCM again.

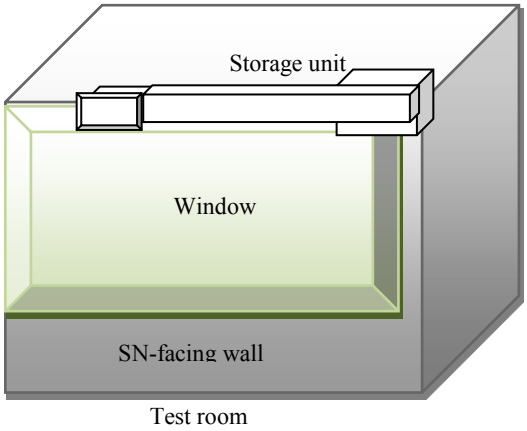

Figure 3.7 Thermal storage model of a free cooling concept for a single-size building

Indoor environment:

$$\rho_a V_r c_a \frac{dT_a}{dt} = a_{in}(T_s - T_a)A_{wa} + q_{rad,in}A_{wa} + Q_{I/V} - Q_{HVAC} + Q_W \qquad (3.30)$$

where

$$Q_{I/V} = \rho_a V_r c_a \times ACH \times \frac{(T_{amb} - T_a)}{3600} \qquad (3.31)$$

$$Q_W \quad = U_W A_W (T_{amb} - T_a) \qquad (3.32)$$

where V_r is the room volume, $Q_{I/V}$ is the infiltration heat flow and ventilation, T_{amb} is the ambient temperature, T_a is the indoor temperature, ACH is the air change per hour, Q_{HVAC} is the heat supplied by the air heating and conditioning equipment , Q_W is the heat flow through the window, and U_W is the total overall heat transfer coefficient.

The heating/cooling load can be calculated from the energy balance equation as:

$$Q_{C/H} = a_{in}(T_s - T_{set})A_{wa} + q_{rad,in}A_{wa} + \rho_a V_r c_a \times ACH \times \frac{(T_{amb} - T_{set})}{3600} + U_W A_W (T_{amb} - T_{set}) \quad (3.33)$$

where T_{set} is the set point temperature, selected as 20℃ for heating and 25℃ for cooling. According to the ASHRAE recommendations provided by Jegadheeswaran and Pohekar [25], the convective heat transfer coefficients are assumed to be a_{in} =8.3 W/m^2 K and a_{out} =17 W/m^2 K.

The following initial and boundary conditions are applied to solve the governing equations:

1. Initial conditions

$$t = 0, \qquad T = T_i = 288.15\text{K}$$

$$u = v = 0$$

2. Boundary condition

$$\rho_a V_r c_a \frac{{T_a}^i - {T_a}^{i-1}}{\Delta t} = a_{in}\left({T_s}^i - {T_a}^i\right)A_{wa} + q_{rad,in}^{i-1}A_{wa} + Q_{I/V}^{i-1} - Q_{HVAC}^{i-1} + Q_W^{i-1} \quad (3.34)$$

The cooling/heating load is calculated at each time step based on the wall temperature; where ambient corresponds to the previous time step.

$$Q_{C/H}^i = a_{in}\left(T_s^{i-1} - T_{set}\right)A_{wa} + q_{rad,in}^{i-1}A_{wa} + \rho_a V_r c_a \times ACH \times \frac{\left(T_{amb}^{i-1} - T_{set}\right)}{3600} + U_W A_W\left(T_{amb}^{i-1} - T_{set}\right) \quad (3.35)$$

3.4.3 Integrated thermal storage unit into single-zone building at floor space

Figure 3.8 demonstrates the integration of a centralized LHTES within the basement of a building. The strategy allows fresh air to be supplied into the storage system.

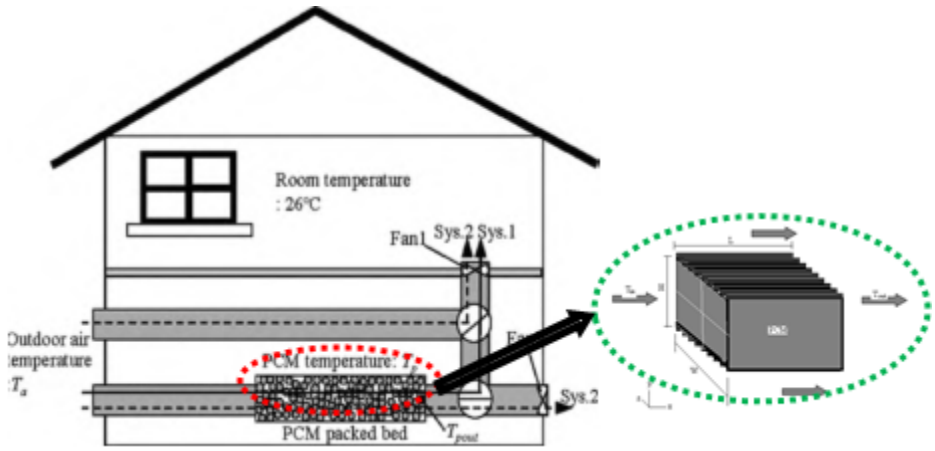

Figure 3.8 Conceptual centralized latent heat thermal energy storage system [99]

3.5 Summary

In the first part of this dissertation, a mathematical model of LHTES system is conducted to investigate its heat flow characteristics. Two models are presented. First, a two-dimensional model of a LHTES rectangular cavity is studied. The rectangular cavity was filled with gallium as the PCM. Second, a three-dimensional mathematical model of the centralized LHTES system is carried out to analyze the thermal performance of the melting process for both the quasi-steady state and the transient conjugate heat transfer problems. Paraffin RT20 was selected as the PCM medium in the hybrid PCM closed system multi-fin heat sink for cooling and heating applications in a building.

Chapter 4

Two-Dimensional LHTES Model Development and Validation

A numerical simulation method has been conducted to analyse the 2-D phase change material (PCM) melting process problem in a rectangular cavity filled with Gallium. The numerical prediction is verified by comparing with experimental data. Solid−liquid interface positions and the temperature distributions at different rates of melting are computed for three cases with different boundary conditions. The first case has a constant wall temperature on the left and right sides while the top and bottom surfaces remain insulated. In the second case, the top and bottom surfaces are subjected to a constant convective heat transfer while the side surfaces are kept insulated. To examine the increasing melting rate, a third case is established where two fins are set on the top and bottom of a rectangular cavity. To verify the methodology, a comparison between the experimental work conducted by Gau and Viskanta [100] and a numerical simulation of the evolution of a melted phase's fraction was performed.

4.1 Case I: 2-D LHTES model for constant wall temperature

A proposed physical model of interest has a length of 88.9mm and height of 63.5mm in a rectangular cavity filled with solid metal gallium, as illustrated in Figure 4.1. The temperature of gallium is assumed to be 28.3℃. At time zero, the left wall temperature suddenly rises to 38℃ and then remains constant, while the temperature of the right wall is constant at 28.3℃. The model employs a single precision (which requires conversion of about 7 decimal digits), unsteady solver to solve the implicit second-order

scheme, and the time step is set to 0.2s. The pressure implicit with splitting operator (PISO) algorithm is used for pressure-velocity coupling.

The computational domain of the physical model is meshed at a 44×32 size using GAMBIT software. The methodology used in this proposal is verified using the data from work conducted by Qiang et al. [88], as shown in Figure 4.2. The melted fraction for different melting times is shown in Figure 4.3. The results show a good agreement with the available reference data.

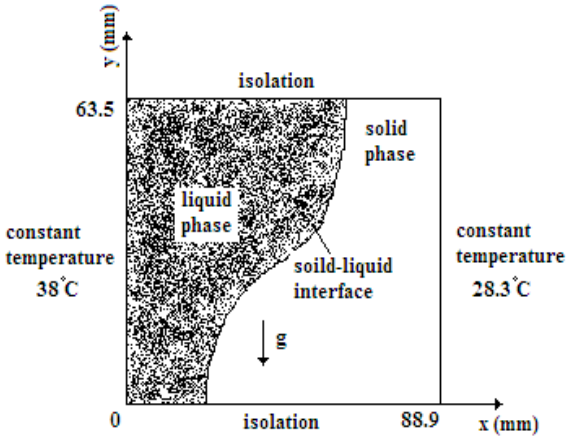

Figure 4.1 Physical model [88]

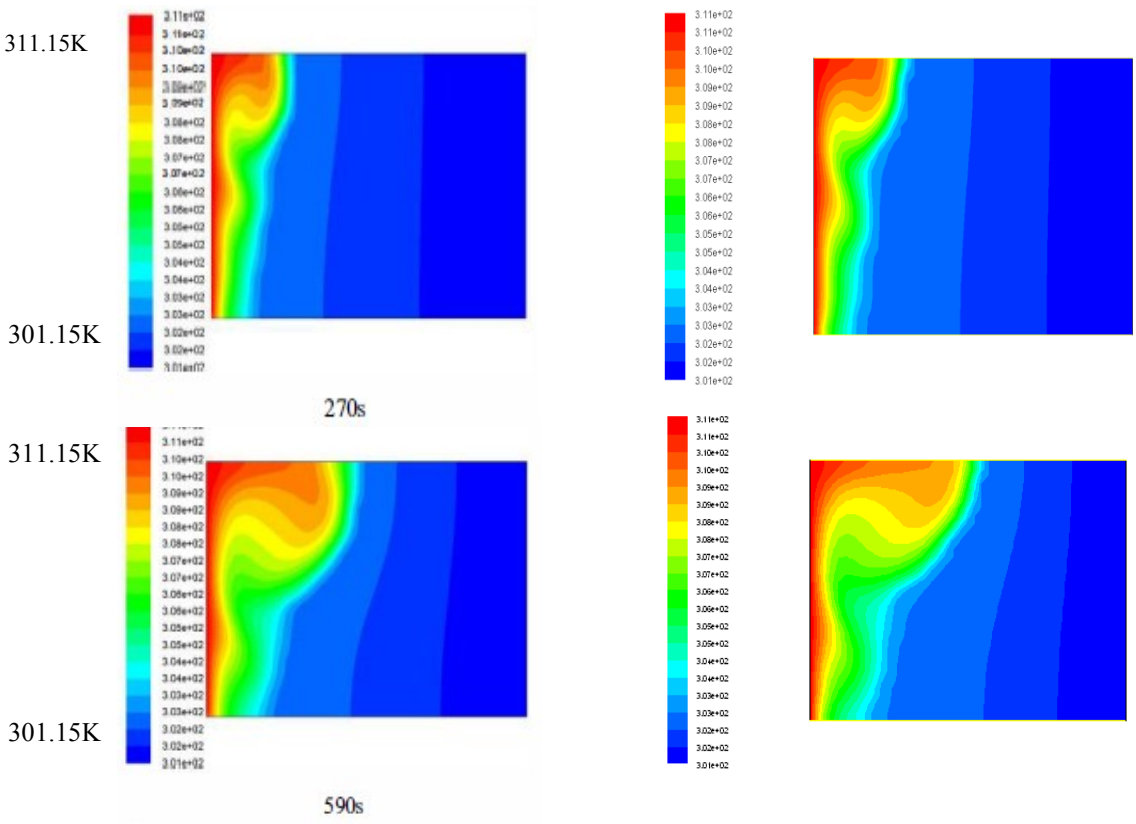

Figure 4.2 Temperature fields of two different melting time processes, for comparing the methodology used (on the left side) and the reference data (on the right side)

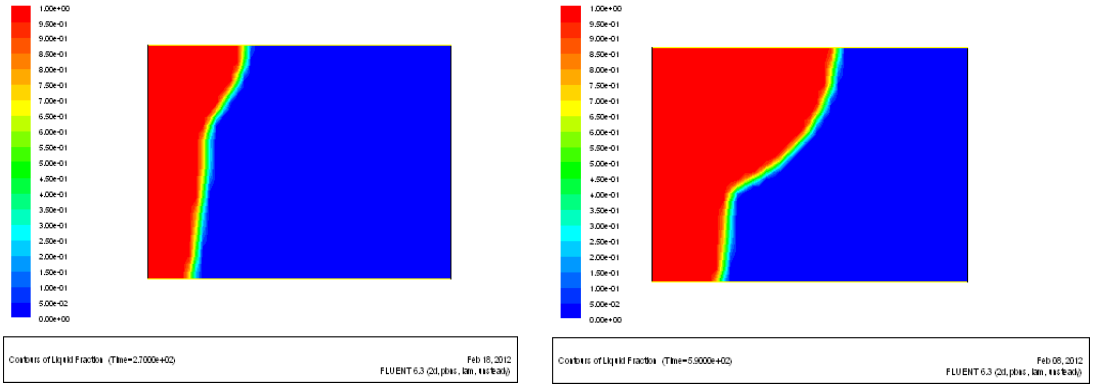

Figure 4.3 Melted fractions for different melting times

4.2 Case II: 2-D LHTES model validation with experimental work

To verify the model, the numerical simulation of the evolution of fraction of the melted phase was compared with experimental data reported by Gau and Viskanta [98]. They measured the performance of a physical model in a rectangular cavity with a length of 88.9mm and height of 63.5mm filled with gallium PCM. The melting temperature of gallium is assumed to be 29.8℃. At time zero, the left wall temperature suddenly rises to 38℃ and remains constant, while the temperature at the right wall was maintained constant at 28.3℃. Table 4.1 gives the relevant properties of gallium, air, and aluminum. The numerical solution was performed using Fluent-12 [101]. Figure 4.4 shows the solid−liquid interface positions for 2min, 6min, 10min, and 17min of melting processes. The numerical simulation results are in good agreement with the experimental results, as indicated in Figure 4.4.

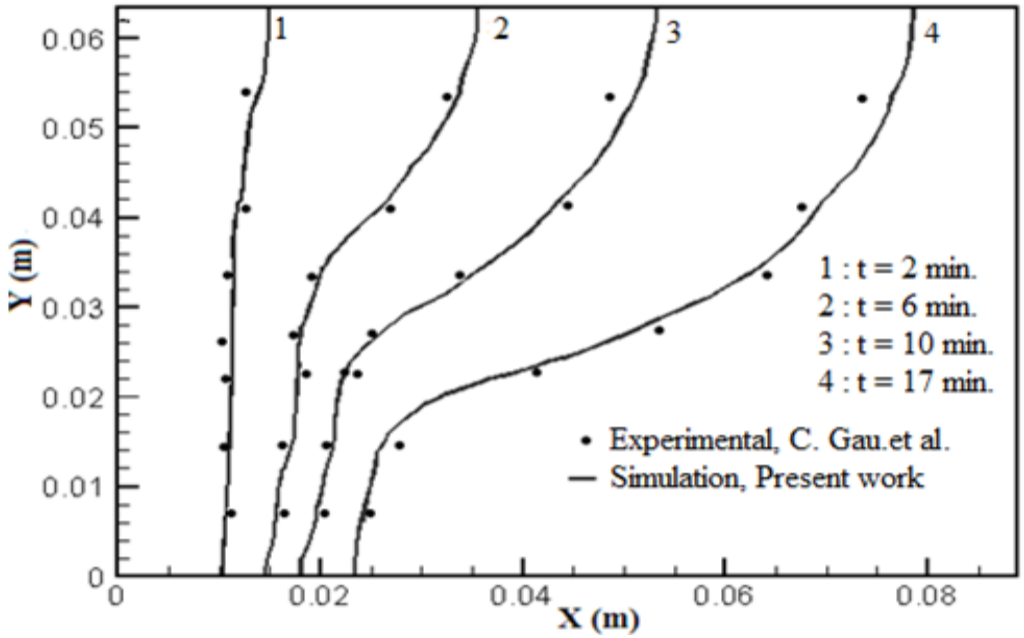

Figure 4.4 Comparison between experimental and numerical results in the evolution of the fractions of melted phase

Table 4.1 Properties of gallium, air, and aluminum used for the calculations

Materials	$\rho(\mathrm{kg/m^3})$	k(W/mK)	c(J/kgK)	T_{PCM}(℃)	L(J/kg)	$\mu(\mathrm{kg/ms})$
Gallium	6093	32	381.5	29.78	80160	1.81×10^{-3}
Air	$1.2\times10^{-5}T^2 - 0.01134T + 3.498$	0.0242	1006.43	-	-	1.7894×10^{-5}
Aluminum	2719	202.4	871	-	-	-

4.3 Case III: 2-D LHTES model for constant convective boundary conditions

The same domain used in Case I is studied by imposing a constant convective heat transfer on the top and bottom surfaces while the side surfaces remain insulated, as shown in Figure 4.5. Air passes in a free stream aligned at the top and bottom surfaces at certain thermal properties of heat transfer coefficient, h =20 W/m^2 K, and ambient temperature of T_∞ =311.15K. Two contours of the melted fraction and temperature distribution are illustrated in Figures 4.6 and 4.7, respectively.

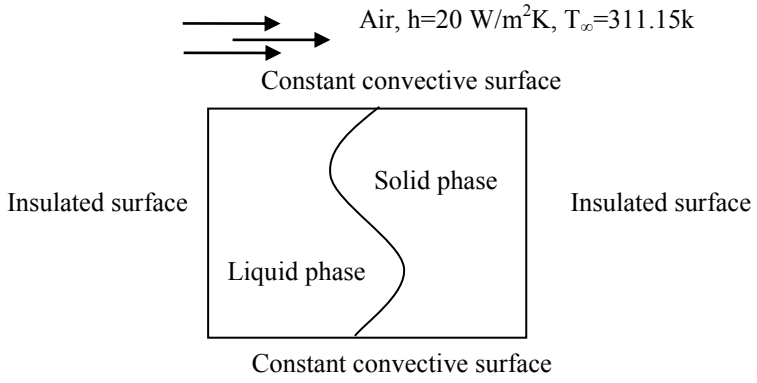

Figure 4.5 Physical model

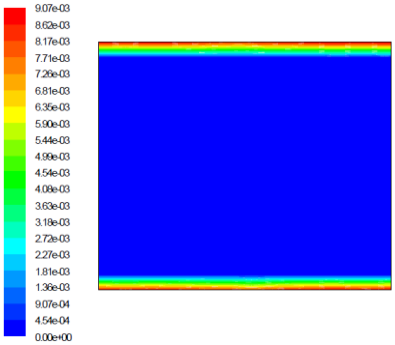

Figure 4.6 Melted fraction at 677s

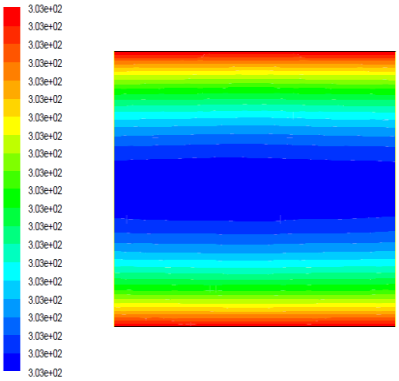

Figure 4.7 Temperature field at 677s

4.4 Case IV: 2-D LHTES model for constant convective boundary conditions with fins

The geometry for this case is the same as in the previous case study, except for two fins that are added on the top and the bottom, as shown in Figure 4.8. They are added in order to study the effect of fins on the thermal performance of a unit. Two contours of the melted fraction and temperature distribution is illustrated in Figure 4.9. After approximately 3hr, the melting rate appears to be slow and there is no a significant effect of the extended surfaces on the top and the bottom on enhancing the heat exchange between PCM and HTF.

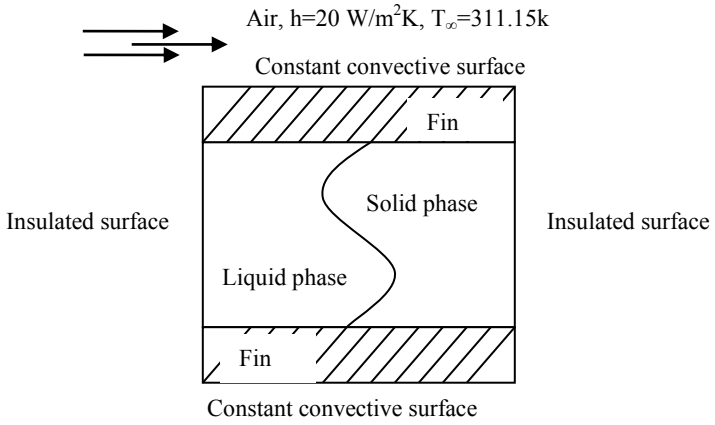

Figure 4.8 Physical model

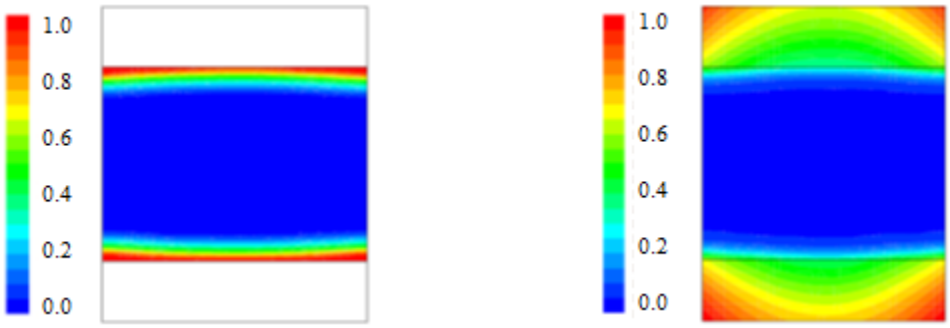

Figure 4.9 Melted fraction and temperature field at 3hr

The compassion between the finned unit and the unit without fins indicates that the melted fraction is speeded up by % 48 at 4000s of simulation time for a finned unit compared to a unit without fins, as illustrated in Table 4.2.

Table 4.2 Comparison between a finned unit and a unit without fins

Time (s)	Melted fraction for a unit without fin	Melted fraction for a unit with fin	Enhanced melting rate %
1000	0.0418	0.0772	46
2000	0.117	0.222	47
3000	0.192	0.367	48
4000	0.267	0.513	48
5000	0.342	0.658	48
6000	0.417	0.804	48

4.5 Summary and conclusion

A numerical simulation method has been carried out to solve the 2-D phase change material (PCM) melting process problem in the condition of a side-heated wall enclosure and natural convection. The developed model solves phase change problem using the enthalpy-porosity method adopted by computational fluid dynamic (CFD), Fluent 12. The melting evolution process is characterized at several time intervals to provide the positions of the solid-liquid interface and temperature distributions. The numerical results are compared with the available experimental and numerical data. The

comparisons show that the developed model is able to predict the thermal behavior of PCMs. However, a LHTES 2-D PCM model applied to a convective boundary condition has indicated that further investigations is required to provide more details about the heat exchange between the PCM and the air as a fluid heat transfer (FHT) process.

Chapter 5

Three-Dimensional Model Development of a Centralized LHTES System

5.1 Introduction

Different techniques have been evaluated to enhance the performance of PCM systems using fins which are being the most common method to boost the thermal conduction heat flux within the PCM [25-27]. A simplified numerical model was developed for a thin fin system assuming quasi-linear and transient. Physical properties of PCM were assumed to be constant for liquid and solid phases. Natural convection heat transfer occurs from the fins to the PCM caused by instabilities created above fins and the solid−liquid interface. Numerical results were in a good agreement with experimental data and showed that the rate of heat transfer could be enhanced if the space between the fins is reduced.

The centralized LHTES system is integrated into a mechanical ventilation system through suitable air supply ducts inside a room of the building to store/retrieve the thermal energy, which leads to justify the indoor air temperature variation during the day-time, as shown in Figure 5.1. To regulate the function of a mechanical ventilation system, a control unit is required to balance the temperature difference between the inlet ambient air, T_a and outlet air from LHTES system, T_{out}. Thus, the ventilation system has two modes of operation. First mode is to restrict the air flow to just pass through the LHTES system as the ambient air temperature is higher than the set point temperature. Second

mode is to allow ambient air directly be supplied to the room and also to pass through the LHTES system thereby storing cold energy when the ambient air temperature is lower than the set point temperature as shown in Figure 5.1 (b). However, the ventilation control strategy is beyond the scope of the current study.

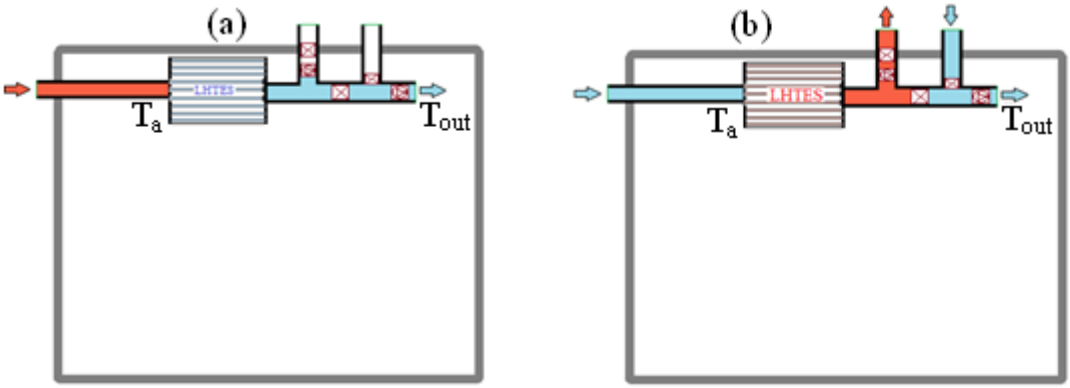

Figure 5.1 Installation of the centralized latent heat thermal energy storage system (LHTES) in two ventilation control modes; (a) discharging mode, (b) charging mode

To the knowledge of the author, the investigation of transient conjugate heat transfer for the three-dimensional mathematical model for the centralized LHTES system integrated into the building has not been addressed. The developed model solves simultaneously complete conservation equations for solid fins and solid−liquid phase change. The nonlinear variation of PCM's thermo-physical properties with temperature is considered. Here, the development of a mathematical model of a centralized finned LHTES for analyzing the thermal performance of melting process for both quasi-steady state and transient conjugate heat transfer problems is reported. The developed model utilizes PCM technology that stores and retrieves energy at almost a constant temperature and is subjected to constant convective boundary conditions of free air stream based on a specific ventilation airflow rate. The numerical simulation results using paraffin RT20 are

compared with available experimental data for cooling and heating of buildings. The effect of temperature difference between the melting point of PCM and the temperature of the heat transfer fluid (HTF) on the effectiveness of the hybrid PCM thermal performance through the discharging period is assessed. In addition, the effects of the HTF inlet temperature, HTF mass flow rate, and discharging time on the thermal performance of the hybrid PCM system are numerically investigated. A detailed transient analysis of charging/discharging process for practical application was provided. For long-time simulation, the behavior of the system shows a similar trend for various inlet air temperatures. Therefore, correlations are obtained for the distribution of melting front and solid fraction as a function of time that provide useful information for the design of hybrid finned PCM closed system. Thus, the air cooling time can be predicted for the centralized LHTES system with paraffin RT20.

5.2 Computation for LHTES model

Numerical technique is employed to simulate PCM heat transfer within a certain range of phase change temperature, which typically uses the enthalpy porosity theory to deal with solid−liquid interface. The porosity effect found to be similar to the liquid volume fraction of the porous media at mushy region [53]. Based on multiphase flow model such as volume of fluid method (VOF), mixture and Euler model, only VOF and solidification/melting model can be applied simultaneously.

For simplicity, the following assumptions are considered:

- The axial conduction and viscous dissipation in the fluid are negligible;
- PCM and porous matrix material are considered homogenous and isotropic;

- The thermo-physical properties of the PCM and transfer fluid are independent of temperature; however, the properties of the PCM could be different in the solid and liquid phases;
- The PCM is considered at a single mean melting temperature, T_m;
- The effect of radiation heat transfer is negligible.

5.2.1 Modelling

The density and the viscosity of PCM are simulated as they depend on their temperature. Assuming a Newtonian laminar flow, the continuity and momentum equations in 3-D are:

$$\frac{\partial(\rho)}{\partial t} + div(\rho \underline{u}) = 0 \quad (5.1)$$

$$\frac{\partial(\rho u)}{\partial t} + div(\rho \underline{u}\, u) = div(\mu\, grad\, u) - \frac{\partial P}{\partial x} + Au \quad (5.2)$$

$$\frac{\partial(\rho v)}{\partial t} + div(\rho \underline{u}\, v) = div(\mu\, grad\, v) - \frac{\partial P}{\partial y} + Av + S_b \quad (5.3)$$

$$\frac{\partial(\rho w)}{\partial t} + div(\rho \underline{u}\, w) = div(\mu\, grad\, w) - \frac{\partial P}{\partial z} + Aw \quad (5.4)$$

where $\underline{u} = (u, v, w)$ is the velocity, P is the effective pressure, and μ is the viscosity. The parameter A in Eqs (5.2-5.4) represents the source term for PCM.

5.2.2 LHTES unit description

The schematic diagram of the three-dimensional physical model of the centralized storage unit filled with phase change materials is shown in Figure 5.2. Two different fins, made of aluminum, are used to increase the thermal performance of the storage unit and

are connected to the metal box from both the lower and upper faces. The fins on the external side of the box are to increase the exposed area for convective heat flux whilst fins inside the box are aimed at boosting the thermal conduction heat flux. The box is filled with paraffin RT20 with a melting point of 22℃, heat storage capacity of 172 kJ kg^{-1} within an operating temperature range of 11-26℃, and specific heat capacity of 1.8 and 2.4 kJ kg^{-1} K^{-1} for solid and liquid, respectively as the experiment conducted by Stritih and Butala [74]. Paraffin RT20 is chemically stable and commercially available compared with the other materials. In addition, the phase change temperature range of paraffin RT20 is suitable to regulate the indoor air temperature within the range of the comfort condition inside the building as reported by Tatsidjodoung et al. [102]. The centralized LHTES system is integrated into a mechanical ventilation system with an advanced control unit through suitable air supply ducts for free cooling of a low-energy building. Thus, the fluctuation in indoor air temperature is stabilized during the day-time.

The three-dimensional computational domain storage unit filled with PCMs where the aluminum fins are arranged orthogonal to the axis of the unit. The heat transfer fluid flows in the vicinity of such unit. The model has three zones: 1) Air box with airflow around the fins and system, 2) PCM box (fluid/solid), and 3) Fins box (solid).All boxes are coupled to each other as one geometrical body. Air and PCM are coupled so energy transfers from air to fin and then from fin to PCM. Using the symmetrical structure of the considered unit, the computational domain is simplified to only one symmetry unit cell in which the planes of symmetry are in the middle of the fin and are in middle between the two subsequent fins, as illustrated in Figure 5.2.

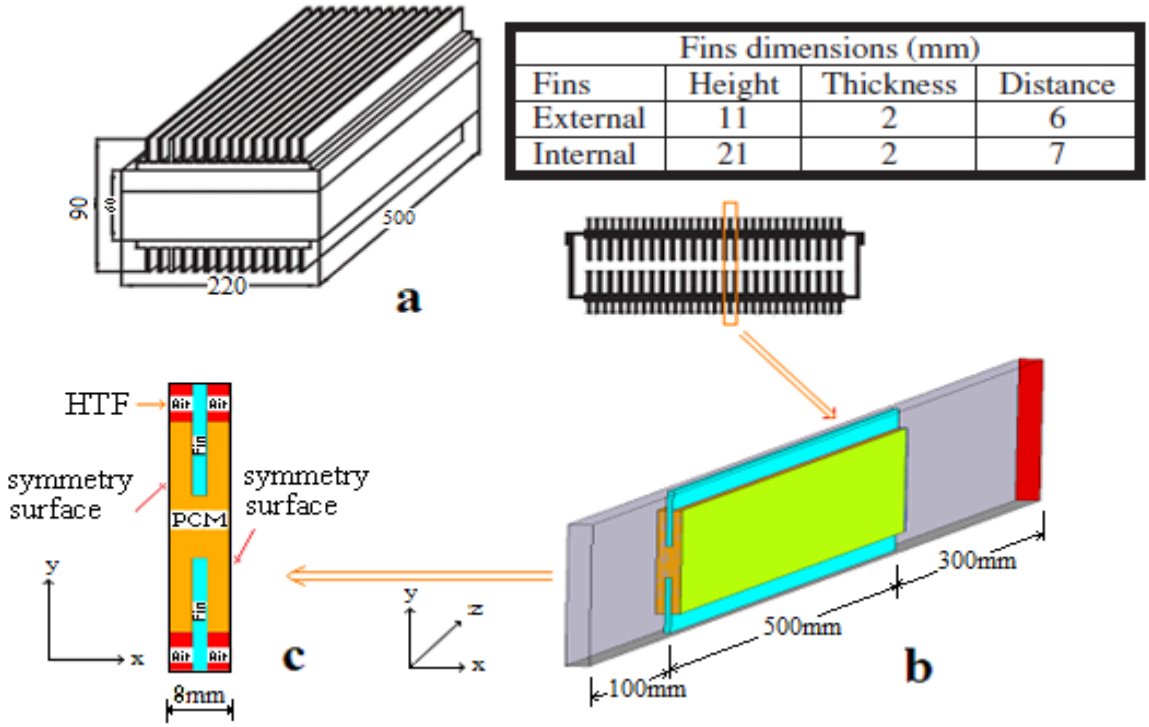

Fins dimensions (mm)			
Fins	Height	Thickness	Distance
External	11	2	6
Internal	21	2	7

Figure 5.2 Geometrical configuration of the latent heat thermal energy storage system (LHTES) : (a) the schematic Figure of LHTES system, Stritih and Butala [74]; (b) three-dimensional of computational domain; (c) cross section of computational domain

5.2.3 Three-dimensional model validation

The proposed model verification was performed by comparing the 3-D model prediction with experimental data of Stritih and Butala [74]. The computational grid was selected based on a grid study for two cases of quadrilateral grid systems. First case (mesh.1) was meshed as follows: bottom fin domain of 100×16×4, fluid of 100×210×8, PCM of 100×68×4, and top fin of 100×16×4. Second case (mesh.2) was chosen, which was meshed of 125×20×4 for bottom fin; 125×20×4 for top fin; 125×91×8 for HTF; 125×102×4 for PCM. After examining the grid refinement, the time step size was set as a variable starting from 10^{-5}s. The convergence criterion is met when the scaled residuals were set to be 10^{-4} for momentum and 10^{-6} for continuity and energy equations.

The following initial and boundary conditions are applied to solve the governing equations:

1. Initial condition

$$t = 0, \qquad T = T_i = 288.15\text{K}$$

$$u = v = 0, \qquad w = 1.5\text{m/s}$$

2. Symmetry boundary conditions

$$\left.\frac{dT}{dx}\right|_{x=0} = \left.\frac{dT}{dx}\right|_{x=L} = 0, \qquad \left. k\frac{dT}{dy}\right|_{y=-H/2} = \left. k\frac{dT}{dy}\right|_{y=H/2} = a\left(T_{out,i} - T_{in,i}\right)$$

where a is the convection coefficient. The three-dimensional physical model was verified by comparing its prediction with experimental data reported by Stritih and Butala [74] with inlet air temperature of $T = 26$℃, velocity = 1.5m/s for the second grid mesh case as shown in Figure 5.3. The entire initial computational domain was set to the ambient temperature. Properties of paraffin RT20, air, and aluminum used are given in Table 5.1. The density of air was modeled with a polynomial function while the properties of aluminum were used in a standard form. Two cases of HTF condition were considered as external boundary condition as follows; Case.1) the inlet air temperature 36℃ and the temperature difference ($\Delta T = T - T_{PCM}$), 16℃, and Case.2) the inlet air temperature 26℃ and the temperature difference 6℃.

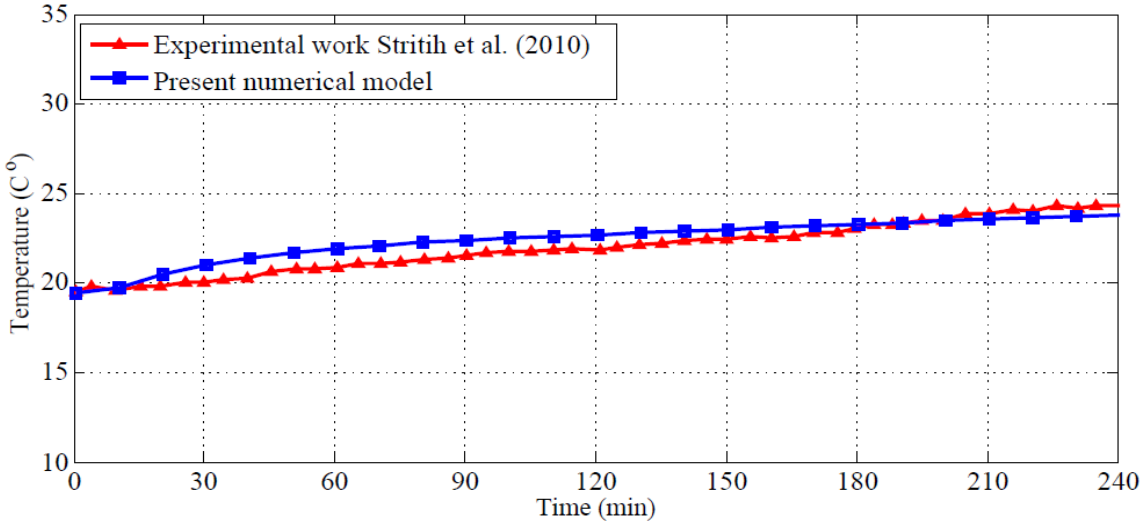

Figure 5.3 Comparison of outlet temperature of storage unit during different time of melting between experimental data and developed numerical model with inlet air temperature of T = 26℃

Table 5.1 Properties of paraffin, air, and aluminum used for calculations

Materials	$\rho(kg/m^3)$	k(W/mK)	c(J/kgK)	μ(kg/ms)
Paraffin	740/(0.001×(T−293.15)+1)	0.15	RT20 (DSC)	0.001×exp(-4.25+1970/T)
Air	$1.2 \times 10^{-5}T^2 - 0.01134T + 3.498$	0.0242	1006.43	1.7894×10^{-5}
Aluminum	2719	202.4	871	-

5.3 Results and discussion of numerical simulation

Figure 5.4 compares the model prediction with the experimental data and with the prediction of the numerical model developed by Stritih and Butala [75]. The prediction of numerical result shows that the transient outlet air temperature is closer to the experimental data at the early stage of the melting process with a maximum discrepancy of 0.5K compared to a numerical solution presented by Stritih and Butala within a maximum discrepancy of 1.5K as shown in Figure 5.4. As time passes, the convective heat transfer plays a role to exchange the thermal energy between the incoming air and PCM. Thus, the general trend of the predictive curve gets aligned with the experimental

data over the transient melting period of the phase change. The experimental measurement was carried out when the indoor/outdoor temperature difference was at 15℃ with a room temperature maintained at 23℃. It should be mentioned that the experimental measurement of the outlet temperature was conducted using a K-type thermocouple with a reading error of ± 1.5℃. After 145 min the outlet air-temperature approaches the inlet air temperature. This is due to the length of the storage unit which is not suitable for more discharging time. In case of the inlet air temperature of 36℃ and air flow of 1.5m/s, the outlet air temperature does not reach the inlet air temperature because of thermal losses to the surroundings. This is attributed to the loss to the room temperature which is maintained at 23℃.

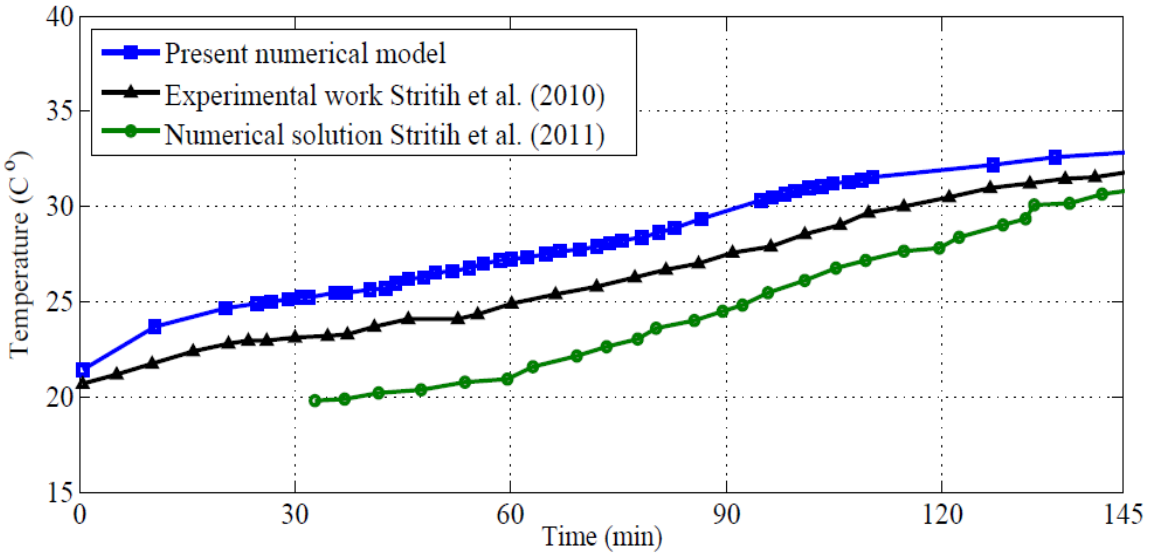

Figure 5.4 Comparison of model prediction of outlet temperature for the mesh.2 (see page 62) with 2-D numerical solution and experimental data Stritih and Butala [75] with inlet air temperature of $T = 36$℃

The experimental observation reported by Stritih and Butala [74] shows that the outlet's LHTES air-temperature is lower when the air flow is of 1.5m/s than that of 2.4m/s. The length of air channel might be not appropriate for air flow larger than 1.5m/s

and it is more effective with inlet air temperature not lower than 30℃. Table 5.2 below shows air cooling time completion, $t_{cooling}$, against the inlet air temperature, T_i, and air flow rate.

Table 5.2 Completion time for cooling at two different inlet air conditions

Air flow		Inlet air temperature	
		36℃ (min)	40℃ (min)
1.5 m/s	Experimental work [74]	150	110
	Numerical prediction	146	119
2.4 m/s	Experimental work [74]	140	100
	Numerical prediction	120	98

Figure 5.5 presents the comparison between the numerical result and experimental work [74] for 3-D diagram of completion's air cooling. This graph is obtained from the surface plane for simulation of two cases of the inlet air conditions (i.e., T_i=36, 40℃) with two different scenarios of air flows (i.e., u_i=1.5, 2.4m/s). The numerical model prediction is in a good agreement with the experimental data. The computational result of completion's air cooling time of the LHTES system varies within 2% to 8% for air flow of 1.5m/s. During the numerical calculations, the variation of PCM's thermo-physical with temperature and also the volume expansion due to the phase change are taken into account by leaving 18% filled up with air above PCM of the total PCM enclosed space. However, a slight deviation is found when the flow rate is of 2.4m/s. The possible reason can be attributed to the length of air channel that is located at over and bottom of the PCM's metal box is not appropriate for flow rate higher than 1.5m/s as Stritih and Butala [74] reported in their experimental observations. Therefore, the predicted results can be

acceptable as a guide manual to design a practical engineering of LHTES model for cooling applications.

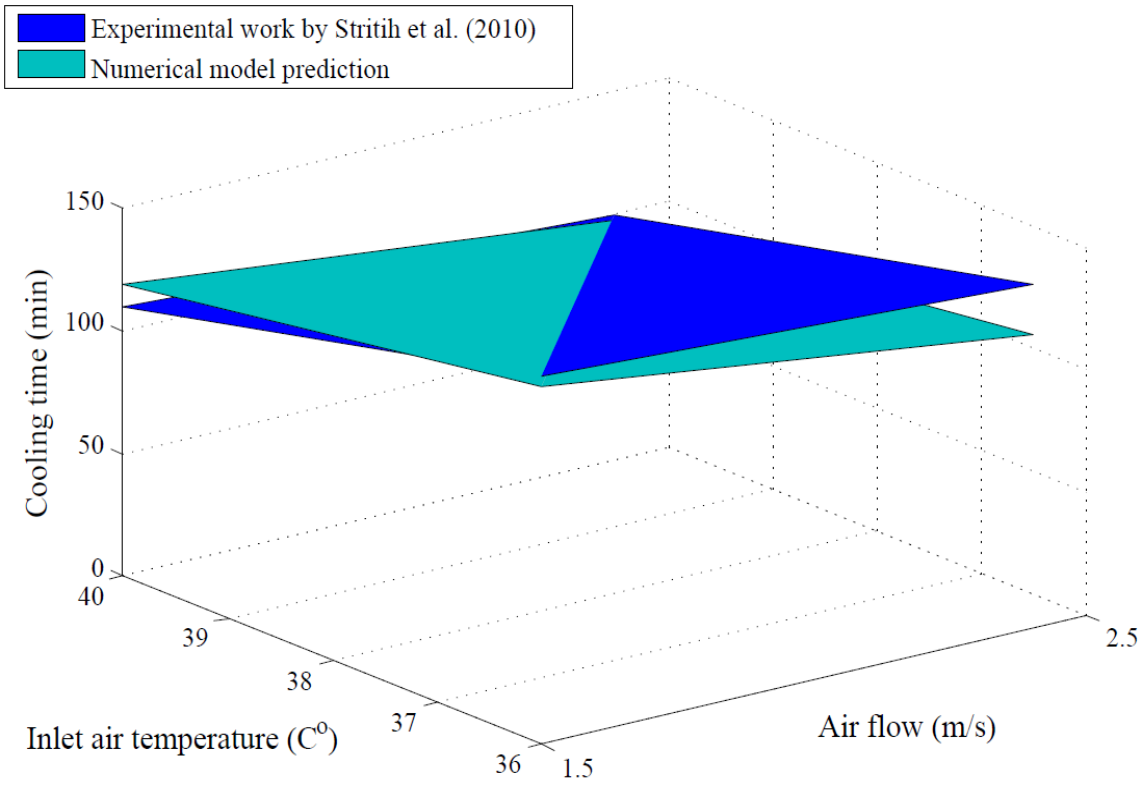

Figure 5.5 The comparison of air cooling time completion between the present numerical model and the experimental work [74]

5.3.1 Numerical computations and mesh evaluation

The governing equations are solved numerically using CFD commercial package. The grid dependency on the solution is tested for several grid resolutions. Typically, three different sizes of the centralized LHTES system are studied, 500mm, 650mm, and 750mm. The available pressure-velocity coupling schemes, SIMPLE is used. Multiphase model is implemented for two Eulerian phases. Explicit scheme is used to calculate volume fraction parameters with 0.25 Courant number. The modelling is conducted using

finite-volume CFD code, Fluent. A segregated solver has been used to numerically solve the melting 3-D Navier-Stokes and energy equations. The PCM-air volume of fluid (VOF) model is implemented to deal with the changes of the phase change volume expansion and to track the fluid volume fraction throughout the domain. In the VOF model, the Geo-Reconstruct model which is the volume fraction spatial discretization is used to solve the face fluxes when the cell is near the interface between two phases. The pressure staggering option (PRESTO) scheme uses the discrete continuity balance to compute the staggered pressure for a staggered control volume about the face. Viscous model is used to set parameters for laminar flow (the same model can be used for inviscid and turbulent flow). The under-relaxation factors for the pressure, density, momentum, liquid fraction updates, and energy are set to be 0.3, 1, 0.7, 0.9, and 1, respectively. Time step independent solutions are obtained using a variable time stepping within a minimum time step size of 10^{-5}s to a maximum time step size of 1s. Several grid resolutions are evaluated based on the experimental data of the cooling completion time with inlet air conditions as shown in Table 5.2. All examined grid resolutions yield an acceptable accuracy of the cooling completion time estimation for the discharging process. However, the minimum computation time is found 3days 4hr and 55min for the storage unit of 500mm length. To save computing time without sacrificing of desirable accuracy, the grid system shown in Table 5.3, can be regarded as grid independent and sufficient to perform the numerical investigation purposes with using quadrilateral/hexahedral meshes. However, a hexahedral cell demands more CPU and memory than a tetrahedral cell.

Table 5.3 Three computational grids resolutions

Domain	LHTES's length of 500mm Cells	LHTES's length of 650mm Cells	LHTES's length of 750mm Cells
HTF (air)	90550	141720	156920
Fin bottom	11500	20480	25600
Fin top	17250	20480	25600
PCM	71300	108800	138800
PCM air	9200	16320	21600
All Domains	199800	307800	368520

5.3.2 Effective heat capacity

The effect of initial condition of temperature on the thermal performance of LHTES system was investigated using four different initial conditions. As expected, it is found that the rate of melting increases with increasing initial temperature as shown in Figure 5.6. Low melting temperature differences lead to increasing rate of melting. To assess the effect of effective heat capacity of the system, three different approximations of the effective heat capacity are studied (see Figure 5.7). The first is based on the differential scanning calorimeter (DSC) measurement, while the second and third approximations are chosen for which the phase change temperature range, dT_P, equals 4K, and 6K , respectively, according to the function used by Medved and Arkar [46]. It is noted that the effective heat capacity measured by DSC is more reliable because commercially available PCMs have a wide temperature range of the phase change.

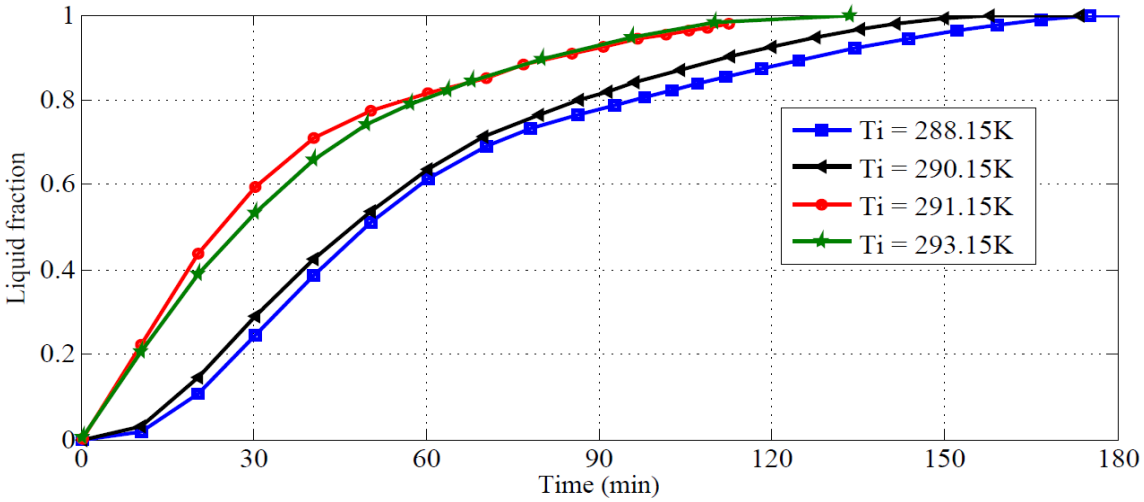

Figure 5.6 Liquid fraction of melting evolution at different inlet temperature of boundary conditions

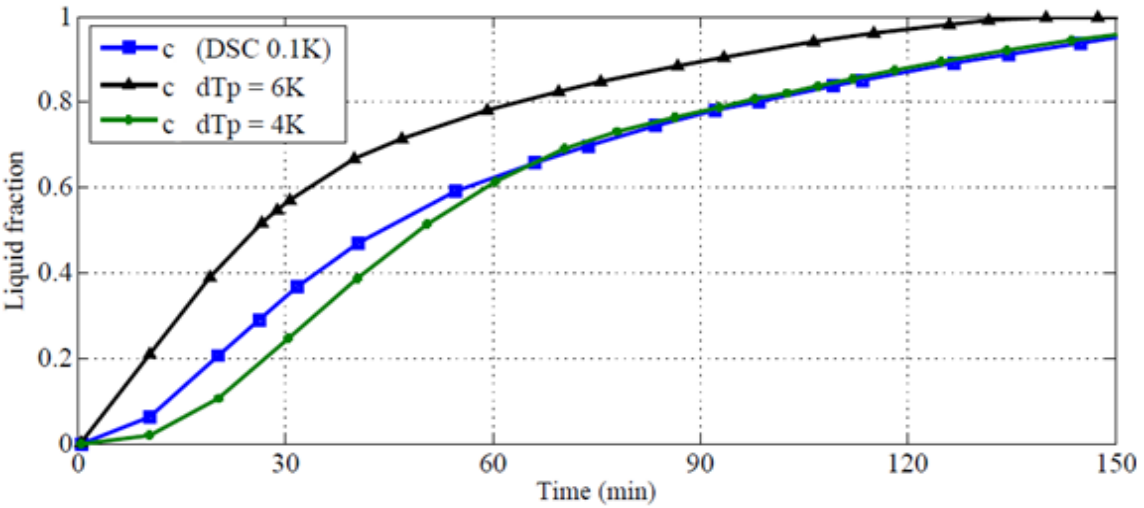

Figure 5.7 Liquid fraction for different effective specific heat capacity of RT20 paraffin measured using DSC test with cooling rate of 0.1K/min and with different melting range temperature *dTp*

Figure 5.8 illustrates the computed liquid and solid fractions of the centralized LHTES system as a function of time. The y-axis on the left side of Figure 5.8 presents the liquid fraction, for non-melting to complete melting. For long-scale time simulation, the behavior of the system shows a similar trend for various inlet temperatures. Therefore, the relation between the liquid fraction and the discharging time (min) for case.1 is

correlated using curve fitting to the numerical results obtained that are plotted on Figure 5.8. The equation obtained is of a third degree polynomial and can be written as;

$$Liquid\ fraction = -3.852 \times 10^{-6}t^3 + 3.604 \times 10^{-4}t^2 - 1.396 \times 10^{-3}t$$

$$(R^2 = 0.9988) \qquad (5.17)$$

Similarly, the relation between the solid fraction and the charging time (min) can be written as following:

$$Solid\ fraction = 1.339 \times 10^{-9}t^4 - 9.084 \times 10^{-7}t^3 + 2.645 \times 10^{-4}t^2$$

$$- 2.538 \times 10^{-2}t\ (R^2 = 0.9983) \qquad (5.18)$$

As can be seen from Figure 5.8 the solid fraction increases rapidly at early stage of the charging period due to relatively small thermal resistance between the aluminum walls and the PCM. However, when the charging period prolongs, the solidified layers of PCM cause an increase of thermal resistance to the heat transfer.

The distribution of melting front and solid fraction provides useful information for practical application of a hybrid PCM closed system based multi-fin heat sink.

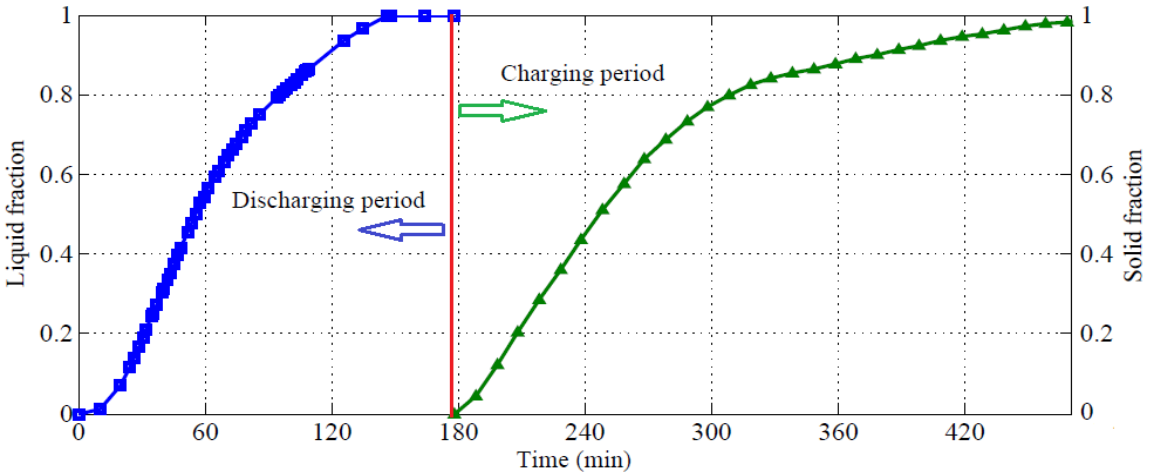

Figure 5.8 Liquid fraction during discharging time and solid fraction during charging time

5.3.3 Temperature Difference

The transient heat flux for two cases of inlet temperature of HTF is illustrated in Figure 5.9. The curves are for $\Delta T = 16℃$ and 6℃. It is observed that the transient heat flux drastically decreases at early stage of discharging time caused by the strong influence of diffusion through the lateral heating surface. The result reveals that the higher temperature difference (ΔT), results in a higher release of heat flux at the beginning of melting process. Accordingly, the discharging period shortens and the transient heat flux reduces. During prolong melting time the thermal resistance of the growing layer thickness is significantly increased leading to a decrease in the surface heat flux. The effect of buoyancy plays a role in reducing the rate of heat flux and, hence, prolonging the discharge period. This situation is more pronounced in case.2.

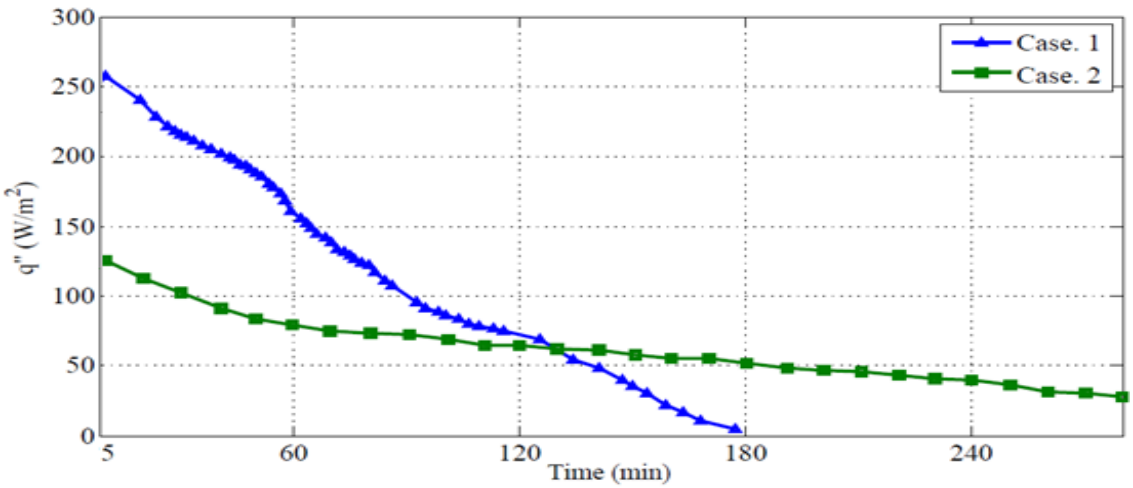

Figure 5.9 Heat transfer rate during melting period for two different inlet air temperatures, 36℃, and 26℃

Figure 5.10 (a) demonstrates the transient heat flux for case.1 for both discharging and charging periods. Both the melting and the solidification processes are simulated to analyze the heat transfer performance. The total energy released from the PCM is

portrayed for two cases of interest. As expected, the total energy stored increases with increasing temperature difference as shown in Figure 5.10 (b).

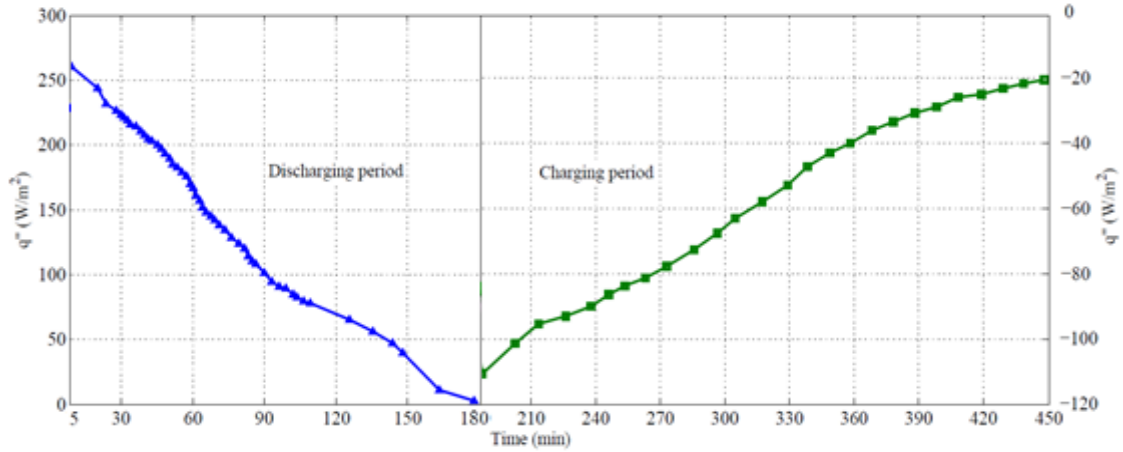

Figure 5.10 (a) Transient heat flux releasing from the PCM during discharging time and storing during charging time (case.1)

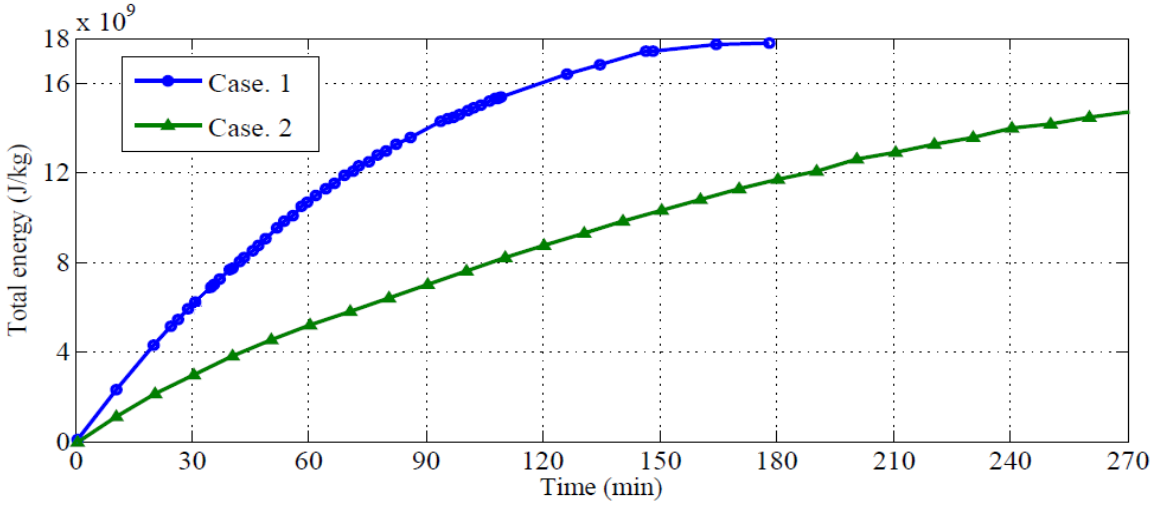

Figure 5.10 (b) Total energy releasing from the PCM during discharging time for two cases of inlet air conditions

5.3.4 Normalization analysis of the results

The computational results of evolution of melting front are employed to describe the fluid flow and heat transfer characteristics. For generalization, the dimensionless Fourier number is used as a common approach to explain the transient heat conduction.

Fourier number is defined as a measure of conducted heat within a body relative to the stored heat, $F_o = \alpha t / {l_c}^2$, where α is the thermal diffusivity of the PCM and l_c is the characteristic length (half thickness of the PCM layer). To accommodate the phase change processes, however, Fourier number needs to be combined with Stefan number. Stefan number is defined as the ratio of sensible heat to latent heat, $Ste = c\,\Delta T / L$, where c is the specific heat capacity of the PCM, ΔT is the temperature difference between the free stream of air temperature and the PCM average melting temperature, and L is the latent heat. The product of Fourier number and Stefan number, $F_o Ste$ acts as an independent dimensionless parameter that defines the transient heat conduction and phase change processes.

The governing equation can be written in dimensionless from. The following parameters are the dimensionless variables and groups that are introduced for analysis

$X^* = \frac{x}{l}$, $Y^* = \frac{y}{l}$, $Z^* = \frac{z}{l}$, $P^* = \frac{(P - P_\infty)}{\rho\, u_\infty^2}$, $U^* = \frac{u}{u_\infty}$, $V^* = \frac{V}{u_\infty}$, $W^* = \frac{w}{u_\infty}$, $\theta = \frac{T - T_\infty}{T_m - T_\infty}$,

$t^* = \frac{t\, u_\infty}{l}$, $g^* = \frac{g}{(u_\infty^2 / l)}$, $R_e = \frac{\rho\, u_\infty l}{\mu}$, $P_r = \frac{\mu\, c}{K} = \frac{\vartheta}{\alpha}$, $Ste = \frac{c\,(T_m - T_\infty)}{\Delta H}$, $A^* = \frac{A}{(\rho u_\infty / l)}$

, $\psi = \frac{\Delta H}{L}$

The dimensionless continuity, momentum, and energy equations can be expressed as;

$$\frac{\partial U^*}{\partial X^*} + \frac{\partial V^*}{\partial Y^*} + \frac{\partial W^*}{\partial Z^*} = 0 \tag{5.19}$$

$$\frac{\partial U^*}{\partial t^*} + U^* \frac{\partial U^*}{\partial X^*} + V^* \frac{\partial U^*}{\partial Y^*} + W^* \frac{\partial U^*}{\partial Z^*} = \frac{1}{Re}\left[\frac{\partial^2 U^*}{\partial {X^*}^2} + \frac{\partial^2 U^*}{\partial {Y^*}^2} + \frac{\partial^2 U^*}{\partial {Z^*}^2}\right] - \frac{\partial P^*}{\partial X^*} + A^* U^* \tag{5.20}$$

$$\frac{\partial V^*}{\partial t^*} + U^*\frac{\partial V^*}{\partial X^*} + V^*\frac{\partial V^*}{\partial Y^*} + W^*\frac{\partial V^*}{\partial Z^*}$$

$$= \frac{1}{Re}\left[\frac{\partial^2 V^*}{\partial X^{*2}} + \frac{\partial^2 V^*}{\partial Y^{*2}} + \frac{\partial^2 V^*}{\partial Z^{*2}}\right] - \frac{\partial P^*}{\partial Y^*} + A^*V^* + \frac{Ra}{Re^2 Pr} \quad (5.21)$$

$$\frac{\partial W^*}{\partial t^*} + U^*\frac{\partial W^*}{\partial X^*} + V^*\frac{\partial W^*}{\partial Y^*} + W^*\frac{\partial W^*}{\partial Z^*}$$

$$= \frac{1}{Re}\left[\frac{\partial^2 W^*}{\partial X^{*2}} + \frac{\partial^2 W^*}{\partial Y^{*2}} + \frac{\partial^2 W^*}{\partial Z^{*2}}\right] - \frac{\partial P^*}{\partial Z^*} + A^*W^* \quad (5.22)$$

$$\frac{\partial \theta^*}{\partial t^*} + U^*\frac{\partial \theta^*}{\partial X^*} + V^*\frac{\partial \theta^*}{\partial Y^*} + W^*\frac{\partial \theta^*}{\partial Z^*}$$

$$= \frac{1}{Re\ Pr}\left[\frac{\partial^2 \theta^*}{\partial X^{*2}} + \frac{\partial^2 \theta^*}{\partial Y^{*2}} + \frac{\partial^2 \theta^*}{\partial Z^{*2}}\right]$$

$$+ \frac{1}{Ste}\left[\frac{\partial \psi}{\partial t^*} + U^*\frac{\partial \psi}{\partial X^*} + V^*\frac{\partial \psi}{\partial Y^*} + W^*\frac{\partial \psi}{\partial Z^*}\right] \quad (5.23)$$

In addition, melting fraction of the PCM and Nusselt number are employed as two dependent dimensionless parameters. Nusselt number can be introduced as:

$$Nu = \frac{q''}{\Delta T}\frac{l_c}{k_{PCM}} \quad (5.24)$$

where q'' is the mean heat flux, ΔT is the temperature difference between the free stream of air temperature and the PCM average melting temperature, l_c is a half thickness of the PCM layer equals to 0.004m, and k_{PCM} is the thermal conductivity of the PCM. Rayleigh number (Ra) which is associated with buoyancy driven flow in fluid has to be determined to take into account the effect of convection during melting stage. The dimensionless form of temperature can be expressed as follows:

$$\theta = (T - T_m)/(T_i - T_m) \quad (5.25)$$

where T_m is the mean melting temperature of the PCM, and T_i is the inlet air temperature.

$$Ra = \frac{g\gamma\Delta T {l_c}^3 \rho}{\mu\alpha} \tag{5.26}$$

The average Nusselt number of Nu is correlated according to Pal et al. [103] as follows;

$$\overline{Nu} = 0.01559\left[\frac{Ra^{1/5}}{Ste.Fo}\right]^{0.4} \tag{5.27}$$

Figures 5.11 (a) and 5.11 (b) illustrate the melt fraction and the dimensionless temperature versus the product of Fourier and Stefan numbers ($F_o\,Ste$) for cases 1, and 2, respectively. The melting fraction increases clearly for relatively small values of $F_o\,Ste$. It is noticeable from Figure 5.11 (a) that plotting the melting fraction against $F_o\,Ste$ has a remarkable uniformity for two cases of HTF. This indicates that $F_o\,Ste$ could be used to generalize the result for different cases of hot or cold HTF passing over a centralized LHTES unit. As shown in Figure 5.11 (b), the dimensionless temperature for two cases is not identical. This deviation is attributed to the temperature variation in the molten PCM during early stage which became more uniform with time. It is worthwhile to notice that the dimensionless temperature increases as ΔT increases for a given $F_o\,Ste$ (independent dimensionless parameter) because the temperature in liquid PCM is higher than that in solid−liquid interface. When the value of $F_o\,Ste$ reaches about 8.2, the corresponding value of the dimensionless temperature is 0.65. It can be seen that the intersection point between two cases occurs at 0.65 of dimensionless temperature scale. Thus, from Eq. (5.25), it is concluded that the performance of LHTES system is enhanced when the temperature difference between the ambient air at the inlet of LHTES system and the PCM mean melting temperature is higher by about 10K.

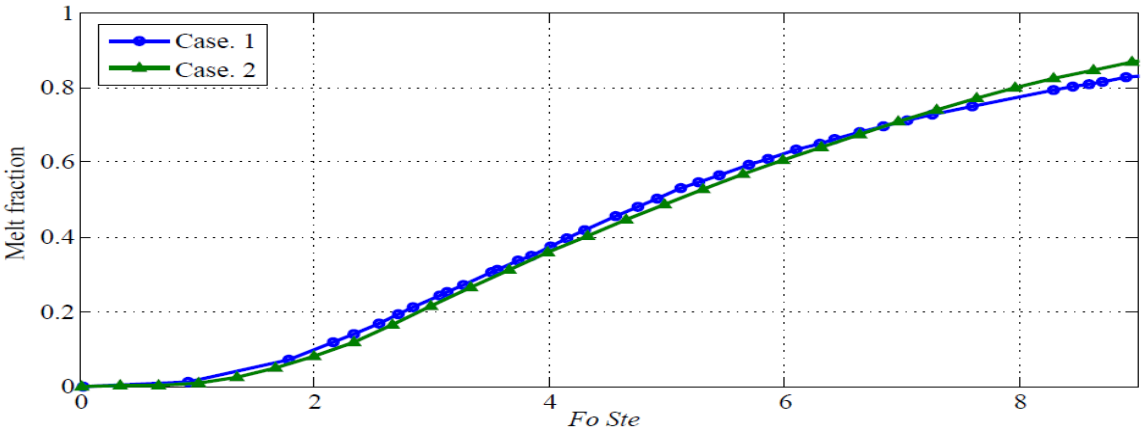

Figure 5.11 (a) The melt fraction versus the product of Fourier and Stefan numbers (*Fo Ste*) for two cases of inlet air conditions

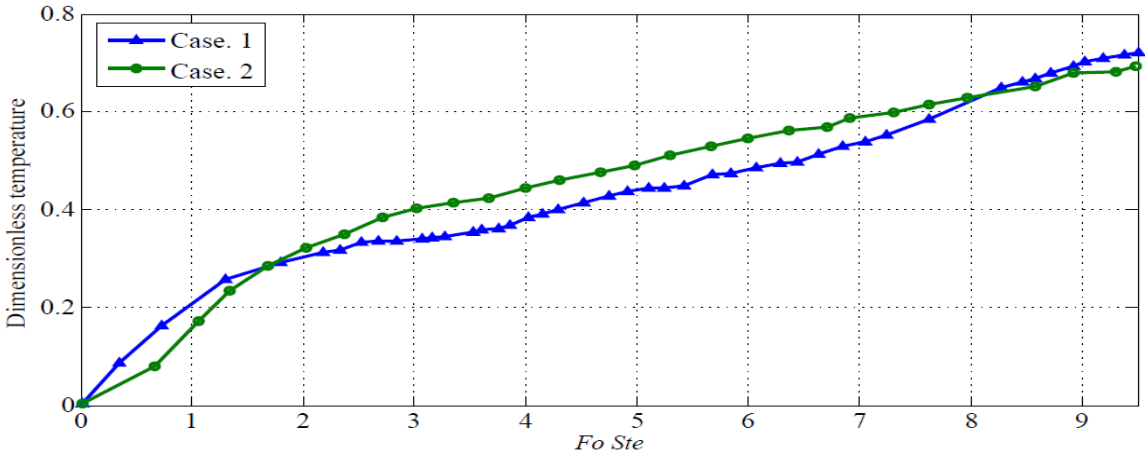

Figure 5.11 (b) The dimensionless temperature versus the product of Fourier and Stefan numbers (*Fo Ste*) for two cases of inlet air conditions

The convective heat transfer of melted liquid has a potential effect to increase the melting rate. To include the effect of convective heat transfer in the liquid PCM, the Rayleigh number is scaled into dimensionless time and normalized with $Ra^{1/5}$, as a scaled parameter of $\left(Ste.F_o/Ra^{1/5}\right)$ as shown in Figures 5.12 (a) and 5.12 (b). The power of Rayleigh number is selected based on natural convection laminar flow for a vertical surface. However, Figures 5.12 (a) and 5.12 (b) for the melting fraction and the

dimensionless temperature against $Ste.F_o/Ra^{1/5}$ respectively, appear to be slightly different due to non-isothermal boundaries. Figure 5.12 (b) shows the data for two cases collapse on a single curve when the scaled dimensional time approaches 0.035.

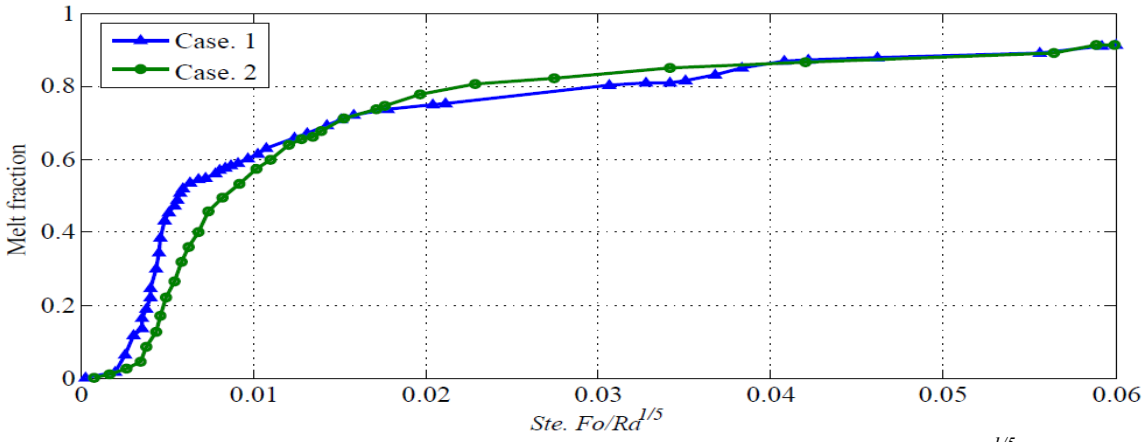

Figure 5.12 (a) The melt fraction versus the scaled dimensionless time (*Ste. Fo/Ra*$^{1/5}$) for two cases of inlet air conditions

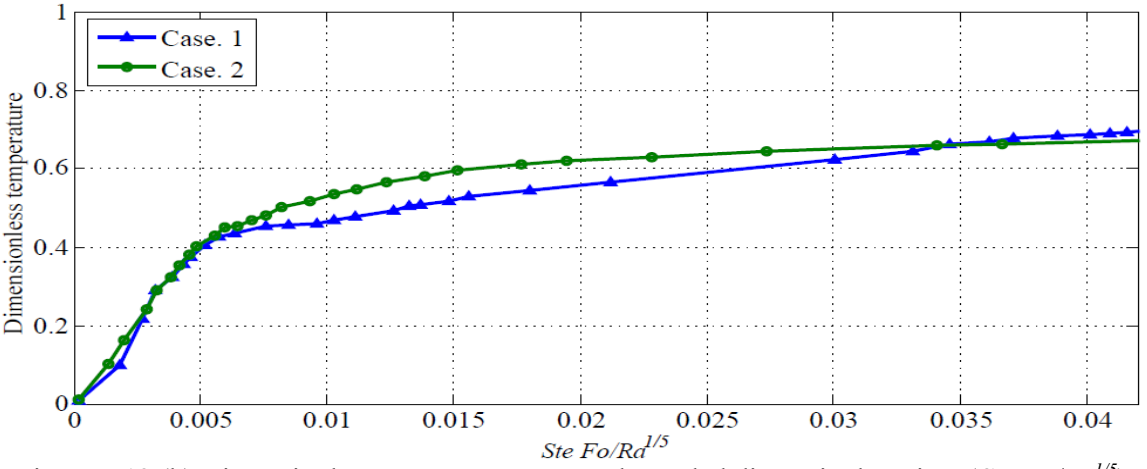

Figure 5.12 (b) Dimensionless temperature versus the scaled dimensionless time (*Ste.Fo/Ra*$^{1/5}$) for two cases of inlet air conditions

As can be seen from Figures 5.13 (a), (b), (c), (d), the dimensionless scaled time decreases from 0.02 to 0.004 for four different inlet air-temperatures (i.e. 26, 30, 36, and 40°C). Those graphs were obtained from the numerical calculations of HTF heat transfer

at the inlet and outlet of the centralized LHTES system. Fourier number was determined by accounting it at each time step over the entire melting process involving the selected PCM thermo-physical properties represented by Stefan number such as thermal conductivity, density, viscosity, specific heat capacity, the mean melting point, and latent heat of fusion. As the inlet air-temperature was approximately defined, which was limited to be in range of 26 to 40℃, the Rayleigh number was estimated. The melt fraction, then, can be determined at each time until it reaches the unity for melting completely case.

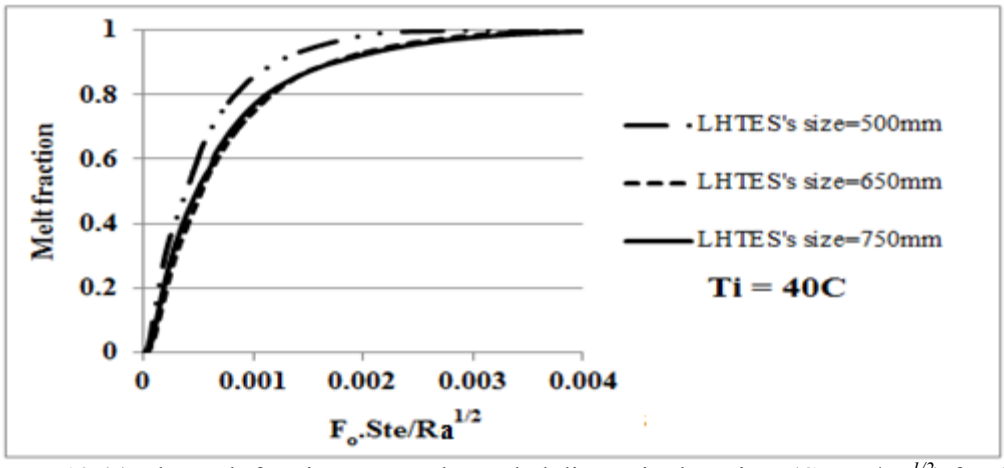

Figure 5.13 (a) The melt fraction versus the scaled dimensionless time ($Ste.F_o/Ra^{1/2}$) for three sizes of LHTES systems at the inlet air temperature of 40℃

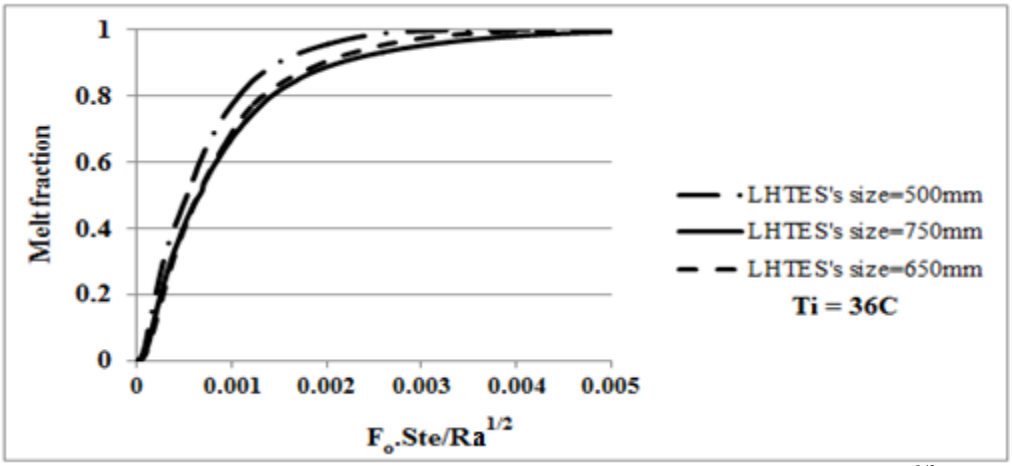

Figure 5.13 (b) The melt fraction versus the scaled dimensionless time ($Ste.F_o/Ra^{1/2}$) for three sizes of LHTES systems at the inlet air temperature of 36℃

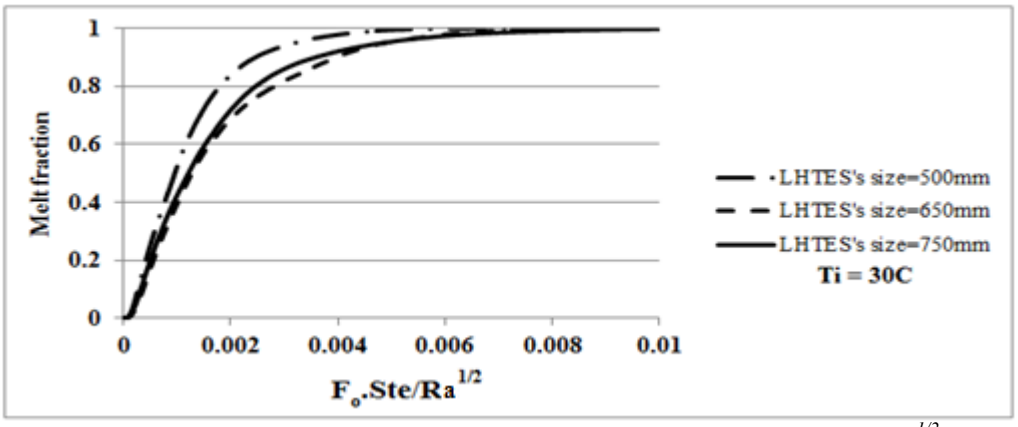

Figure 5.13 (c) The melt fraction versus the scaled dimensionless time ($Ste.F_o/Ra^{1/2}$) for three sizes of LHTES systems at the inlet air temperature of 30℃

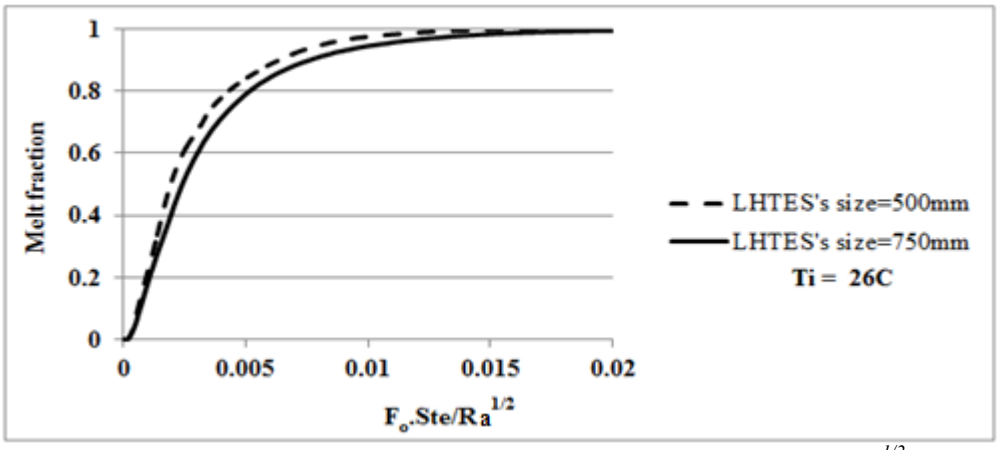

Figure 5.13 (d) The melt fraction versus the scaled dimensionless time ($Ste.F_o/Ra^{1/2}$) for two sizes of LHTES systems at the inlet air temperature of 26℃

In general, Figure 5.14 shows a linear relation between the melt fractions multiplied by reciprocal of the Stefan number ($\varepsilon.Ste^{-1}$) and the ratio of the dimensionless heat release completion time ($F_o/(F_o)_t$) for four cases of the inlet air-temperature with three LHTES's sizes. As the melt fraction was determined based on the inlet air condition and the thermo-physical properties of the selected PCM, the determined value on the *x*-axis is intersected with the specific temperature line to figure

out the best size of LHTES system with a lower ratio of the dimensionless heat release completion time. This figure was performed to take into account the completion time required for the entire melting process. For example, when the PCM completely melts, the melt fraction (ε) and the ratio of the Fourier number are equal to unity. Hence, the LHTES system can be selected based on the inlet air-temperature and the available PCM thermo-physical properties.

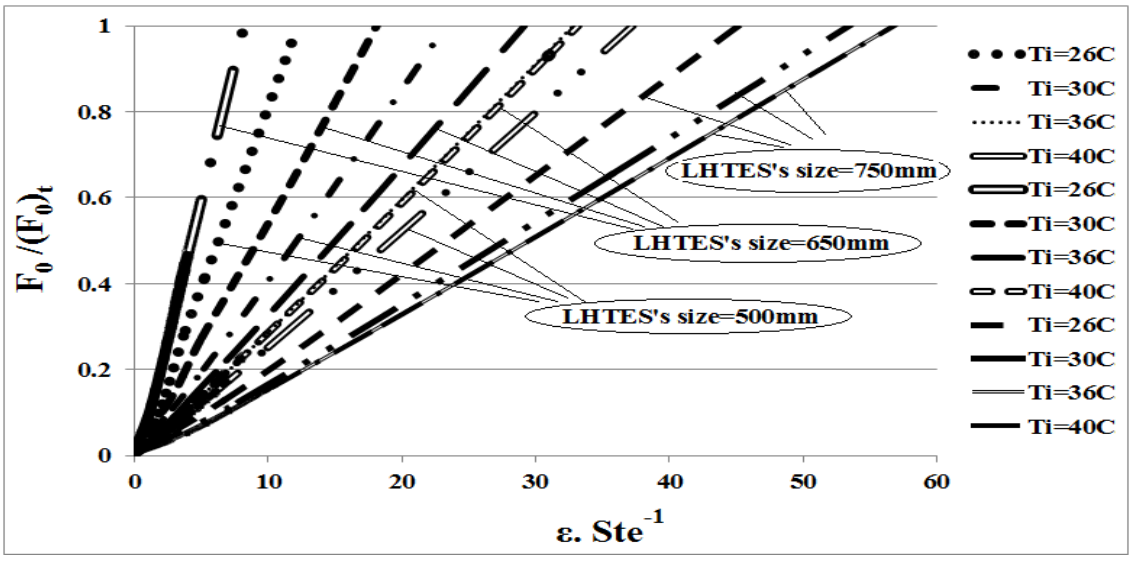

Figure 5.14 The dimensionless of completion melting time ratio versus the combined term of the melt fraction multiplied by the reciprocal of the Stefan number for four different inlet air temperatures at three sizes of LHTES systems

The completion time of the melting process, as can be seen from Figure 5.15, which is presented by the Fourier number, approaches about 30 and 20 for the LHTES systems' sizes of 650 and 500mm, respectively. Meanwhile, it reaches about 40 for the LHTES system's sizes of 750mm. This graph can be used to select an appropriate size of the LHTES system. As the inlet air-temperature of HTF, the thermo-physical properties of a potential PCM, and the estimated time for discharging period are defined, the Fourier

and Stefan numbers can be calculated. Then, their values are assigned on the Figure 5.16 to select the proper size of LHTES within the inlet air-temperature range.

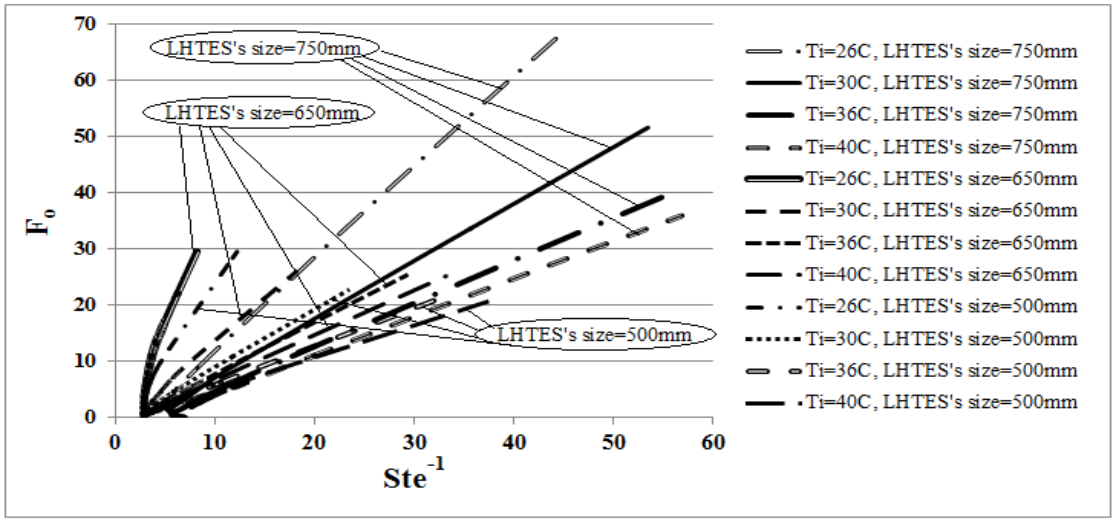

Figure 5.15 The dimensionless of completion melting time versus the reciprocal of the Stefan number for four different inlet air temperatures at three sizes of LHTES systems

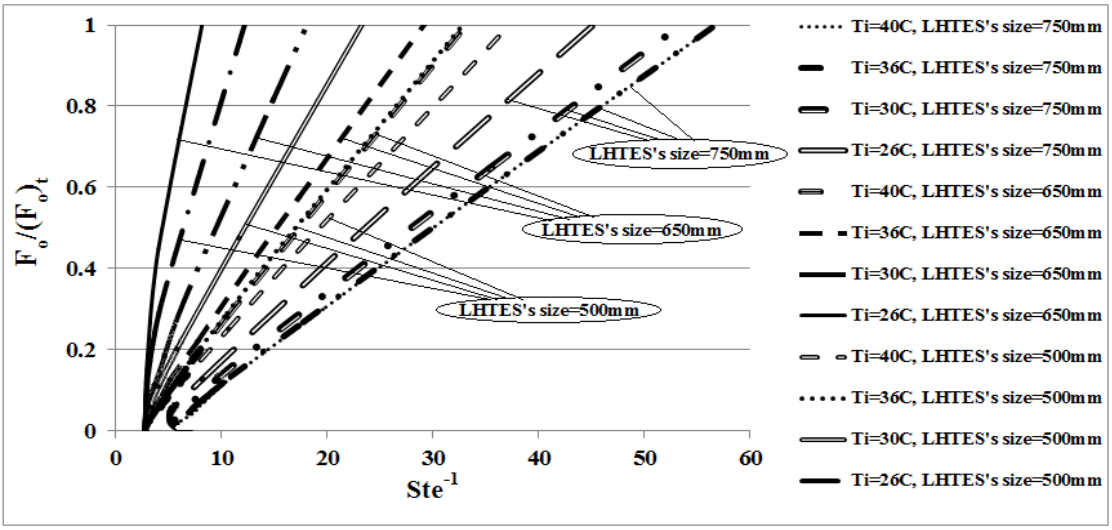

Figure 5.16 The dimensionless of completion melting time versus the reciprocal of the Stefan number for four different inlet air temperatures at three sizes of LHTES systems

Illustrative example to determine a LHTES's size is demonstrated for a selected PCM to which the inlet air-temperature of 36℃ and the inlet velocity of 1.5m/s are

predefined. For approximately 3.0hr of the discharging period, the thermo-physical of a potential PCM was assumed to have the thermal diffusivity of $3.49\times10^{-8}m^2/s$, the Fourier, Stefan, and Rayleigh numbers thus can be calculated (i.e F_0 =25.3, *Ste* =0.034, and *Ra* =23279). Figure 5.15 might be used to provide an initial guess for the Stefan number value. Using Figure 5.13 (b), the melt fraction can be determined (i.e. ε =0.95). Thereafter, Figure 5.14 is used to identify the LHTES's size by assigning the value of ($\varepsilon.Ste^{-1}$) and then crossing with a temperature line of 36℃. The intercepted temperature line points the LHTES's size which needs to be selected.

5.3.5 Transient analysis of charging and discharging performances

The results for melting and solidification processes are depicted in Figures 5.17 (a) and 5.17 (b), respectively. Figure 5.17 (a) shows the melting simulation in the form of solid−liquid phase distribution. The first picture (10.4min) shows the early stage of melting where the whole domain is still in solid state as presented in blue color. There are zones with red color at the top and bottom of the computational domain forming the hot air channels HTF. The PCM is gradually melting with time and associated with mushy zone, which is shown in green color. The melted zone of PCM has a red color similar to HTF color. By increasing the evolution period of melting, the growth of liquid fraction is accordingly pronounced.

The PCM starts melting in the vicinity of the fins at the top and bottom partitions due to their relatively high thermal conductivity. Thus, the heat transfer from the fin to the PCM initially occurs by conduction and later by natural convection. However, the gravity acts to draw down the liquid PCM from the top to the bottom resulting in an

increased in convection and hence an increase in the rate of melting. Thus, the liquid PCM near the fin and heated surface forced to flow up due to the influence of buoyancy. At the start of the melting process, the velocity of the liquid PCM is relatively small. The convection mode of heat transfer becomes dominant until the magnitude of liquid velocity drops because the temperature difference is more likely to be uniform.

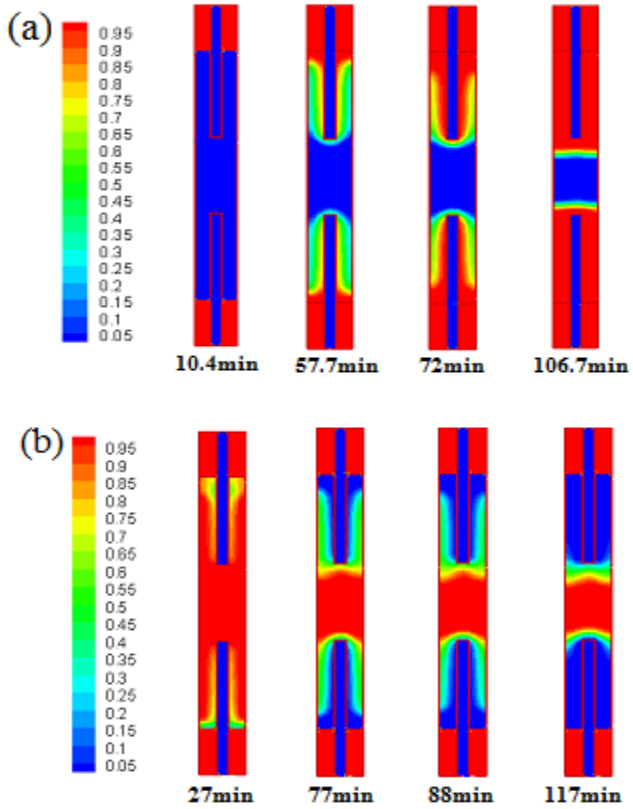

Figure 5.17 (a) The liquid fraction and phase distribution of PCM as a function of time during melting process of energy release. (b) The liquid fraction and phase distribution of PCM as a function of time during solidification process of energy storage at the inlet air temperature of 36℃ and the velocity of 1.5m/s

Figure 5.17 (b) shows a typical evolution of solidification solid−liquid phase distribution as a function of time for vicinity of the fins. Solid layers start developing in parallel of the cooling walls at the top and bottom of the LHTES system. The solid

interface shape is formed in a way resembling the lateral fin surface. The position of solid interface can be determined to identify the speed of solidification evolution.

5.3.6 Heat flow performance and flow characteristics

Figures 5.18 and 5.19 show the three-dimensional contour images of the temperature distribution at different stages of melting and solidification processes for case.1, respectively. Figure 5.18 shows four different simulation times of melting process. At the early stage, the heat is transferred by conduction from the fin to the PCM; the conduction mode dominants through the whole system. In general, the distribution of melting front is most likely to match the melting temperature distribution.

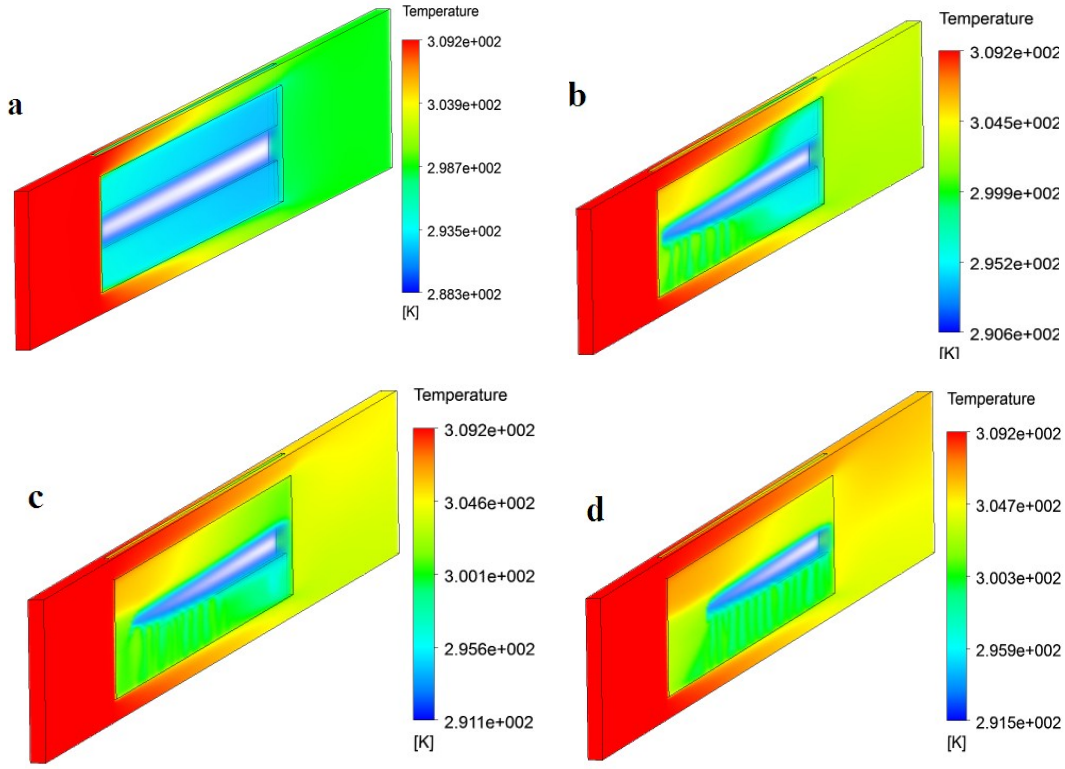

Figure 5.18 PCM temperature contours for the evolution of melting process at case.1 (a) t =1208s (b) t = 4590s (c) t = 5680s (d) t = 6440s

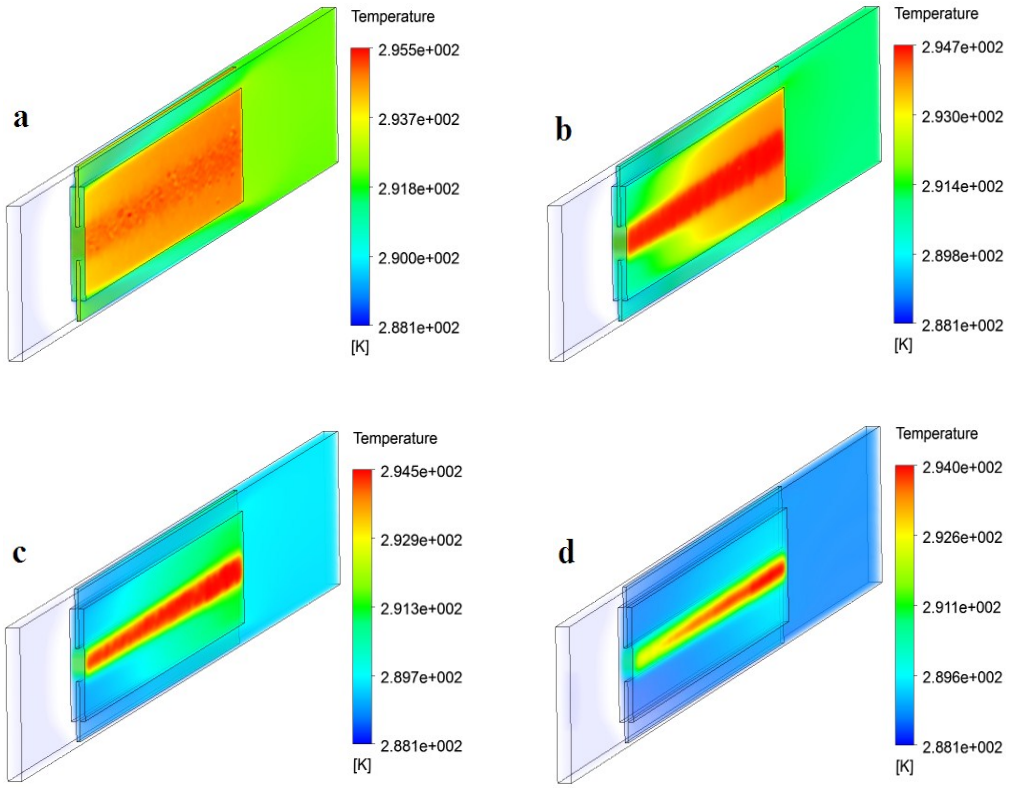

Figure 5.19 PCM temperature contours for the evolution of solidification process at case.1 (a) t = 2424s (b) t = 6624s (c) t = 11424s (d) t = 17424s

A solidification process for case.1 is modeled and presented in the form of the temperature profile contours for four different solidification time, see Figure 5.19. The effect of heat conduction mode on the solid−liquid interface position is significant compared to the effect of free convection as reported by Kroeger and Ostrach [104].

5.4 Fan power and cooling load calculations of the centralized LHTES system

This section presents fan power and cooling load calculations of the LHTES system. Three LHTES systems were modeled to evaluate their optimal performances at four cases of the inlet air-temperatures. Numerical computations and mesh evaluation

were demonstrated. Finally, the dimensionless analysis of LHTES systems' thermal performances was characterized.

5.4.1 Convective heat transfer (h) calculations

The value of convective heat transfer is calculated from velocity of the inlet air stream using empirical data for spiral wire fins provided by the manufacturer (SHE, Lincoln) [105];

$$h = -8 * u^2 + 48.2 * u + 7.4 \ (\mathrm{W/m^2K}) \qquad (5.28)$$

where u is the average air-flow velocity (m/s).

5.4.2 Fan power calculation

The power needed to meet the free cooling requirement can be calculated as following [106]; The static pressure caused by the temperature differences between inlet and outlet air can be written in the form;

$$\Delta P_s = P_{out} - P_{in} \qquad (5.29)$$

Velocity pressure can be defined as the total pressure which measured in the flow direction and it should be less that the static pressure. From a typical graphical illustration of the performance characteristic of a fan at 50% of maximum free delivery air flow, the following characteristics can be provided [107]; The total differential pressure 94%; total fan static differential pressure 79%; fan total efficiency 0.76; fan static efficiency 0.63; power input the fan shaft 50%; power factor 0.99; motor efficiency 0.82. The total differential pressure across the fan can be calculated from the following formula;

$$\Delta P_T = \Delta P_v - \Delta P_s \qquad (5.30)$$

where ΔP_v is the velocity pressure at the outlet (Pa), ΔP_s is the static pressure (Pa, gauge).

The average velocity of air (m/s) can be obtained at standard conditions of 20℃ and 101.325kPa barometric pressure.

$$v = 1.30 \times (\Delta P_v)^{0.5} \qquad (5.31)$$

The volumetric air flow rate of a fan (L/s), can be introduced as;

$$V_F = K_V \times v \times A_d \times 1000 \qquad (5.32)$$

where K_V is the coefficient of fan volumetric flow rate which is approximated by 1.1, and A_d is the cross sectional area of a duct (m^2), 1000 is used for unit conversion.

Fan power, (W) can be determined as;

$$N_F = K_F \times \Delta P_T \times V_F/(\eta_F \times \eta_m) \qquad (5.33)$$

where K_F is the coefficient of electrical capacity which is 0.99; η_F and η_m are the fan and motor efficiencies,0.99,0.82, respectively. The calculated pressure drop of the air stream from the inlet to the room is 3.5kPa and the required fan power is 130W for the inlet air velocity of 1.5m/s.

5.4.3 Cooling load calculations

Cooling factor, ξ, of the centralized LHTES's thermal performance is defined as the ratio of difference temperatures between the inlet and outlet air and between the inlet and PCM mean melting point during discharging period.

$$\xi = (T_i - T_o)/(T_i - T_m) \qquad (5.34)$$

where T_i is the inlet air-temperature, T_o is the outlet's LHTES air-temperature, and T_m is the mean melting PCM temperature.

The cooling load ratio, Φ, which is released from the centralized LHTES system for two design sizes, is calculated at four different scenarios of inlet air conditions. Two sizes of LHTES system of 650 and 750mm are simulated for four conditions of the inlet air-temperatures, (i.e., 26, 30, 36, and 40℃).

$$\Phi = Q/Q_{max} \qquad (5.35)$$

where Q is the cooling energy released over the discharging period, and Q_{max} is the maximal amount of cooling energy that could be obtained during such period.

As appears from the numerical results of the different size LHTES of Figures 5.20- 5.21, it can be seen that the order of magnitude for the cooling factor lines increase for the entire discharge period when the inlet air conditions are lower than 40℃. Due to the different air flow rate, the predicted cooling factor, ξ, against the cooling load ratio (see Figure 5.20) falls within a narrow band for mean melting point of 21℃. This is due to the fact that the temperature of melted PCM is uniform for long time with evenly releasing cooling energy, promoting by natural convection effect. As expected, the cooling factor increases when the inlet air-temperature is equal to 30℃ with phase change temperature range of 22-24℃. Also, it is found that the average ratio of the cooling factor is equal to 3.5 corresponding to case of entering air-temperature of 26℃ with phase change range of 22-24℃ for the LHTES's size system of 650mm as shown in

Figure 5.21. The straight lines which are obtained from the relation between the cooling factor and the cooling load ratio become closer at averaging cooling load ratio equal to 1.3 for entering air-temperature of 40℃. While entering air-temperature of 30℃, the average ratio reaches 2.0 for the LHTES's size system of 650mm.

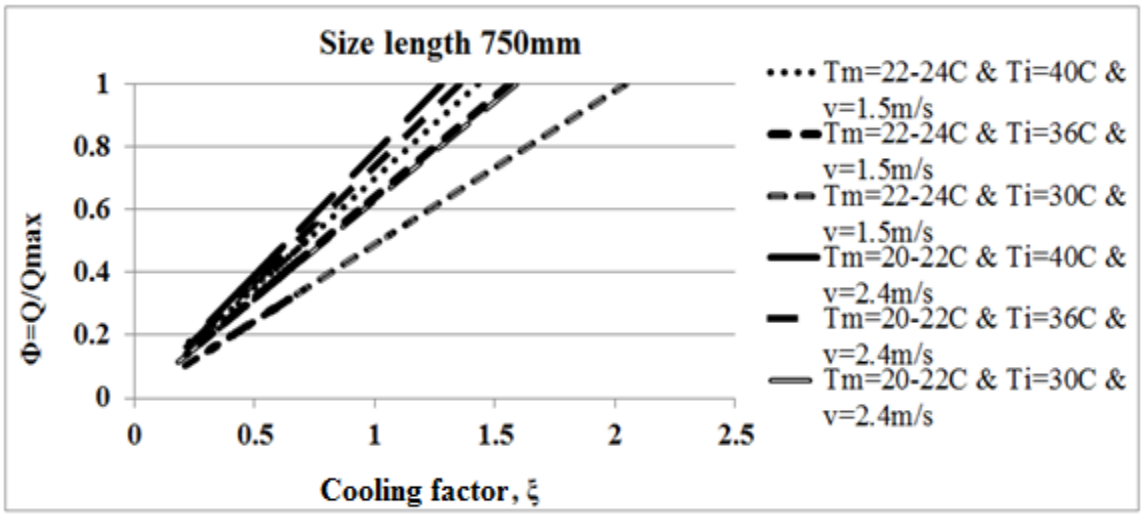

Figure 5.20 Cooling factor versus the rate of the cooling load for the centralized LHTES's length of 750mm

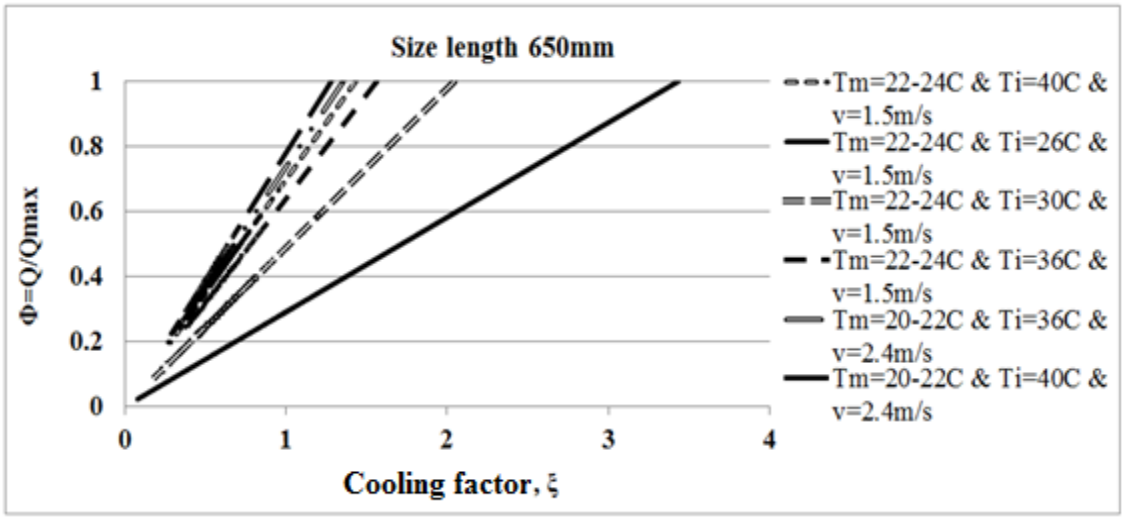

Figure 5.21 Cooling factor versus the rate of the cooling load for the centralized LHTES's length of 650mm

5.5 Summary and conclusion

A transient three-dimensional heat transfer model of a centralized LHTES system is conducted to investigate the effect of influential parameters on its thermal performance. The numerical solution is conducted using the commercial software package, Fluent 12. The centralized LHTES system constitutes of a metal box filled with paraffin RT20 as PCM, enhanced with internal and external fins on its surfaces. The conduction heat transfer flow through the fins is numerically solved in conjunction with the transient conjugate heat transfer problem of PCM. The enthalpy-porosity approach was used to model the convection-diffusion phase change. The developed model is validated by comparing the numerical results with the available experimental data. The numerical model shows a great potential to predict the heat transfer fluid performance of a centralized LHTES system.

Simulations were carried out to study the impact of initial temperature condition on improving the outlet temperature of LHTES system for cooling and heating applications. The convective term considered in this study shows that its effect is significant during the melting stage prompting the melted liquid of PCM to move. Parametric simulations were carried out to investigate the effect of the geometrical parameters on the HTF outlet temperature, heat transfer rate, and melting time. The normalized analysis shows that the temperature difference has an influential impact on the performances of a centralized LHTES system. During the discharging process, the performance of a centralized LHTES system is enhanced when the temperature difference is greater than 10K. Correlations have been developed for the distribution of

melting front and solid fraction as a function of time. These correlations can be used to further optimize the design of cooling or heating systems.

Chapter 6

Assessing Centralized Thermal Energy Storage System Performance

6.1 Introduction

Evidence from a variety of research suggests that the built environment contributes substantially to global energy consumption and to the production of greenhouse gases that impact climate change: buildings use about 40% of the world-wide total annual energy consumption and contribute up to 35% of the Greenhouse Gases (GHG). These facts highlight the importance of targeting building energy use as a way to decrease building energy consumption and GHG emissions simultaneously. The contribution of building energy use to climate change has been acknowledged by the Intergovernmental Panel on Climate Change (IPCC) [108]. The IPCC has prepared documents that assist policy makers to design programs for reducing energy use in buildings.

Dincer et al. [109] applied a feed-forward back-propagation artificial neural network (ANN) algorithm to analyze heat transfer through an annularly finned tube filled with a PCM, concluding that the ANN approach is a promising method for analyzing thermal energy storage systems within a maximum discrepancy of about 5% compared to a numerical solution. Sanchez et. al [110] applied ANN to study the performance of microencapsulation containing a PCM. They investigated the effect of the ratios of paraffin wax to styrene mass, of poly-vinylpyrrolidone to styrene mass, and of water to

styrene mass on micro particles. The average of the particle size was empirically correlated based on the latent heat of microcapsules using a neural network with a single neuron. It was concluded that the developed neural network can predict the latent heat with less than 7% error and the average particle size with less than 20% error. To the authors' knowledge, no effort has been made to investigate the performance of a LHTES system integrated with a building under realistic conditions.

The outcome of an extensive CFD simulation to study the long term performance of a centralized LHTES system is reported. A validated CFD simulation tool is integrated with a building's mechanical ventilation system. Paraffin RT20 was used as a PCM and fins are used to enhance its performance.

To reduce the computational time, ANN was used to relate the relationships between the LHTES inputs and the output parameters. To develop the ANN, extensive CFD simulations were carried out to identify all the influential parameters, which include phase change temperature range, airflow rate, the geometrical configuration of a LHTES system, fin size, and the unit's length. Further CFD simulations were carried out to develop a sufficient database for the proper training and testing of the ANN.

6.2 Ventilation system using the LHTES system

The LHTES system is integrated with a building mechanical ventilation system to provide the required indoor thermal conditions using free cooling. The control strategy for the ventilated room is established to ensure that the internal air room temperature does not exceed 25℃. To analyze the LHTES system's thermal performance, the following operational strategy was used:

1- Charging period: from midnight until 8:00AM, higher air flow rates are used to solidify the PCM since the ambient air temperature is relatively lower than the average mean melting point temperature of the PCM (i.e., 24℃), as shown in Figure 6.1 (a).

2- Discharging period: Relatively low air flow rates are allowed to pass over a centralized LHTES system during the discharge period, normally from 8:00AM until midnight, seeking to dampen the fluctuation of inlet air temperatures from the storage system outlet to within the comfort temperature range, as shown in Figure 6.1 (b).

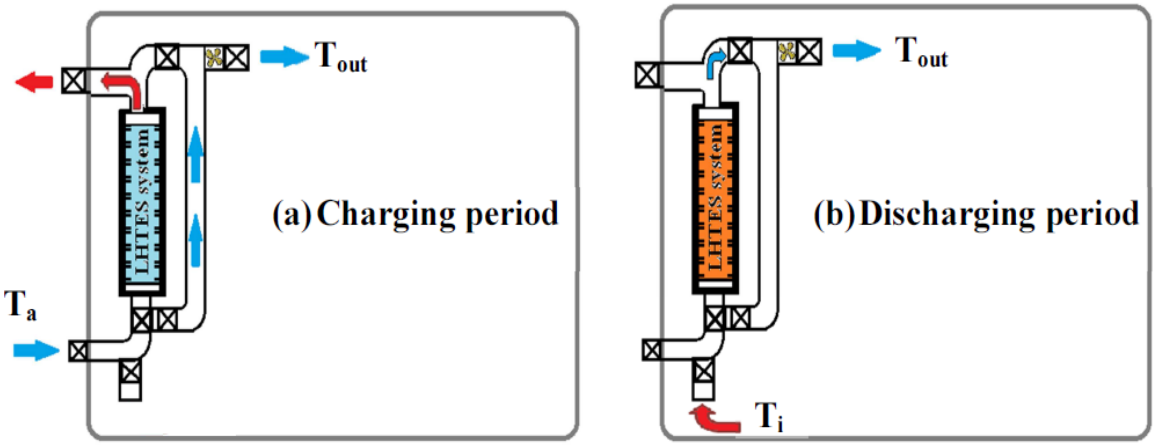

Figure 6.1 Installation of a LHTES in two ventilation control modes; (a) charging mode, (b) discharging mode

The National Climate Data and Information Archive in Canada weather data for Montreal was used as an input to investigate the system performance [111], refer to UDF in Appendix (C). By assuming that the inner surfaces of the duct are smooth and the air is an ideal gas, the air properties were obtained at an approximate average surface temperature of 293.15K and at atmospheric pressure of 1atm. The air-flow movement

through the LHTES system is illustrated in Figure 6.2. The average velocity of air is considered to be 1.5 m/s, equivalent to the volume airflow rate of 0.0271m^3/s. The ventilation load required to regulate the indoor air temperature is estimated for two cases: 1) with a conventional ventilation system, and 2) applying the LHTES system to assess its potential to reduce peak-hour electricity demand to off-peak period.

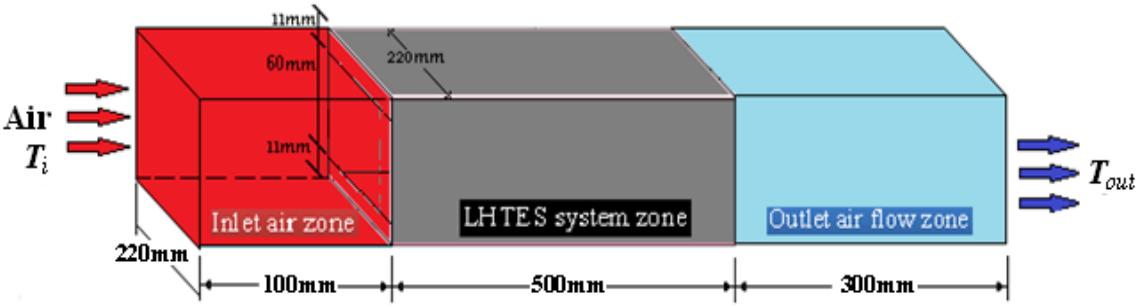

Figure 6.2 Channel of air flow movement through the LHTES system

Eq. (6.1) was used to calculate the energy release during discharge. The energy calculation was performed when the LHTES system's outlet air temperature was lower than that of the inlet ambient air temperature. Figure 6.3 shows the hourly inlet air temperature, the calculated LHTES system's outlet air temperatures, and the cooling load. The inlet air velocity of 1.5m/s and the phase change temperature range of 4K for an average melting point of 294.15K were assumed. The inlet air temperature increased during the daytime, allowing the PCM to melt. However, in most cases the PCM was not completely solidified during the night-time charging period.

$$Q_{cooling} = \rho c \dot{V} \left(T_{Air} - T_{out,LHTES} \right) \quad (6.1)$$

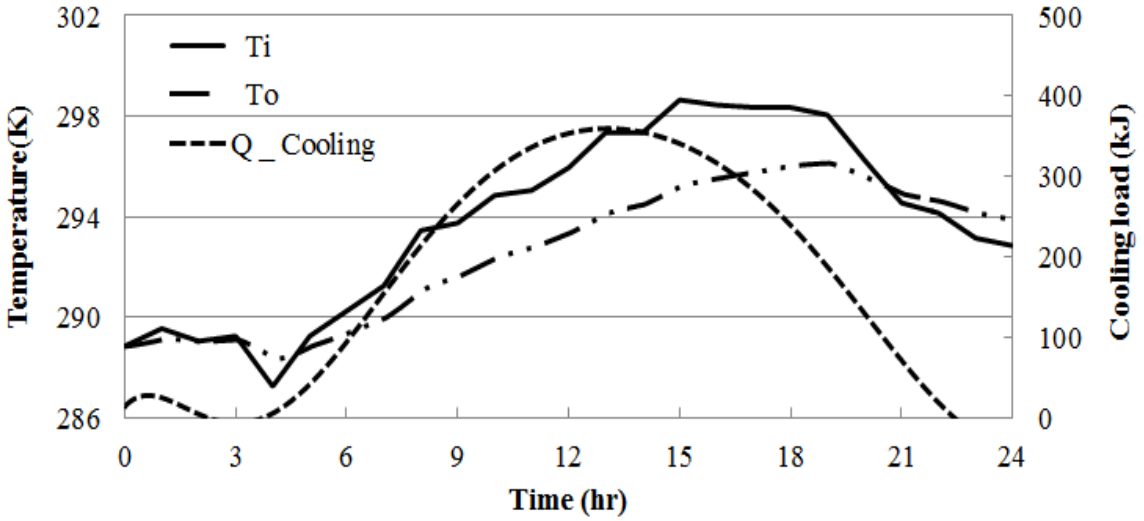

Figure 6.3 Variations of the outdoor ambient and calculated outlet air temperatures along with the PCM energy released for the hourly temperature changes on July 1st

1- Conventional ventilation load system: The ventilation load was determined when the outdoor air was directly supplied to the room, using Eq. (6.2). Calculations were performed to ensure that the indoor air temperature did not exceed the target temperature of 24℃.

$$Q_{C,Air} = \rho c \dot{V} (T_{Air} - T_C) \quad (6.2)$$

2- Ventilation load with LHTES system: To investigate the potential of integrating the LHTES system, the ventilation load was estimated based on two scenarios: 1) when both the ambient outdoor and the LHTES system's outlet air temperatures were higher than the set-point temperature of 24℃, and thus the cooling load was equal to zero; and 2) when the LHTES system's outlet air temperature was equal to or less than the outdoor air temperature. Eq. (6.3) was used to calculate the controlled ventilation load supplied by the LHTES system.

$$Q_{C,LHTES} = \rho c \dot{V} \left(T_{out,LHTES} - T_C\right) \quad (6.3)$$

In chapter 5, the development and validation of a CFD model to characterize the performance of a PCM was reported by A. El-Sawi et al. [112]. Here, the validated CFD model is used to perform hourly simulation using 1st June Montreal weather data to investigate the potential of using LHTES for free cooling. Paraffin, of RT20, was used as a storage media (the PCM) with latent heat of fusion of 172kJ/kg for a phase change range of 4K with an average melting point of 297.15K. Figure 6.4 shows the calculated hourly LHTES system's outlet air temperature associated with the PCM's energy release. When the centralized LHTES system is applied, the results show the inlet air temperature, which is extracted from weather data, can be stabilized. The dashed area represents the amount of cooling load that was removed using the control strategy by switching to the LHTES system. This results in a reduction of 63% in the total required cooling load for June 1st.

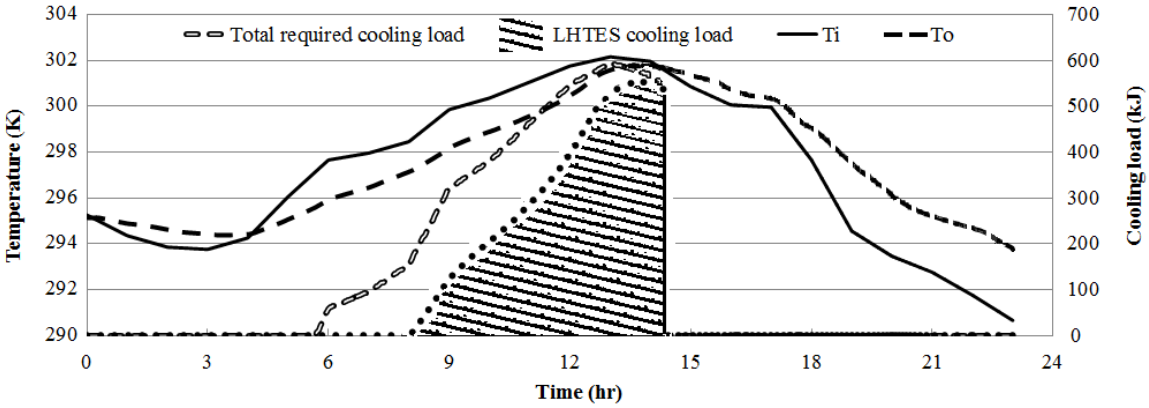

Figure 6.4 Hourly variations of the measured ambient air and the LHTES system's outlet air-temperatures for June 1st and the cooling load of the LHTES

6.3 Development of an artificial neural network (ANN) for predicting the long-term performance of a LHTES system

Predicting the long-term performance of a centralized LHTES system using CFD simulation is a very time consuming process. There are different methods to identify the relation between the independent variable and the dependent variables. Since the relation between the outdoor air temperature and the thermal performance of the centralized LHTES system is highly non-linear, the Artificial Neural Networks (ANNs) method can be an efficient way to find that relation [113, 114]. ANNs are known as an effective method for approximating non-linear model function. To predict the thermal performance over a wide range of weather data, an ANN approach was developed to extrapolate the LHTES's outlet air temperature, which is calculated by CFD.

Extensive CFD simulations were carried out to identify all the influential parameters for the development of the ANN.

6.3.1 Effect of phase change temperature range on the ventilation load

The effect of the range of phase change temperature on the thermal performance of a LHTES was investigated. The reduction in cooling load was estimated using Eq. (6.4).

$$\text{Rate of cooling load reduction} = \frac{\sum Q_{cooling}}{\sum Q_{C,Air}} \qquad (6.4)$$

Three values of phase change temperature range, 4, 8, and 12K, were used to assess their effect on reducing the cooling load [46]. The inlet air-temperature was varied based on the hourly weather data of Montreal, Canada to simulate changes of LHTES system's outlet air-temperature for July 1st, 2011, as shown in Figure 6.5. The latent heat of the

PCM remained constant for all three cases, at 172kJ/kg. Table 6.1 shows three different ranges of phase change temperatures.

Table 6.1 Effective specific heats used for three ranges of phase change temperatures [46]

Range Phase Change	4K	8K	12K
T_{PCM}(K)	c_{eff}(kJ/kg.K)	c_{eff}(kJ/kg.K)	c_{eff}(kJ/kg.K)
283.15	0.5	1.1	2.1
285.15	21.3	14.4	29.7
294.15	200	118	62.2
295.15	260	128	60.8
297.15	2.13	3.6	4.1

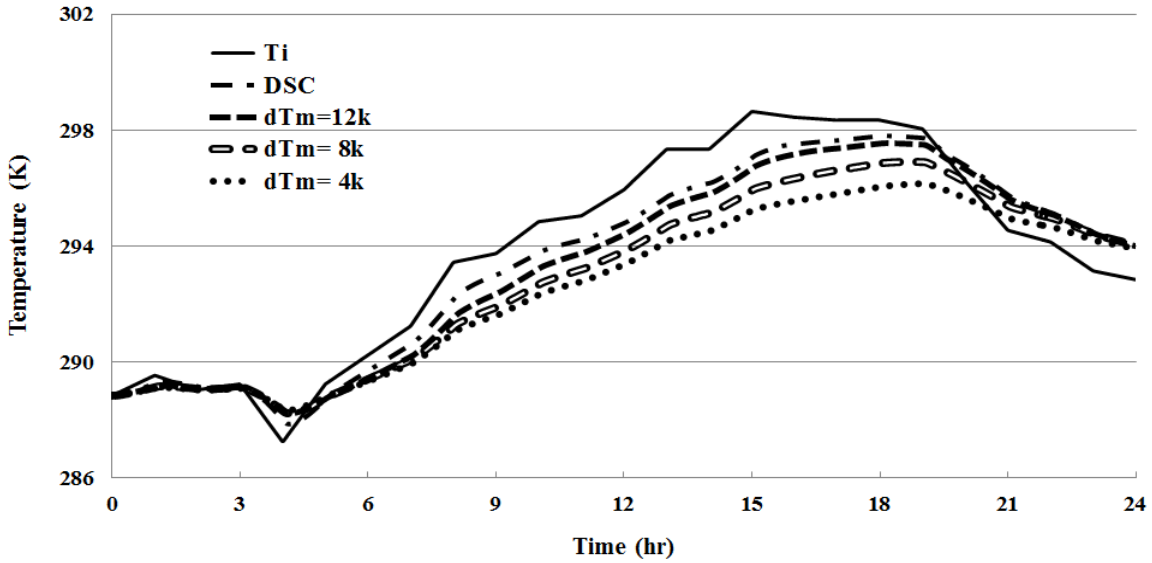

Figure 6.5 Simulation results of a LHTES system's outlet air temperatures at different ranges of phase change temperature for the selected day for July 1st, 2011 in Montreal

To meet the thermal comfort requirement the indoor air temperature is set at 20℃. The total required cooling load, $\sum Q_{C,Air}$, was numerically determined and found to be 5327kJ when the inlet air temperature was higher than the set point.

The summations of $Q_{C,Air}$ and $Q_{cooling}$ over the simulation time are obtained using the trapezoidal rule. Table 6.2 presents the controlled cooling load, $\sum Q_{C,LHTES}$, and the cooling load of the LHTES system, $\sum Q_{cooling}$.

Table 6.2 Daily cooling and controlled loads for a LHTES system with (a conventional load) (DSC stands for differential scanning calorimeter)

Phase change temperature range (K)	$\sum Q_{cooling}$ (kJ)	$\sum Q_{C,LHTES}$ (kJ)
DSC	1192	3574
4	2574	2162
8	2050	2710
12	1515	3264

It was found that the potential of reducing the cooling ventilation load is higher, 48%, for the phase change temperature range of 4K followed by 38% for 8K, and 28% for 12K, while for DSC it is about 23%. This is because the inlet air temperature is relatively low in the early morning with a modest increase to midday of 296K, where the phase change occurs in the range of 293.15-297.15K. These observations leads us to assume that the PCMs with phase change temperature of 12K, and 8K do not have the required time to be completely melted with only a small fluctuation of the ambient air temperature. Thus, the melting process is only partially performed leading to a release of smaller amount of stored cold energy. Here, the PCM with a phase change temperature of 4K is allowed to completely melt and thus release an appreciable amount of stored cool energy.

The cooling load was calculated when both the LHTES's outlet and the inlet air temperatures were higher than the set point and the LHTES's outlet temperature was lower than the inlet air temperatures. The potential cooling load, $Q_{C,LHTES}$, for a typical

day is calculated hourly and reported in Table 6.2. After calculating the summation of the total hourly values of $Q_{C,Air}$ and $Q_{C,LHTES}$, the reduction of ventilation load is verified at 61% of the total required ventilation for the effective heat capacity in the phase change range of 12K, and 67% for the DSC approximation function of the effective specific heat. The daily energy demand reduction for the phase change ranges of 8K and 4K are 51% and 41%, respectively. In addition, the amount of cooling load reduction calculated for the DSC measurements at 0.1 K/min is about the same as that for the phase change range of 12K.

6.3.2 Effect of the geometrical configuration of a centralized LHTES

6.3.2.1 Fin size

Figure 6.6 shows the LHTES system's outlet air temperature calculated for fin thicknesses of 0.6, 1.1, 1.5, and 2mm. The PCM is selected to be paraffin, with melting and solidification points of 297.15K and 294.15K, respectively. It was found that the fin size does not have a significant effect on enhancing the heat exchange between the heat transfer fluid (HTF) and the PCM. Nevertheless, the storage system reached its thermally optimal performance when the fin thickness was 0.6mm. For the first day, the liquid fraction approached 0.8 and 0.9 for fin sizes of 1.5mm and 2.0mm, respectively. For the fin size of 1.1mm, the liquid fraction reached 0.7 at 19hrs, as depicted in Figure 6.7. The heat exchange between the PCM and the HTF was faster in case of the 2.0mm fin size compared to the other cases. Hence, after 19hrs of discharging time, the released stored cooling energy was no longer available. Figure 6.8 shows the variations of hourly cooling loads with different fin sizes. The summation of the cooling load, $\sum Q_{C,LHTES}$, is

determined based on a control strategy that allows the inlet air stream to pass through the LHTES system when its temperature is equal to or over the set point temperature, 297.15K. However, an additional condition is required and is satisfied when the LHTES system's outlet air temperature is higher than the selected control temperature. The results revealed that the smallest fin size evaluated provides the highest amount of cooling load.

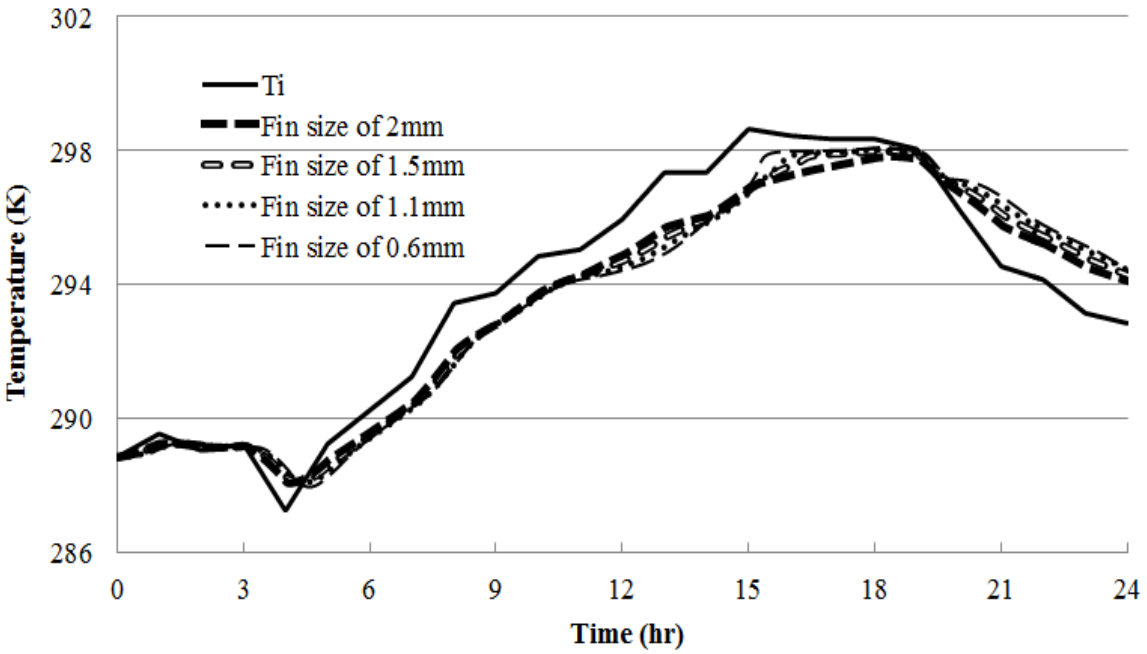

Figure 6.6 Hourly calculated outlet air temperatures of LHTES system for July 1st in Montreal, Canada.

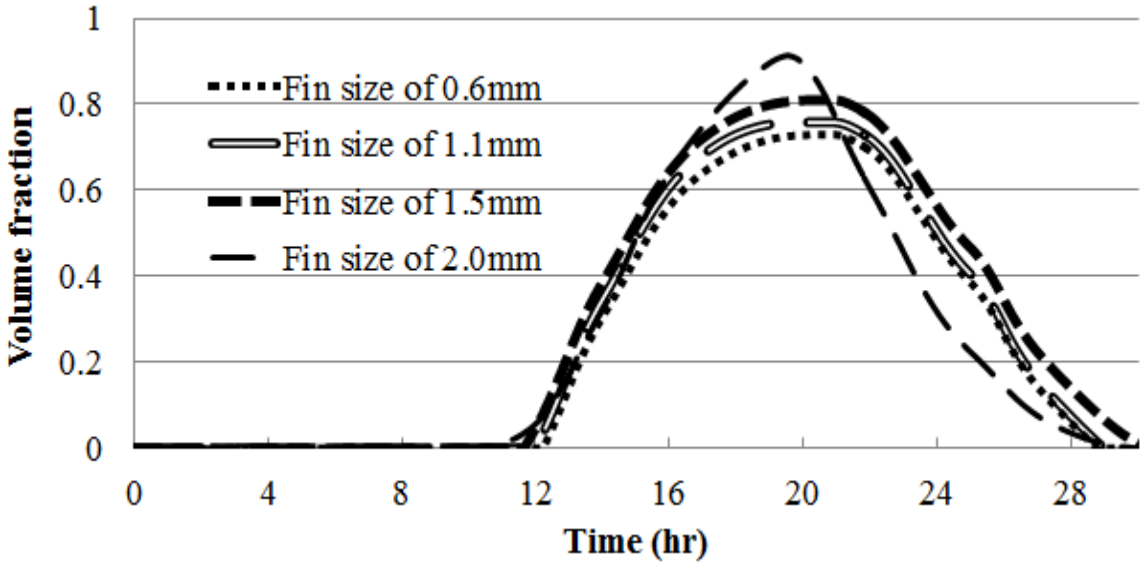

Figure 6.7 Numerically-calculated volume fraction of PCM for different fin sizes

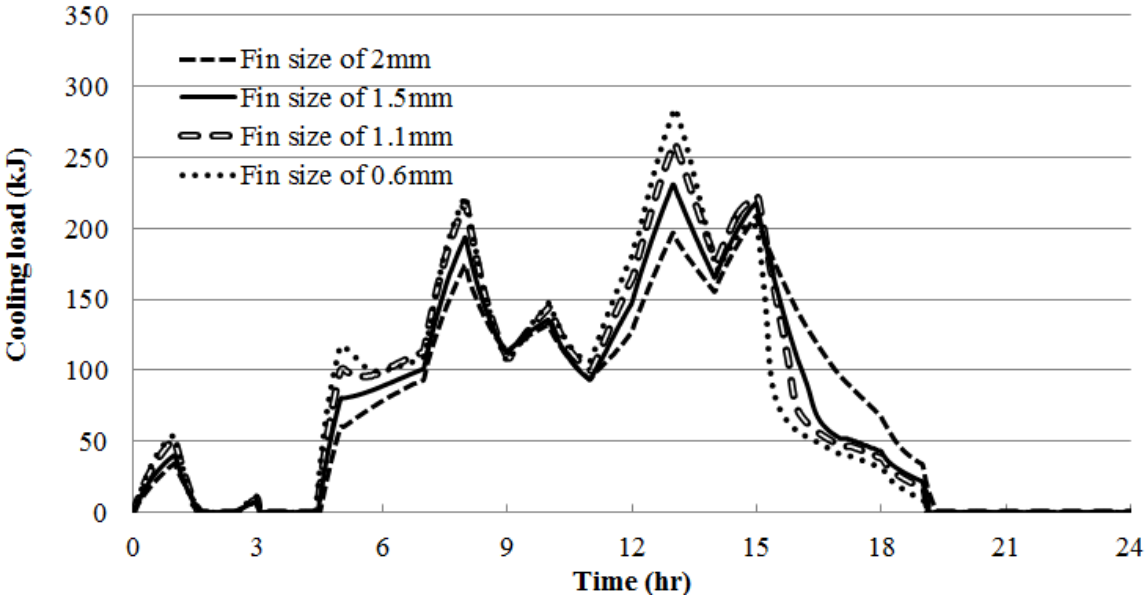

Figure 6.8 Hourly calculated cooling load of LHTES system as a function of time for different fin sizes, for July 1st in Montreal

6.3.2.2 LHTES system length

Figure 6.9 shows the calculated LHTES's outlet air temperature as a function of time for different LHTES system lengths. The length of the LHTES system was changed

from 500 to 650, and to 750mm associated with the change in the inlet air flow rate conditions. Accordingly, the mass of RT20 paraffin, which has a phase change temperature range of 294.15-297.15K, is increased from 3.6kg for the LHTES system length of 500mm, to 4.68kg and 5.4kg for the LHTES system lengths of 650mm and 750mm, respectively. For each selected length, two different velocities of inlet air conditions were considered, 1.5m/s and 2.4m/s.

Figure 6.10 shows that the amount of stored energy increases as the LHTES system length increases. However, the thermal performance does not show any improvement with the increase of the air flow rate. This figure shows that in the case of a 750mm length size and inlet air flows of 1.5m/s and 2.4m/s, the system has a significant potential to stabilize the fluctuation of the inlet air temperature, followed by the 650mm length size with 1.5m/s. There is a significant improvement (15%) on the reduction of the cooling load when the length of the LHTES system is increased from 500mm to 650mm. However, the ventilation airflow rate does not show a significant effect on reducing the cooling load when the entering air speed is higher than 1.5m/s. This result is consistent with experimental work [74]. The result shows a marginal improvement on reducing the cooling load for the longest size compared to the LHTES system length of 650mm.

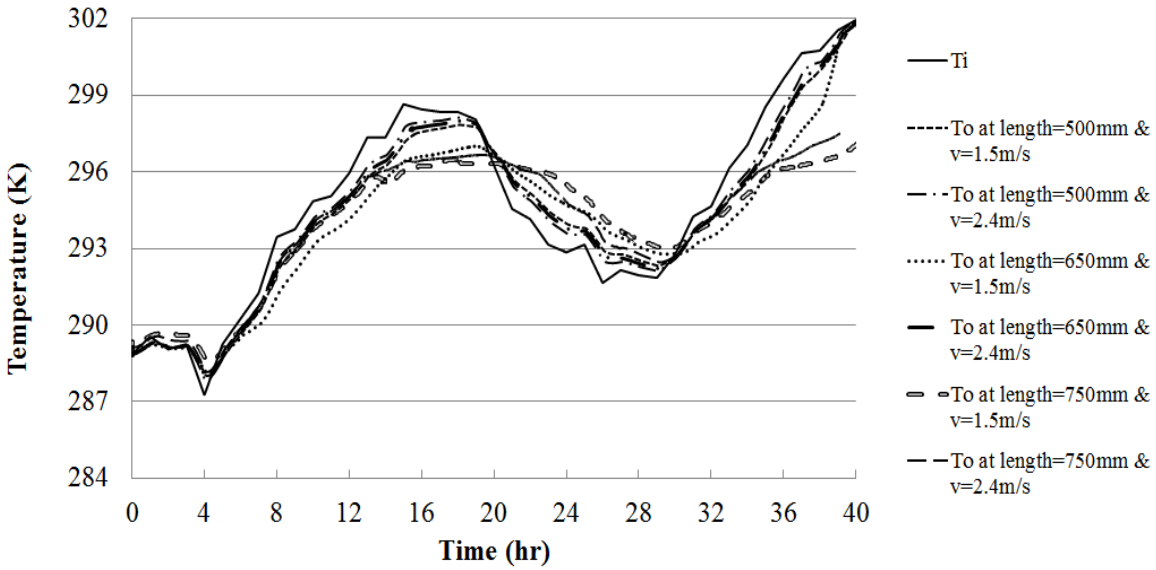

Figure 6.9 Hourly calculated LHTES system's outlet air temperature for the typical first two days of a week in July in Montreal for different LHTES system lengths

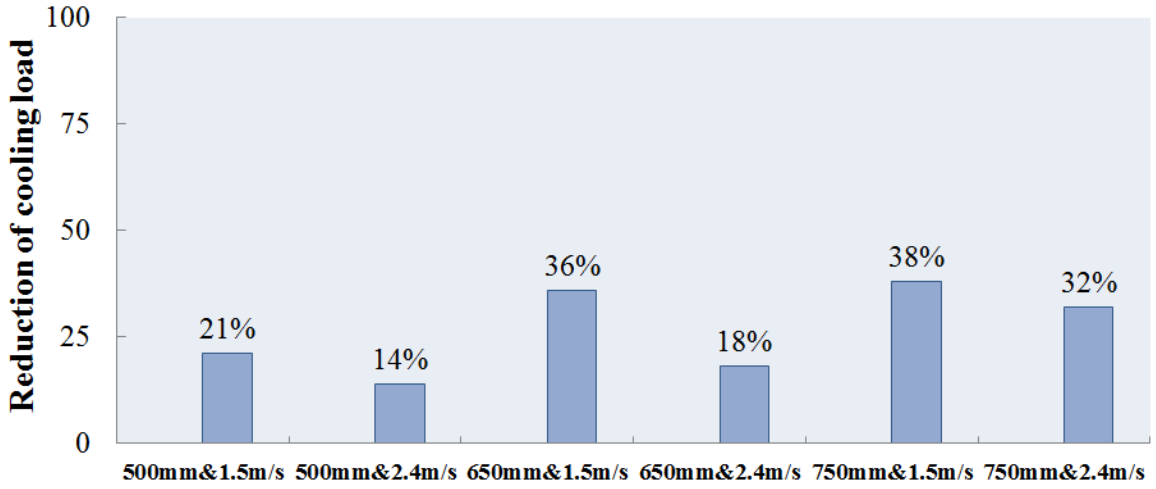

Figure 6.10 Reduction in the cooling load for different parameters of the LHTES system performance design

The remaining cases appear to have a similar trend of the variation with relatively small differences. This can be interpreted from Figure 6.11, where the variation of volume fraction with time for the selected cases is plotted. In the case of the 500mm length size with 1.5m/s, the PCM starts melting after about 10hr (10:00AM) and it is

completely melted at hour 20 (8:00PM), resulting in a complete release of the stored cooling energy. As a result, the LHTES's outlet air temperature is sharply increased. However, the melting rate is relatively faster in the case with higher air speed. This phenomenon can be observed with the 650mm length when the inlet air speed is 2.4m/s; the melting rate is higher, thus increasing the LHTES system's outlet air temperature. On the other hand, when the inlet air speed is 1.5m/s, the LHTES system's outlet air temperature becomes more stabilized, resulting in a higher thermal performance for the LHTES system. The longest size shows the best thermal performance on the first day, regardless of the inlet air speed.

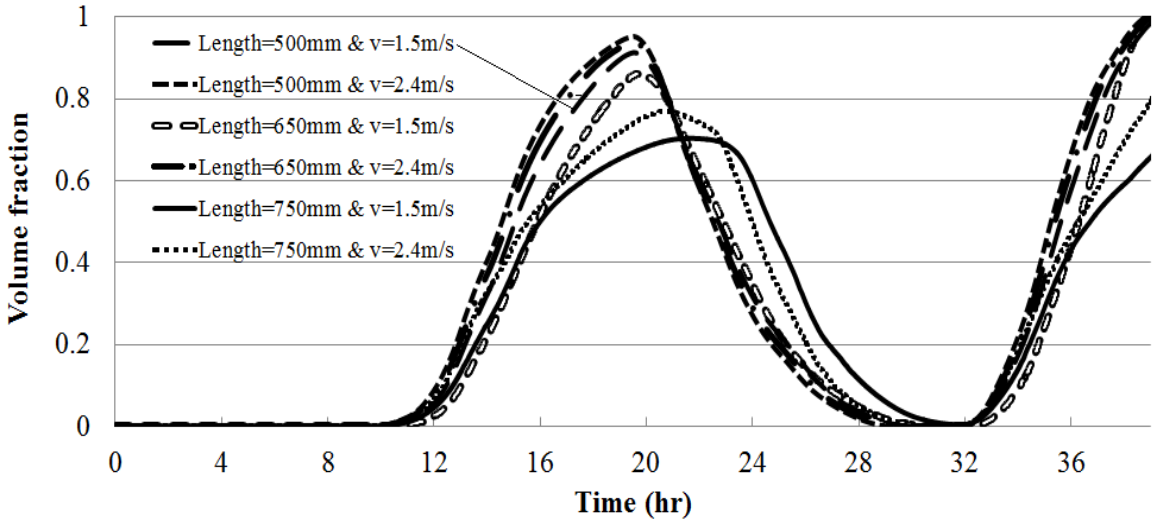

Figure 6.11 Liquid volume fraction calculations of the typical first two days of a week in July in Montreal for different LHTES system lengths

6.3.3 ANN development

A generalized GMDH-type (group method of data handling) ANN is implemented to integrate with the obtained numerical results. A generalization of the neutral network improved the connectivity configuration to provide an optimal network

in which hidden layers and numbers of neurons were more effective to describe the dependent variable of heat transfer phase change process in a polynomial expression. A genetic algorithm is involved in a GMDH-type ANN to effectively determine the values of the quadratic coefficients for a second-order transformation of the inputs. This method provides the flexibility to manage neutral networks with different lengths, sizes and capabilities, as it allows the information to be manipulated by changing building blocks. As a result, both small and large numbers of input variables can be effectively modeled.

The classical GMDH algorithm can be described as a group of neurons where each pairs of neurons is tied at each layer using a quadratic polynomial, so that a new generation of neurons will be produced for the next layer. Thus, the output will be a consequence of this reproduction process. Finally, the target is to reach an approximate function value, $\bar{f}$ of output close to the actual one, f for a given input vector, $X = (x_1, x_2, x_3, \ldots, x_n)$. Furthermore, the square difference between the actual and predicted functions should be minimized to ensure a reasonable accuracy. Farlow presented a polynomial form to relate the input to the output [115]:

$$y = a_0 + \sum_{i=1}^{n} a_i x_i + \sum_{i,j=1}^{n} a_{ij} x_i x_j + \sum_{i,j,k=1}^{n} a_{ijk} x_i x_j x_k + \cdots \quad (6.5)$$

This formula can be simplified for two input variables into the quadratic polynomial form which is most often used to predict the output, $\bar{f}$ as follows [116]

$$\bar{f} = G(x_i, x_j) = a_0 + a_1 x_i + a_2 x_j + a_3 x_i x_j + a_4 x_i^2 + a_5 x_j^2 \quad (6.6)$$

The evolved hidden two layers of a typical GMDH-type neural network structure (G4 and G5) are illustrated in Figure 6.12, and the coefficients a_i in Eq. (6.6) can be determined using regression techniques so that the output $\bar{f}$ is calculated for each pair of

x_i, x_j as input variables. A tree of polynomials is constructed where the coefficients are determined using the quadratic form in a least-square sense. The general structure of a GMDH-type neural network is evolved in which neurons are connected to each other for all layers. Thus, an optimal fit of the output in the entire set of input and output data is achieved for each connected pair of input-output data through quadratic function G.

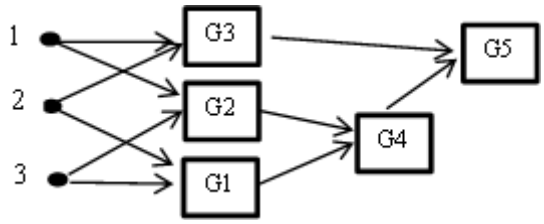

Figure 6.12 A typical feed-forward GMDH-type network

Numerical results for the melting processes were obtained at different inlet air-temperatures. The output parameter was the outlet temperature from the LHTES system and the three input parameters are: heat transfer fluid (HTF), inlet temperature, and volume fraction. Proper training enables an ANN to provide a fast and accurate approximation of the LHTES outlet temperature for a wide range of inlet conditions (i.e., air temperature and flow rate). Thus, a large number of CFD simulations are needed for proper training of the ANN. The simulations must cover a wide range of all influential parameters, and cover the whole search space.

Figure 6.13 compares the numerical results and ANN prediction and indicates a good agreement between them so that ANN function can be used later to predict the LHTES system's outlet air temperature. Table 6.3 illustrates the data used for training a feed forward GMDH-type network. The data is selected based on CFD simulations for

the first days of each week for the month of July in Montreal, Canada. Thus, the LHTES system's outlet air temperature for the entire month can be predicted utilizing a feed-forward GMDH-type network. Table 6.4 provides the calculated coefficients that are used for the second-order polynomial equation after training the ANN for the month of July, obtained from Table 6.4. G1, G2,…, Gn represent a general connection between the input and output variables, as expressed in Eq. (6.6). For instance, G1 is a quadratic function to connect the inlet ambient air temperature and the volume fraction, with an optimal set of appropriate coefficients, a_0, a_1,…,a_n which are given in Table 6.4. Similarly, G2 represents a connection between the computational time and the volume fraction through a quadratic polynomial equation. G3 is utilized to connect the computational time and the inlet ambient air temperature. Hence, first a hidden layer is built and then the second layer is established by connecting the predictive functions, G1 and G2 so that the quadratic polynomial equation G4 is constructed using the quadratic form provided in Eq. (6.6) for which the coefficients are obtained in a least-squares sense. Finally, the outlet prediction function, G5, is constructed by integrating G3 and G4 with the associated coefficients obtained for G5.

Figure 6.14 shows the thermal performance of the centralized LHTES system that represents the response of the LHTES system's outlet to the inlet air temperatures using Eq. (6.6) and the coefficients from Table 6.4.

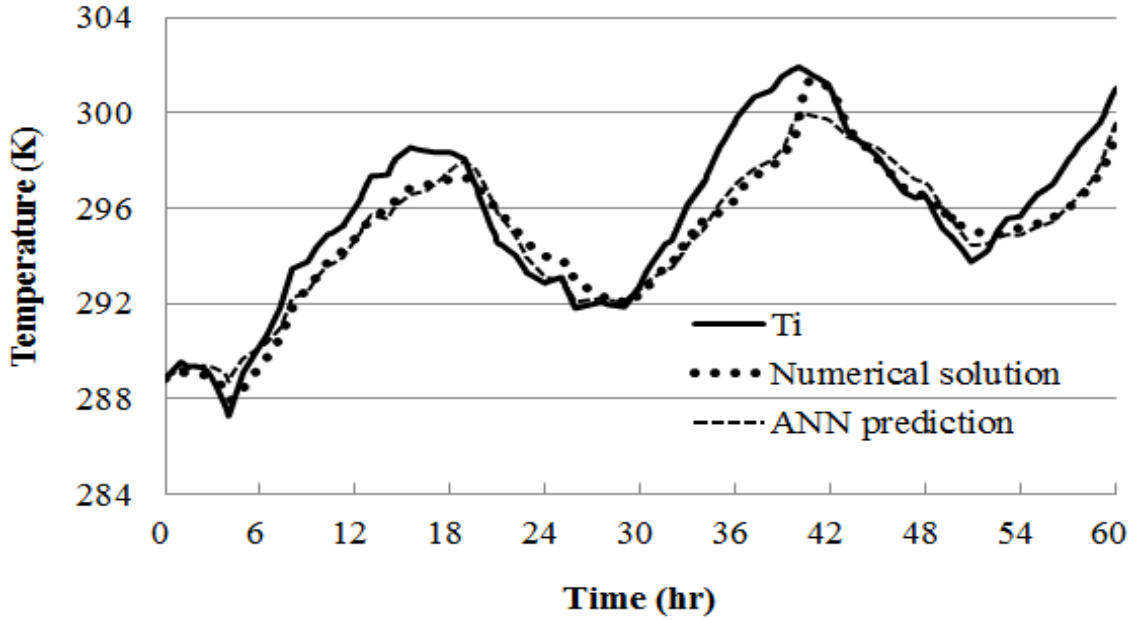

Figure 6.13 Comparison of the numerical calculation and the ANN's prediction for the single LHTES system's outlet air temperature

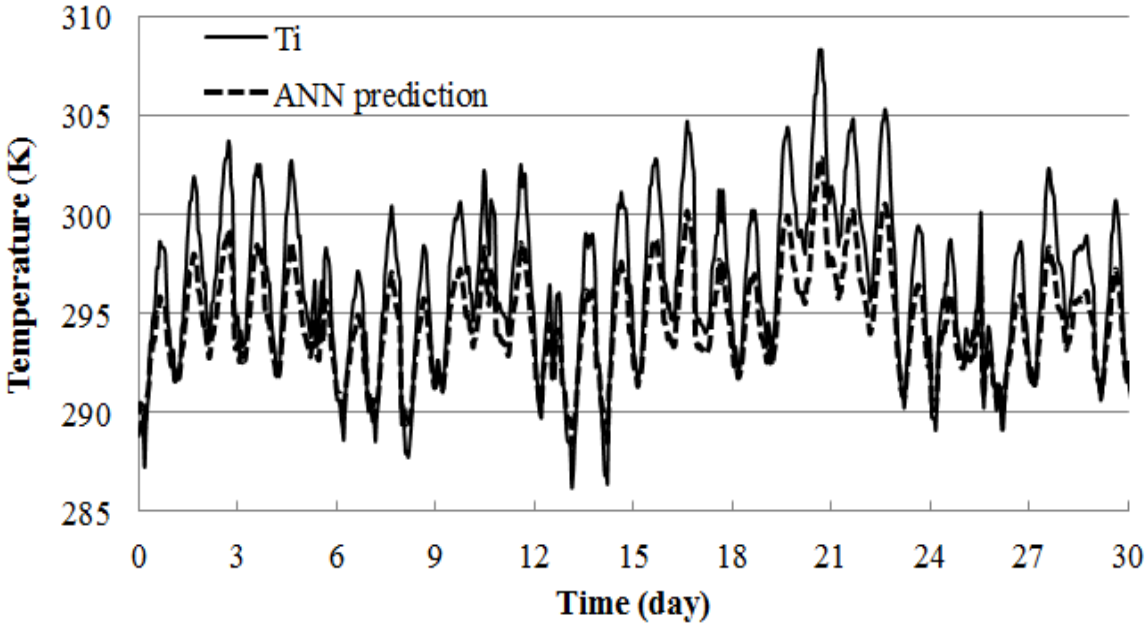

Figure 6.14 The ANN's prediction for the single LHTES system's outlet air temperature for the entire month of July in Montreal

Table 6.3 Input parameters and the calculated output versus the ANN output prediction

Iteration No	Iteration start Time (hr:min)	Ambient air temperature (K)	Volume fraction	Outlet air Temperature (K), Numerical result	Outlet air Temperature (K), Prediction of ANN	ΔT(K)
1	0:00	288.85	0.00	288.85	290.09	1.24
2	0:52	289.21	0.00	288.91	290.29	1.38
3	0:82	289.42	0.00	289.02	290.41	1.39
4	2:62	289.17	0.00	288.98	290.26	1.28
5	3:72	287.81	0.00	288.47	289.51	1.04
6	3:99	287.28	0.00	288.16	289.21	1.05
7	4:92	289.09	0.00	288.42	290.22	1.8
8	6:09	290.34	0.00	289.45	290.91	1.46
9	8:09	293.48	0.00	291.90	292.71	0.81
10	10:50	294.94	0.00	293.83	293.58	0.25
11	13:10	297.35	0.12	295.62	295.24	0.38
12	14:00	297.40	0.23	295.94	295.54	0.4
13	14:50	298.05	0.30	296.29	296.07	0.22
14	16:50	298.40	0.59	296.97	297.14	0.17
15	16:70	298.38	0.63	297.01	297.23	0.22
16	17:60	298.35	0.75	297.15	297.64	0.49
17	18:30	298.27	0.84	297.27	297.87	0.6
18	19:50	297.09	0.93	297.08	297.54	0.46
19	20:90	294.78	0.82	295.98	295.98	0
20	20:90	294.77	0.82	295.98	295.98	0
21	20:90	294.67	0.81	295.93	295.89	0.04
22	20:90	294.67	0.81	295.93	295.89	0.04
23	20:90	294.67	0.81	295.93	295.89	0.04
24	21:00	294.54	0.79	295.84	295.77	0.07
25	21:30	294.43	0.74	295.69	295.58	0.11
26	22:20	293.98	0.57	295.10	294.84	0.26
27	22:80	293.31	0.44	294.55	294.06	0.49
28	25:00	293.10	0.11	293.83	292.82	1.01
29	25:90	291.85	0.05	292.99	291.92	1.07
30	27:60	292.04	0.00	292.30	291.87	0.43
31	28:00	291.95	0.00	292.19	291.81	0.38
32	28:10	291.94	0.00	292.18	291.81	0.37
33	29:00	291.88	0.00	292.05	291.77	0.28
34	33:70	296.79	0.06	295.28	294.80	0.48
35	34:00	297.05	0.10	295.45	295.01	0.44
36	35:00	298.53	0.18	295.81	296.03	0.22
37	36:10	299.79	0.28	296.58	296.94	0.36

38	37:20	300.67	0.42	297.32	297.71	0.39
39	38:40	301.03	0.58	297.81	298.34	0.53
40	39:10	301.59	0.67	298.22	298.89	0.67

Table 6.4 Coefficients of the quadratic form used in Eq. (6.6)

	a_0	a_1	a_2	a_3	a_4	a_5
G1	-2.01	1.41	49.30	-0.001	1.46	-0.15
G2	292.82	-0.008	8.6	0.001	-2.6	0.004
G3	0.008	-0.028	1.28	-0.0001	-0.001	0.0001
G4	-0.02	3.23	-2.23	0.0170	0.0250	-0.074
G5	0.0030	0.49	0.492	-0.10	-0.11	0.220

6.4 Summary and conclusion

A validated transient 3-D numerical model of centralized LHTES system is used to solve the conjugate phase change heat transfer and fluid flow problem using a CFD commercial package, Fluent-12. The centralized LHTES system is filled with paraffin RT20 as a PCM and is enhanced with fins embedded at the top and bottom of its surfaces. The outlet air stream, a HTF (Heat Transfer Fluid), is allowed to pass over the top and bottom of the LHTES system. The centralized LHTES system is integrated into a mechanical ventilation system. The thermal performance of the LHTES system is assessed using hourly inlet air data obtained from the National Climate Data and Information Archive, Canada for summer months. The effect of phase change temperature range, HTF flow rate, of the geometrical configuration of a LHTES system, unit fin size and length on the output temperatures of the HTF is quantified.

The time-step of the simulation model is one second, making long-term analysis computationally prohibitive. The performance of the LHTES system is simulated for the

first days of each week throughout the month. The obtained numerical results are used to train an ANN for estimating the long-term performance of the system. Using the ANN, the LHTES's outlet air-temperatures are estimated over the entire summer (defined as 1 June to 31 August). The predicted function of an ANN is evaluated by predicting the output temperatures of the LHTES for the simulated period of selected days throughout the summer months. The results indicate that there is a good agreement between the ANN's prediction and the numerical results. Through the parametric study, the effects of various significant influencing factors on the system performance, including phase change temperature range, airflow rate, and geometrical configuration of LHTES system, fin size, and length of unit were studied. The numerical results show that the performance of a LHTES system is not significantly affected when the fin thickness size is reduced from 2 to 0.6mm. The effect of the range of phase change temperature on the thermal performance of a LHTES system is investigated by examining several values of the effective specific heat capacities; mainly for 4K, 8K, 12K, and DSC. The highest reduction of the total required ventilation is attained with a higher range of temperature phase change, 12K. The centralized LHTES system contributes to reducing the cooling load from 21% to 36% when the length of the centralized LHTES system is increased from 500-650mm at a flow rate of 1.5m/s.

Chapter 7

Integrating a 3-D Model of the Centralized LHTES System into Buildings using TRNSYS

7.1 Introduction

TRNSYS is a dynamic simulation software for building energy calculations, developed by the Solar Energy Laboratory of the University of Wisconsin-Madison. The building model is described as a Type 56 and its visual interface given as (TRNBuild). The source codes of the modelling types were written in FORTRAN. The interface (TRNBuild) is used to model the building envelope, internal gains, ventilation, and air conditioning system. Another interface, called Studio, is used for performing the simulation. The latter interface enables the user to make a link with the building file and with the local weather file. Generally, the basic idea of TRNSYS is that systems are modeled as groups of components connected to each other according to the user's specifications.

First, a dynamic model of a mono-zone building in TrnStudio simulation is established. Next, the ventilation modes with the centralized LHTES system are integrated into the building simulation model.

7.2 Integrating the centralized LHTES system into a building

7.2.1 The building model description

The thermal building response is simulated for a single-zone model used TRNSYS. The model is an apartment with dimensions of 11.44m×5.69m×2.76m. Each wall of the apartment is divided into several layers of materials, which form a composite

wall (more details are provided in Appendix (A)). The floor area is 11.44m ×5.69m. The exterior walls, with a façade of 5.69m×2.76m, are facing south and north. On the south side, there is one door and one window with surface areas of 1.98 and 2.07m^2, respectively, and one door and two windows of 2.07 and 1.41m^2 (2x), respectively, are on the north side. Since there are no windows on the east-west sides of the apartment, two adjacent walls are considered in the building model.

The thermal building response is investigated for free cooling using a mechanical ventilation system with the centralized LHTES system. Air is used as a heat transfer fluid (HTF) for the LHTES system. A ventilation system delivers fresh air to cool down the storage unit, normally during the night-time to early morning, thereby solidifying the PCM. This process is called the charging period. Thereafter, during the discharging period, the hot air from the internal heating loads is mixed with a fraction of fresh air and then directed to pass over the centralized LHTES system, resulting in a release of the accumulation of stored cooling energy due to the phase change of the PCM, thereby stabilizing the fluctuation of the indoor air-temperature.

7.2.2 Indoor temperatures

To analyze the performance of the storage system for one full day, the operational strategy should be followed along with the associated assumptions:

1. Relatively low air flow rates are allowed to pass over a canalized LHTES system during the discharge period, normally from 6:00AM in the early morning until 19:00PM, seeking to flatten the fluctuation of inlet air temperatures from the storage system outlet to within the comfort temperature range. To this end, a fraction of fresh air is mixed with

the return air stream from the re-circulating air inside the building to be delivered into the centralized LHTES system through a ventilation system duct. The mixed air is cooled down by the centralized LHTES system before being supplied to the building. However, if the outlet air-temperature from the centralized LHTES system is higher than the ambient air temperature, fresh air is directed to the building without passing it into the centralized LHTES system.

The following steps are performed in TRNSYS:

- The air change function is carried out as shown in Figure 7.1. Type 14h is scheduled to allow an air change per hour (ACH) of 5 to flow into the building during the period of 19:00PM -6:00AM and then only a lower flow of 2 ACH of air change is allowed for the rest of the day. The assembly equation is provided below:

$$Air\_change\ (\text{ACH}) = daytime \times 537 + 358 \qquad (7.1)$$

where *daytime* is a function which is scheduled in Type 14h. This equation is similar to Type 56 where the building characteristics are created.

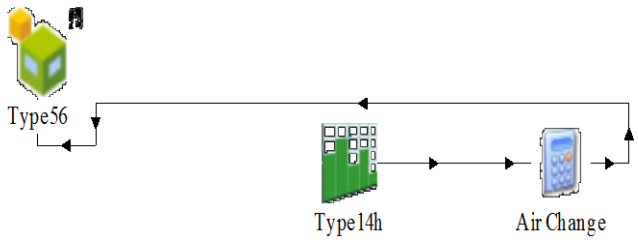

Figure 7.1 Air change schedule through a day

- The indoor air is re-circulated and mixed with a fraction of the fresh air as performed in the previous step in a scheduled amount as defined above. The fresh air temperature is provided from Type9A for the month of July in Montreal, and the re-circulated air temperature is delivered from Type56. The mixed air temperature obtained from Eq. (7.2)

is similar to the data supplied by Type56 for scheduling the air change ventilation, as shown in Figure 7.2.

$$Temp_{Mixed} = \begin{cases} Temp_{out}, & daytime = 1 \\ Temp_{out} + (Temp_{return} - Temp_{out}), & daytime = 0 \end{cases} \quad (7.2)$$

where $Temp_{Mixed}$ is the mixed air temperature, ℃, $Temp_{out}$ is the ambient fresh air temperature, ℃, $Temp_{return}$ is the re-circulated indoor air temperature, ℃. The mixed air temperature is linked to the centralized LHTES system function.

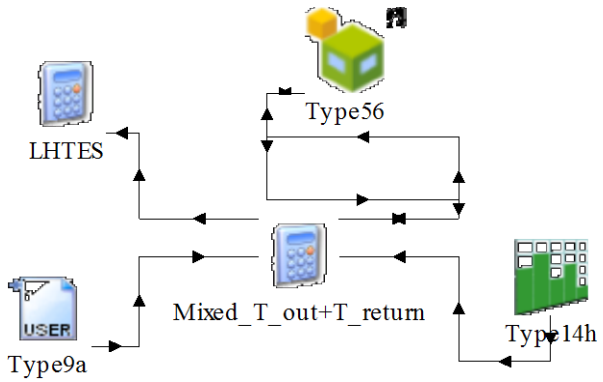

Figure 7.2 Mixing re-circulated and fresh air exchange schedule through a day

- The centralized LHTES Type is a function of time and temperature. This function is obtained after simulating a 3-D LHTES transient numerical model to solve the heat transfer phase change problem of paraffin RT20 during the month of July. Eq. (7.3), which is a second-order polynomial formula, represents the outlet air temperature of the centralized LHTES system. This formula is obtained after ANN training with data extracted from a CFD simulation for a centralized LHTES system of 650mm in length.

$$Temp_{LHTES} = 2.7 \times 10^{-5} + 6.3 \times 10^{-3} \times Time - 4.1 \times 10^{-5} \times Temp - 2.3 \times 10^{-6} \times Time^2 - 0.03 \times Temp^2 + 5.9 \times 10^{-3} \times Time \times Temp \quad (7.3)$$

where $Temp_{LHTES}$ is the outlet air temperature of the centralized LHTES system (°C), $Time$ is the simulation time (hr), recalled from Type9A since the ambient air temperature reading is based on hourly changes according to the weather data for Montreal. Figure 7.3 shows that $Temp$ is the temperature of the mixed air temperature and how $Temp_{LHTES}$ is linked to evaluate whether it is allowed to supply into the building for cooling purposes or not, based on the desired indoor conditions.

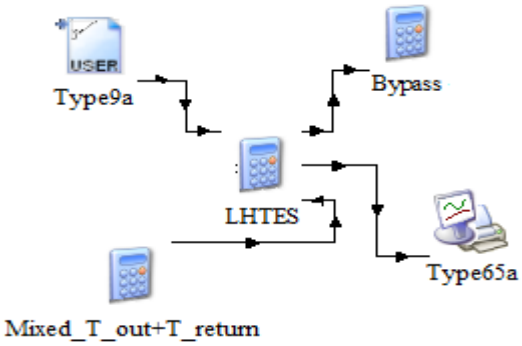

Figure 7.3 LHTES network connection

- A bypass ventilation control is applied to ensure suitable ventilation for the building. The temperature of the mixed air, which includes fresh ambient air and the LHTES's outlet air temperature, is linked to the bypass check point. A lower air temperature is chosen to be supplied into the building based on the Type56 information, using a control functions as shown in Figure 7.4. The control function has two conditions; the first condition is to check the air stream temperatures from the outside environment and from the centralized LHTES system. The second condition is to check the temperatures of the outdoor air stream and of the re-circulated air stream. Thereafter, the control function is used to select the air stream which has a lower air temperature to be supplied into the building, as illustrated in Eq. (7.4).

Condition one; $Test = Temp_{return} - Temp_{LHTES}$

Condition two; $Test_{amb} = Temp_{out} - Temp_{return}$

$$T_{result} = \begin{cases} Temp_{LHTES}, & if \quad Test > 0 \\ Temp_{return}, & if \quad Test_{amb} > 0 \; and \; Test < 0 \end{cases} \tag{7.5}$$

where $Temp_{LHTES}$ is the LHTES's outlet air-temperature, ℃, $Temp_{return}$ is the re-circulated indoor air temperature, ℃, and $Temp_{out}$ is the ambient fresh air temperature, ℃.

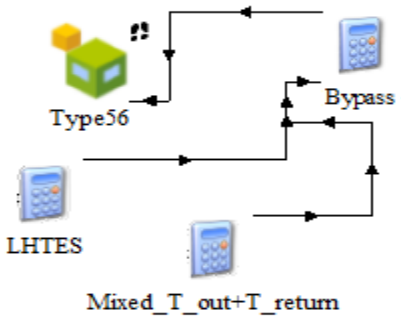

Figure 7.4 Bypass ventilation network connections

2- During the charging period, from 7:00PM until 6:00AM, higher air flow rates are preferable to solidify the PCM since the ambient temperatures are relatively lower than the PCM melting point temperature. This cycle is repeated, as illustrated in Figure 7.3.

The test room is occupied by two persons from 8:00AM to 12:00PM and from 1:00PM to 5:00PM Monday through Friday. During this occupancy there is a constant additional load of 150W (television) and 100W for electric lights. For more details on the simulation boundary conditions, (see Appendix B). Typical Meteorological Year (TMY)

weather file data is used. The weather data (ambient air temperature and solar radiation intensity) is generated using TRNSYS Type TMY2.

The model building is simulated by considering the given assumptions to investigate the effect of integrating the LHTES system on the reducing energy demand. Figure 7.5 shows the variation of the indoor air temperature which is affected by the supply and the LHTES's outlet air-temperatures. During the month of July, it is obvious that the value of ambient air temperature goes down in the middle of the week, which enhances the night ventilation and therefore the LHTES system is almost completely charged. However, the opportunity to take advantage of night ventilation decreases when the ambient air temperature increases, causing an increase of the indoor air-temperature. In general, the value of indoor air-temperature is relatively weighted to the summation of the supply and LHTES's outlet air-temperatures, as illustrated in Figure 7.6.

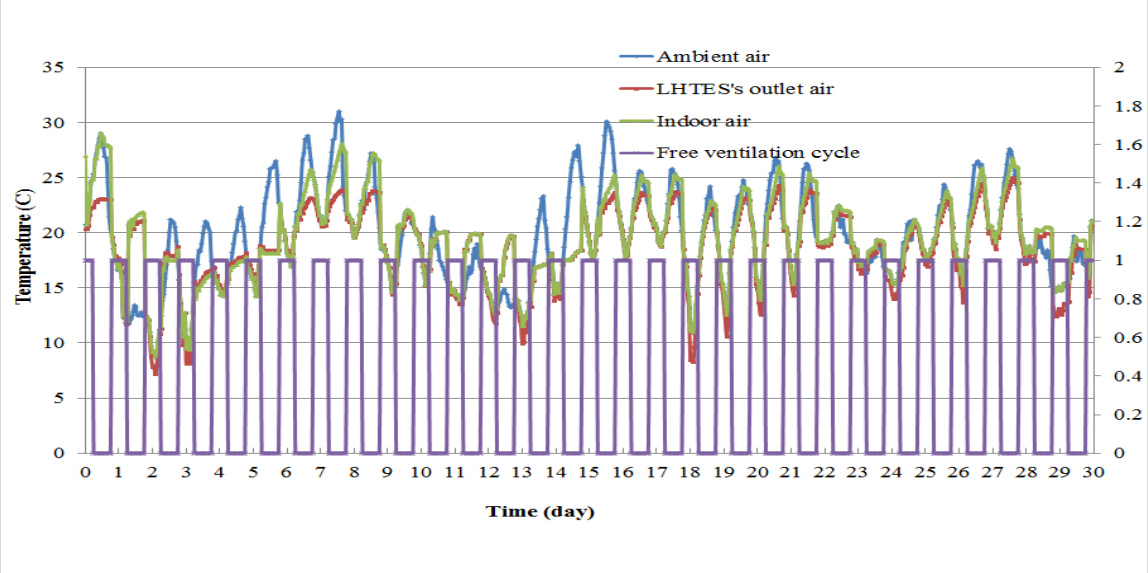

Figure 7.5 The variation of indoor air-temperature of the building model integrated into the LHTES system for a passive space

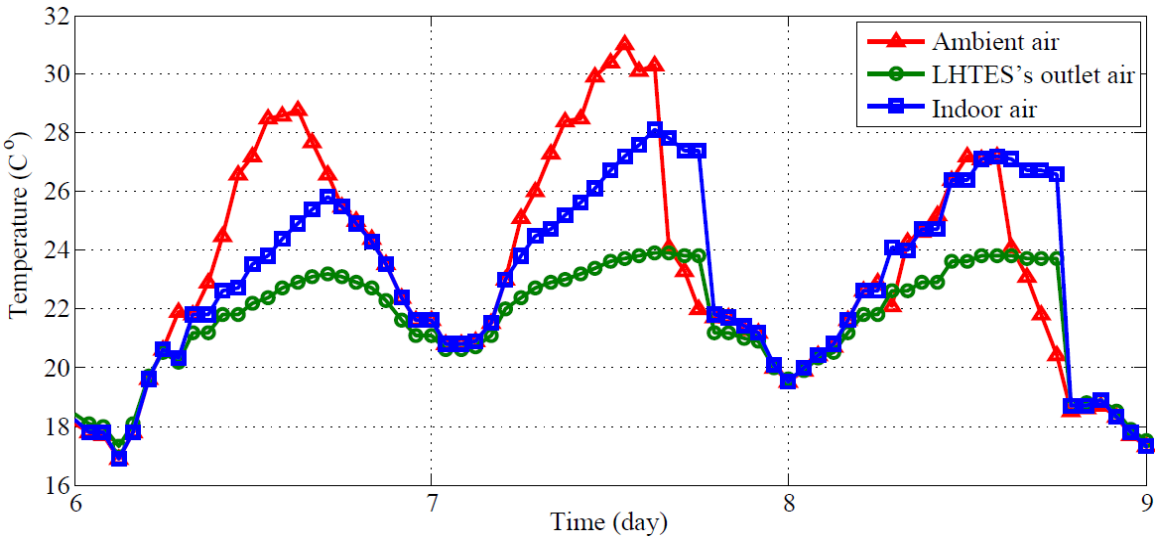

Figure 7.6 The variation of indoor air-temperature of the building model integrated into the LHTES system for days 6-9 of July for a passive space

Figure 7.7 shows different scenarios of indoor air-temperature using the LHTES system and the night ventilation mode. No auxiliary cooling is provided during the selected period. To analyze the effect of a night ventilation system with and without the centralized LHTES system, three days (July 6-9) are chosen from the summer season. The LHTES's response function in conjunction with night ventilation has a significant effect on reducing the variations of indoor air temperature compared to only implementing night ventilation. This is attributed to the thermal storage effect of the centralized LHTES system, in which the air stream coldness is stored during the night and then it is released to the indoor air during the day. The cooling effect of the centralized LHTES system lasts from 9:00 in morning to 17:00 in afternoon, when the PCM almost completely melts. This suggests that the centralized LHTES system can not only stabilize the temperature swing but also improve building occupant's comfort. As

can be seen from Figure 7.7, the indoor air-temperature rises due to the internal load when there is no mechanical ventilation system.

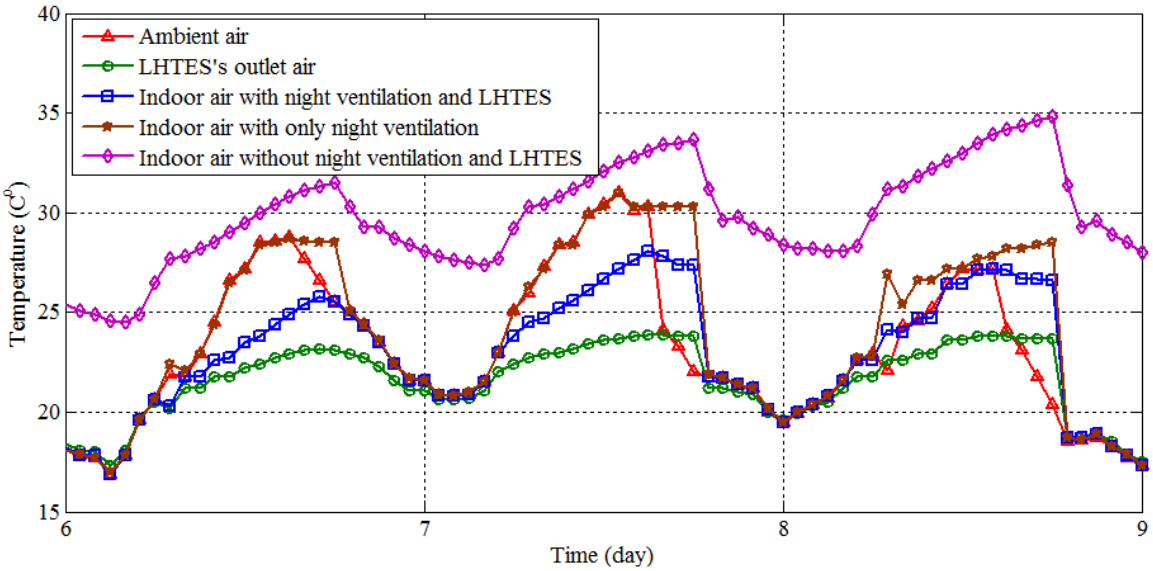

Figure 7.7 Indoor air-temperature histories with and without LHTES system combined with night ventilation for days 6-9 of July

The indoor air-temperature is calculated when only the night ventilation system is applied and scheduled as mentioned in the previous section. The indoor air-temperature line overlaps the ambient air-temperature line from early morning to about mid-day, and then the indoor air-temperature increases and remains higher than the ambient air temperature. An auxiliary cooling supply is needed to maintain the indoor air-temperature within the comfortable range below 28℃ because of high ACH during the daily operation of the system.

7.3 Design evaluation of LHTES for cooling

7.3.1 Development of ANN to characterize the optimal LHTES's performance

The optimal design and characterization of a centralized LHTES system are investigated for reducing the cooling demand under different boundary conditions. Three different models, each of which has a different mesh constructed according to its size and computational domain (i.e., 500, 650, 750mm), are used to discretize the LHTES unit for estimating the stored cooling energy. Each model is then simulated using the CFD solver for selected typical days, as the inlet air temperature varies based on hourly changes, in accordance to the weather data [111]. Thereafter, the database obtained from CFD simulations for each model is used to train the ANN method for the long-term prediction of this LHTES system's performance. Each model has a trained ANN's response function which reflects the LHTES system's outlet air temperature for summer season.

The trained ANN's response function is integrated into the TRNSYS building thermal response model which was described in section 3.4.1. A ventilation system that operates in two modes is installed. One mode ventilates the cooling space with a constant air flow rate at 2 ACH throughout the day. The second mode is set up to supply a relatively cold air stream during the night time, or the night ventilation mode. Type 14h is scheduled to allow the air change per hour (ACH) to be changed from 1 to 11 to supply into the building during the period of 7:00PM-6:00AM, which is an appropriate time period for night ventilation. To this end, a fan with variable electrical power is required. Fan power calculations are performed according to the changes required for the varying ACH. The average stored cooling energy is determined for each LHTES system model, combined with the fan energy consumption for several values of ACH.

The thermal performance of the centralized LHTES system combined with night ventilation is investigated numerically. The system is charged during the night (7:00PM to 6:00AM) by night ventilation with a variable air change per hour (ACH). Then, the stored cooling energy is discharged to the building model's environment during the daytime hours (7:00AM-6:00PM). Figure 7.8 shows the stored cooling energy release for three LHTES unit models verses the electrical energy required for the ventilating fan. The cold energy released increases with fan energy consumption, since a higher ACH with night ventilation leads to higher rates of the PCM's solidification period (charging process), resulting in an increase of the cooling energy curve in an exponential trend. For instance, when the ACH reaches 10, the calculated pressure loss of the air-flow through the building model is 87 Pa and the required fan power is 50W. As can be seen from Figure 7.8, the cooling energy extracted from either the first storage unit of 750mm length or the second one of 650mm length is higher than that of the third one of 500mm length. However, the thermal performances for the first storage unit of 750mm length and for the second one of 650mm length are relatively similar. Therefore, the second storage unit model of 650mm length appears to be more efficient for cooling purposes as compared to the first storage model of 750mm length in terms of economic benefits. It is concluded that the design optimization of a centralized LHTES is found to be the second storage model of 650mm length.

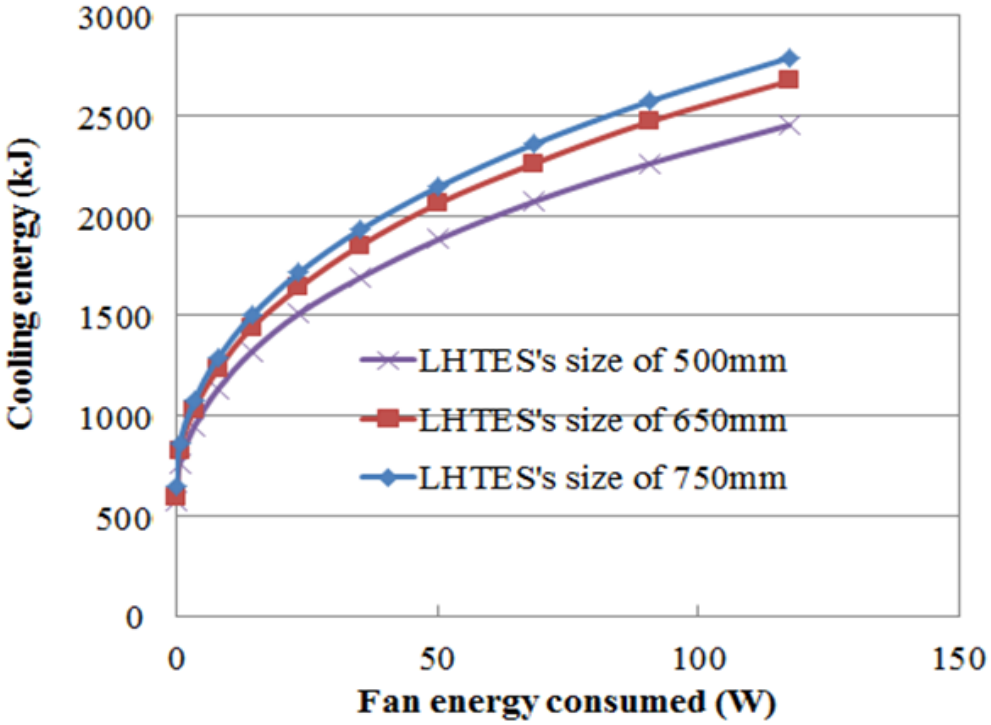

Figure 7.8 The stored cooling energy released for three different-sized LHTES system models verses the fan energy consumed

7.4 Summary and conclusion

A design of a centralized LHTES system is evaluated based on the stored cooling energy and the LHTES system's size. A validated 3-D centralized LHTES transient numerical model is used to solve the conjugate phase change heat transfer and fluid flow problems using the CFD commercial package, Fluent. The centralized LHTES system is filled with paraffin RT20 and is enhanced with fins embedded at the top and bottom of its surfaces. The LHTES system is integrated with the mechanical ventilation system of a low-energy TRNSYS building model to provide the required indoor thermal conditions combined with night ventilation. To analyze the optimized performance of the centralized LHTES system and its contribution to enhance building energy performance, two operational strategies are applied. First, a charging period strategy is applied from

7:00PM until 6:00AM. Higher air flow rates are preferable to solidify the PCM, since the ambient air temperature is relatively lower than the PCM's melting temperature.

A control strategy for a ventilated room is established to ensure that the internal air room temperature does not exceed 25℃. The daily ambient air temperature variations are recorded based on hourly changes. A discharge period is applied when relatively low air flow rates are allowed to pass over a canalized LHTES system from 6:00AM until 7:00PM, thereby reducing the fluctuation of indoor air-temperatures. The outlet LHTES system's air temperatures for three LHTES models are numerically calculated for selected typical summer days. The calculation time is computationally expensive, and so the simulations are performed separately for the first days of each week through the month, in turn; the numerical database is used to train the artificial neural networks (ANN) model. Thereafter, the LHTES's outlet air-temperatures are extrapolated over the entire summer, from the beginning of June to the end of August. The reduction of the indoor air-temperature is found in the range of 1.5-2.5℃. The results show the optimal performance design of a centralized LHTES system can be achieved using the medium-scale 650 mm models.

Chapter 8

Summary, Conclusion, Contributions, and Future Work

8.1 Summary

The characterization of a centralized latent heat thermal storage system was investigated in this dissertation. The evolution of the phase change of a rectangular cavity filled with PCM was investigated using a developed 2-D mathematical model and the model prediction was verified with experimental data. The thermo-physical properties of PCMs were varied for a wide temperature ranges for paraffin RT20. The effect of the specific heat capacity on the thermal performance of a centralized LHTES system was studied. The evolution of liquid and solid fractions was explored at different inlet air-temperature conditions.

PCM technology is recommended as a storage medium for use in building to reduce the peak demand. In this context, a practical model for LHTES systems is required for their implementation in buildings. To this end, a 3-D model for the transient phase change heat transfer problem is conducted and validated with the experimental data. To achieve more accuracy, the complete conservation equations were solved simultaneously for solid and liquid PCMs and for solid fins. Several meshes are structured to discover the effect of grid dependency on the solution. The numerical results obtained from the developed model were thus validated with experimental data.

The thermal performance of the model was evaluated so that it may be implemented in buildings. Hence, the centralized LHTES system was integrated into a

mechanical ventilation system. LHTES design parameters were investigated by simulating the LHTES system performance with realistic boundary conditions. The effects of the phase change temperature range, the flow rate of HTF, of the geometrical configuration of a LHTES system, and of fin size and the length of a unit on the output temperatures of the HTF and the reduction of the ventilation load were assessed. Since calculation time is computationally expensive, the thermal performance of the centralized LHTES system was predicted using an ANN method by extrapolating the LHTES system's outlet air-temperatures over the entire summer season. The reduction of ventilation load was determined for typical selected days. The centralized LHTES system was integrated into the building simulation model. The dynamic passive solar model of a mono-zone building with a thermally internal load was investigated using TRNSYS.

8.2 Conclusion

The findings of this thesis are elaborated in the following steps:

1- A 3-D numerical model is conducted to analyze the transient heat transfer during the phase change process of a PCM in a centralized LHTES system which can be integrated into a building's mechanical ventilation system. The numerical results are compared with experimental data and the results of that comparison show a good agreement, which could be attributed to having including the convective effect during the melting period.

2- A parametric study is performed to investigate the effect of the design parameters on the thermal performance of a centralized LHTES system. The thermo-physical properties of a PCM are set as a variant, with the temperature parameters to be

investigated through different scenarios of the inlet air condition. It is found that the most influential property is the specific heat capacity. The results show that the effective specific heat capacity, which is obtained from DSC measurements, gives a more accurate indication for predicting the behaviour of phase change evolution. In addition, the thermal conductivity and the viscosity of a PCM are handled so that they can accommodate the temperature variation. The geometrical configuration of a physical model is investigated in terms of fin size and according to the size of the model itself. The fin sizes are varied in terms of their thickness, from 0.6mm to 1.5mm, and the simulations are run based on hourly changes of inlet air conditions to determine its contribution in enhancing the heat exchange between the HTF and the PCM. The numerical result obtained shows that the charging time is relatively shortened when the fin thickness is decreased, resulting in additional stored energy. The size of the centralized LHTES system is enlarged by increasing the length from 500-750mm and then two different scenarios of air stream flow rates, 1.5m/s, 2.4m/s, are allowed to pass over the LHTES system under realistic boundary conditions. The outlet's LHTES air-temperature is remarkably decreased compared to that of the inlet air-temperature at the longer sizes. Hence, it has a significant potential to be used as means for cooling purposes in buildings.

3- The rate of recovering the stored energy from the centralized LHTES system is quantitatively improved when the temperature difference between the HTF and the mean melting point of PCM is greater than 10K.

4- The centralized LHTES system is integrated into a mechanical ventilation system in order to determine its contribution to reducing the required ventilation load. From perspective of the PCM's thermo-physical properties, the maximum reduction of the cooling ventilation load is 48% when the phase change temperature range is 4K for a typical July day. A control strategy is applied to calculate the ventilation load reduction when the inlet air-temperature is higher than the desired indoor air-temperature and the LHTES's outlet air-temperature is equal to or lower than the desired indoor air temperature. When both the inlet and the LHTES system's outlet air-temperatures are higher than the desired indoor air-temperature but the LHTES system's outlet air- temperature is lower than the inlet air-temperatures, the maximum ventilation load reduction is attained with a phase change temperature range of DSC and 12K by 67% and 61%, respectively.

5- The stored cooling energy recovered by the centralized LHTES system is investigated at three different design sizes. The retrieved cold energy contributes to reducing the ventilation load, which is the total daily required ventilation at similar air flow rate conditions, 1.5m/s, by 36% with the 650mm length, compared to 21% with the 500mm length. For the system length size of 750mm, the cooling reduction reaches 38%. This percentage of cooling reduction does not increase with increased air flow rates for all of the cases studied.

6- The optimal size of the centralized LHTES system in terms of storing/retrieving cooling energy is found to be the 650mm length with paraffin RT20 as the PCM. This suggests that the predicted thermal performance of the centralized LHTES

system can be utilized to stabilize the daily variations of indoor air-temperatures and to improve the environmental footprint of buildings.

7- The thermal performance of the centralized LHTES system is predicted over the entire summer season using the ANN approach because the calculation time of CFD simulation for a 3-D numerical phase change model is computationally expensive. The simulations are performed to calculate the LHTES's outlet air-temperature for two days of each week. The database obtained from the CFD simulation is used to train the ANN method; the prediction of a LHTES system's outlet air-temperature is then extrapolated to cover a certain time of year. The trained ANN is proven to be an effective tool to predict the thermal performance of a centralized LHTES system with reasonable accuracy.

8- The centralized LHTES system is integrated into a building model with a mechanical ventilation system through the TRNSYS building simulation tool. The objective is to investigate the contribution of the centralized LHTES system in reducing the indoor air-temperature which has been charging during the night ventilation using free air streams. The predicted function of the LHTES system's outlet air-temperature combined with the scheduled night ventilation for the month of July indicates that a significant reduction of the indoor air-temperature can be achieved along with reducing the peak energy demand by about 1.5-2.5℃.

9- Finally, a design tool for predicting the long-term performance of a centralized LHTES system is developed. To this end, a design optimization of the centralized LHTES system is carried out based on its thermal response to the building cooling load characterization. Three models of the centralized LHTES system are selected

to be optimized in tandem with night ventilation for use inside buildings (i.e., the large-scale 750mm long model and the medium-scale model of 650mm are both higher than that of the little-medium-scale model of 500mm). After implementing the trained ANN to predict the LHTES system's outlet air-temperatures for the three selected models, the ACH plays an important role in enhancing a building's thermal response. Generally, as a fan supplies higher airflow rates, the thermal performance of the selected models is significantly increased. However, the optimal design for the centralized LHTES system is characterized based on the average stored cooling energy over the whole summer season. The results indicate that the medium-scale of the centralized LHTES system is found to have the most favourable impact on enhancing the comfort level inside buildings while achieving a high level of energy demand shift.

8.3 Contributions and list of publications

The major contributions of this dissertation are summarized as following:

- An effective design tool to predict the thermal performance of a centralized LHTES system is developed taking into account the heat exchange phenomenon between PCM and HTF through solid extended surfaces.
- 3-D PCM numerical modelling is implemented to solve complete conservation equations for a convection-diffusion phase change problem. The numerical result is verified using experimental data available in literature. Also, normalization study is performed to make a proper scale for collapsing the numerical result. The

discharging behavior is characterized by variable Ra, Re, and Ste numbers for several different scenarios of inlet air conditions. This is the first report to explore that the performance efficiency of LHTES system during the discharging period is maximized when the temperature difference between the inlet air and the mean melting point is 10K at phase change temperature range of 12K.

- Three sizes of LHTES are evaluated through a parametric study to assess their thermal response for hourly variations of the inlet air temperature. As a simulation time is computationally expensive, ANN is developed to extrapolate the numerical result over a long-term for performance prediction on a selected season period. Thus, the LHTES thermal response function is utilized to determine the sored cooling energy. This research is the first in the literature to provide an assessment for cooling load reduction over a long-term period.
- Finally, a low-energy building using a mechanical ventilation system with the trained ANN's response function combined with night ventilation is simulated to investigate the cooling load reduction. There sizes of LHTES are simulated including the power fan required to evaluate the best LHTES size for maximum cooling energy release.

List of publications

1) "Centralized latent heat thermal energy storage system: Model development and validation", *Energy and Buildings*, 2013; 65:260-71
2) "Assessing long-term performance of centralized thermal energy storage system", *Applied Thermal Engineering,* 2014; 62:313-21

3) "Assessment and prediction of the thermal performance of a centralized latent heat thermal energy storage utilizing artificial neural networks", presented at the *2013 International Conference for Enhanced Building Operations* (ICEBO).

8.4 Future work

This work provides a design model of a centralized LHTES system which is proven with a primary experimental model. The design parameters are investigated through a parametric study. The findings can serve as a guide to fabricate models to meet free cooling application needs. From the thermo-physical PCM perspective, since centralized LHTES systems have the potential to be integrated into low-energy buildings, chemically-improved types of PCMs should be tested to identify and maximize their optimal thermal performance. Additionally, the heat exchange between the HTF and PCM needs to be investigated by applying different enhancement techniques.

References

[1] Oro E, de Gracia A, Castell A, Farid MM, Cabeza LF. Review on phase change materials (PCMs) for cold thermal energy storage applications. Applied Energy. 2012;99:513-33.

[2] Al-Saadi SN, Zhai Z. Modeling phase change materials embedded in building enclosure: A review. Renewable and Sustainable Energy Reviews. 2013;21:659-73.

[3] Gunther E, Mehling H, Hiebler S. Modeling of subcooling and solidification of phase change materials. Modelling and Simulation in Materials Science and Engineering. 2007;15:879-92.

[4] Connolly D, Lund H, Mathiesen BV, Leahy M. A review of computer tools for analysing the integration of renewable energy into various energy systems. Applied Energy. 2010;87:1059-82.

[5] Zhou D, Zhao CY, Tian Y. Review on thermal energy storage with phase change materials (PCMs) in building applications. Applied Energy. 2012;92:593-605.

[6] Zalba B, MarÄ±Ì□n JM, Cabeza LF, Mehling H. Review on thermal energy storage with phasechange: materials, heat transfer analysis and applications. Applied thermal engineering. 2003;23:251-83.

[7] Sharma A, Tyagi VV, Chen CR, Buddhi D. Review on thermal energy storage with phase change materials and applications. Renewable and Sustainable Energy Reviews. 2009;13:318-45.

[8] Agyenim F, Hewitt N, Eames P, Smyth M. A review of materials, heat transfer and phase change problem formulation for latent heat thermal energy storage systems (LHTESS). Renewable and Sustainable Energy Reviews. 2010;14:615-28.

[9] Parameshwaran R, Kalaiselvam S, Harikrishnan S, Elayaperumal A. Sustainable thermal energy storage technologies for buildings: A review. Renewable and Sustainable Energy Reviews. 2012;16:2394-433.

[10] Alawadhi EM. Thermal analysis of a building brick containing phase change material. Energy & Buildings. 2008;40:351-7.

[11] Weinlader H, Beck A, Fricke J. PCM-facade-panel for daylighting and room heating. Solar Energy. 2005;78:177-86.

[12] Evers AC, Medina MA, Fang Y. Evaluation of the thermal performance of frame walls enhanced with paraffin and hydrated salt phase change materials using a dynamic wall simulator. Building and Environment. 2010;45:1762-8.

[13] Diaconu BM, Cruceru M. Novel concept of composite phase change material wall system for year-round thermal energy savings. Energy and Buildings. 2010;42:1759-72.

[14] Hammou ZA, Lacroix M. A new PCM storage system for managing simultaneously solar and electric energy. Energy and Buildings. 2006;38:258-65.

[15] Kosny J, Yarbrough D, Dpe P, Miller W, Petrie T, Childs P, et al. PCM-Enhanced Building Envelopes in Current ORNL Research Projects, Oak Ridge National Laboratory, 2007, http://www.ornl.gov/sci/.index.shtml/.

[16] Peippo K, Kauranen P, Lund PD. A multicomponent PCM wall optimized for passive solar heating. Energy and Buildings. 1991;17:259-70.

[17] Guobing Z, Yinping Z, Xin W, Kunping L, Wei X. An assessment of mixed type PCM-gypsum and shape-stabilized PCM plates in a building for passive solar heating. Solar Energy. 2007;81:1351-60.

[18] Ismail KAR, Castro JNC. PCM thermal insulation in buildings. International Journal of Energy Research. 1997;21:1281-96.

[19] Chen C, Guo H, Liu Y, Yue H, Wang C. A new kind of phase change material (PCM) for energy-storing wallboard. Energy and Buildings. 2008;40:882-90.

[20] Athienitis AK, Liu C, Hawes D, Banu D, Feldman D. Investigation of the thermal performance of a passive solar test-room with wall latent heat storage. Building and Environment. 1997;32:405-10.

[21] Stetiu C, Feustel HE. Phase-change wallboard and mechanical night ventilation in commercial buildings. Lawrence Berkeley National Laboratory. 1998.

[22] Boehm RF, Halford CK. Modeling of phase change material peak load shifting. Energy and Buildings. 2007;39:298-305.

[23] Koschenz M, Lehmann B. Development of a thermally activated ceiling panel with PCM for application in lightweight and retrofitted buildings. Energy and Buildings. 2004;36:567-78.

[24] Zhu N, Ma Z, Wang S. Dynamic characteristics and energy performance of buildings using phase change materials: A review. Energy Conversion and Management. 2009;50:3169-81.

[25] Jegadheeswaran S, Pohekar SD. Performance enhancement in latent heat thermal storage system: a review. Renewable and Sustainable Energy Reviews. 2009;13:2225-44.

[26] Fan L, Khodadadi JM. Thermal conductivity enhancement of phase change materials for thermal energy storage: A review. Renewable and Sustainable Energy Reviews. 2011;15:24-46.

[27] Baby R, Balaji C. Experimental investigations on phase change material based finned heat sinks for electronic equipment cooling. International Journal of Heat and Mass Transfer. 2012;55:1642-9.

[28] Yuwen Z, Faghri A. Heat transfer enhancement in latent heat thermal energy storage system by using the internally finned tube. International Journal of Heat and Mass Transfer. 1996;39:3165-73.

[29] Stritih U. Heat transfer enhancement in latent heat thermal storage system for buildings. Energy and Buildings. 2003;35:1097-104.

[30] Lamberg P. Approximate analytical model for two-phase solidification problem in a finned phase-change material storage. Applied Energy. 2004;77:131-52.

[31] Stritih U. An experimental study of enhanced heat transfer in rectangular PCM thermal storage. International Journal of Heat and Mass Transfer. 2004;47:2841-7.

[32] Shatikian V, Ziskind G, Letan R. Numerical investigation of a PCM-based heat sink with internal fins. International Journal of Heat and Mass Transfer. 2005;48:3689-706.

[33] Henze RH, Humphrey JAC. Enhanced heat conduction in phase-change thermal energy storage devices. International journal of heat and mass transfer. 1981;24:459-74.

[34] Ye W-B, Zhu D-S, Wang N. Numerical simulation on phase-change thermal storage/release in a plate-fin unit. 17-18 ed. Langford Lane, Kidlington, Oxford, OX5 1GB, United Kingdom: Elsevier Ltd; 2011. p. 3871-84.

[35] Raj VAA, Velraj R. Review on free cooling of buildings using phase change materials. Renewable and Sustainable Energy Reviews. 2010;14:2819-29.

[36] Turnpenny JR, Etheridge DW, Reay DA. Novel ventilation cooling system for reducing air conditioning in buildings. Part I: Testing and theoretical modelling. Applied Thermal Engineering. 2000;20:1019-37.

[37] Etheridge D, Murphy K, Reay D. A PCM/heat pipe cooling system for reducing air conditioning in buildings: review of options and report on field tests. Building Services Engineering Research & Technology. 2006;27:27-39.

[38] Marin JM, Zalba B, Cabeza LF, Mehling H. Improvement of a thermal energy storage using plates with paraffin-graphite composite. International Journal of Heat and Mass Transfer. 2005;48:2561-70.

[39] Sanusi O, Warzoha R, Fleischer AS. Energy storage and solidification of paraffin phase change material embedded with graphite nanofibers. International Journal of Heat and Mass Transfer. 2011;54:4429-36.

[40] Takeda S, Nagano K, Mochida T, Shimakura K, Nakamura T. Study of a floor supply air conditioning system using granular phase change material to augment building mass thermal storage-Heat response in small scale experiments. Energy and Buildings. 2006;38:436-46.

[41] Mettawee EBS, Assassa GMR. Thermal conductivity enhancement in a latent heat storage system. Solar Energy. 2007;81:839-45.

[42] Guo C, Dong H, Wei X. Performance enhancement of a PCM cold storage under condition of heat flux. Wuhan, China: IEEE Computer Society; 2010. p. 499-502.

[43] Mosaffa AH, Talati F, Rosen MA, Tabrizi HB. Approximate analytical model for PCM solidification in a rectangular finned container with convective cooling boundaries. International Communications in Heat and Mass Transfer. 2012;39:318-24.

[44] Jeon J, Lee J-H, Seo J, Jeong S-G, Kim S. Application of PCM thermal energy storage system to reduce building energy consumption. Journal of Thermal Analysis and Calorimetry. 2013;111:279-88.

[45] Cabeza LF, Castell A, Barreneche C, de Gracia A, Fernandez AI. Materials used as PCM in thermal energy storage in buildings: A review. 2011;15:1675-95.

[46] Medved S, Arkar C. Correlation between the local climate and the free-cooling potential of latent heat storage. Energy and Buildings. 2008;40:429-37.

[47] Waqas A, Kumar S. Thermal performance of latent heat storage for free cooling of buildings in a dry and hot climate: An experimental study. Energy and Buildings. 2011;43:2621-30.

[48] Halawa E, Saman W. Thermal performance analysis of a phase change thermal storage unit for space heating. Renewable Energy. 2011;36:259-64.

[49] Halawa E, Saman W, Bruno F. A phase change processor method for solving a one-dimensional phase change problem with convection boundary. Renewable Energy. 2010;35:1688-95.

[50] Liu M, Saman W, Bruno F. Validation of a mathematical model for encapsulated phase change material flat slabs for cooling applications. Applied Thermal Engineering. 2011;31:2340-7.

[51] Gadgil A, Gobin D. Analysis of two-dimensional melting in rectangular enclosures in presence of convection. Transactions of the ASME Journal of Heat Transfer. 1984;106:20-6.

[52] Ho CJ, Viskanta R. Heat transfer during melting from an isothermal vertical wall. Transactions of the ASME Journal of Heat Transfer. 1984;106:12-9.

[53] Brent AD, Voller VR, Reid KJ. Enthalpy-porosity technique for modeling convection-diffusion phase change: application to the melting of a pure metal. Numerical Heat Transfer. 1988;13:297-318.

[54] Wang Y, Amiri A, Vafai K. An experimental investigation of the melting process in a rectangular enclosure. International Journal of Heat and Mass Transfer. 1999;42:3659-72.

[55] Lazaro A, Dolado P, Marin JM, Zalba B. PCM-air heat exchangers for free-cooling applications in buildings: Empirical model and application to design. Energy Conversion and Management. 2009;50:444-9.

[56] Xiang-Qi W, Mujumdar AS, Yap C. Effect of orientation for phase change material (PCM)-based heat sinks for transient thermal management of electric components. International Communications in Heat and Mass Transfer. 2007;34:801-8.

[57] Lazaro A, Dolado P, Marin JM, Zalba B. PCM-air heat exchangers for free-cooling applications in buildings: Experimental results of two real-scale prototypes. Energy Conversion and Management. 2009;50:439-43.

[58] Tan FL, Hosseinizadeh SF, Khodadadi JM, Liwu F. Experimental and computational study of constrained melting of phase change materials (PCM) inside a spherical capsule. International Journal of Heat and Mass Transfer. 2009;52:3464-72.

[59] Vakilaltojjar SM, Saman W. Analysis and modelling of a phase change storage system for air conditioning applications. Applied Thermal Engineering. 2001;21:249-63.

[60] Zalba B, Marin JM, Cabeza LF, Mehling H. Review on thermal energy storage with phase change: materials, heat transfer analysis and applications. Applied Thermal Engineering. 2003;23:251-83.

[61] Dutil Y, Rousse DR, Salah NB, Lassue S, Zalewski L. A review on phase-change materials: Mathematical modeling and simulations. Renewable and Sustainable Energy Reviews. 2011;15:112-30.

[62] Tay NHS, Bruno F, Belusko M. Experimental validation of a CFD model for tubes in a phase change thermal energy storage system. International Journal of Heat and Mass Transfer. 2012;55:574-85.

[63] Wu S, Fang G, Chen Z. Discharging characteristics modeling of cool thermal energy storage system with coil pipes using n-tetradecane as phase change material. Applied Thermal Engineering. 2012;37:336-43.

[64] Waqas A, Kumar S. Utilization of latent heat storage unit for comfort ventilation of buildings in hot and dry climates. International Journal of Green Energy. 2011;8:1-24.

[65] Dolado P, Lazaro A, Marin JM, Zalba B. Characterization of melting and solidification in a real scale PCM-air heat exchanger: Numerical model and experimental validation. Energy Conversion and Management. 2012;52:1890-907.

[66] Kang Y, Jiang Y, Zhang Y. Modeling and experimental study on an innovative passive cooling system-NVP system. Energy and Buildings. 2003;35:417-25.

[67] Arkar C, Medved S. Influence of accuracy of thermal property data of a phase change material on the result of a numerical model of a packed bed latent heat storage with spheres. Thermochimica Acta. 2005;438:192-201.

[68] Tan H, Li C, Li Y. Simulation research on PCM freezing process to recover and store the cold energy of cryogenic gas. International journal of thermal sciences. 2011;50:2220-7.

[69] Antony Aroul Raj V, Velraj R. Heat transfer and pressure drop studies on a PCM-heat exchanger module for free cooling applications. International Journal of Thermal Sciences. 2011;50:1573-82.

[70] Mesalhy O, Lafdi K, Elgafy A, Bowman K. Numerical study for enhancing the thermal conductivity of phase change material (PCM) storage using high thermal conductivity porous matrix. Energy Conversion and Management. 2005;46:847-67.

[71] Ming L, Bruno F, Saman W. Thermal performance analysis of a flat slab phase change thermal storage unit with liquid-based heat transfer fluid for cooling applications. Solar Energy. 2011;85:3017-27.

[72] Colella F, Sciacovelli A, Verda V. Numerical analysis of a medium scale latent energy storage unit for district heating systems. Energy. 2012;45:397-406.

[73] Rodriguez-Ubinas E, Ruiz-Valero L, Vega S, Neila J. Applications of Phase Change Material in highly energy-efficient houses. Energy and Buildings. 2012;50:49-62.

[74] Stritih U, Butala V. Experimental investigation of energy saving in buildings with PCM cold storage. International Journal of Refrigeration. 2010;33:1676-83.

[75] Stritih U, Butala V. Energy savings in building with a PCM free cooling system. Strojniski Vestnik. 2011;57:125-34.

[76] Yam J, Yuguo L, Zuohuan Z. Nonlinear coupling between thermal mass and natural ventilation in buildings. International Journal of Heat and Mass Transfer. 2003;46:1251-64.

[77] Costa M, Buddhi D, Oliva A. Numerical simulation of a latent heat thermal energy storage system with enhanced heat conduction. Energy Conversion and Management. 1998;39:319-30.

[78] Zalba B, Marin JM, Cabeza LF, Harald M. Free-cooling of buildings with phase change materials. International Journal of Refrigeration. 2004;27:839-49.

[79] Arkar C, Medved S. Free cooling of a building using PCM heat storage integrated into the ventilation system. Solar Energy. 2007;81:1078-87.

[80] Arkar C, Vidrih B, Medved S. Efficiency of free cooling using latent heat storage integrated into the ventilation system of a low energy building. International Journal of Refrigeration. 2007;30:134-43.

[81] Lamberg P, Lehtiniemi R, Henell A-M. Numerical and experimental investigation of melting and freezing processes in phase change material storage. International Journal of Thermal Sciences. 2004;43:277-87.

[82] Voller VR, Cross M, Markatos NC. An enthalpy method for convection/diffusion phase change. International Journal for Numerical Methods in Engineering. 1987;24:271-84.

[83] Voller VR, Swaminathan CR. General source-based method for solidification phase change. Numerical Heat Transfer, Part B (Fundamentals). 1991;19:175-89.

[84] Voller VR. Fast implicit finite-difference method for the analysis of phase change problems. Numerical Heat Transfer, Part B (Fundamentals). 1990;17:155-69.

[85] Shamsundar N, Rooz E. Numerical methods for moving boundary problems. Handbook of Numerical Heat Transfer. 1988:747-86.

[86] Voller V. An implicit enthalpy solution for phase change problems: with application to a binary alloy solidification. Applied Mathematical Modelling. 1987;11:110-6.

[87] Swaminathan CR, Voller VR. A general enthalpy method for modeling solidification processes. Metallurgical Transactions B (Process Metallurgy). 1992;23B:651-64.

[88] Qiang S, Xing Y-M, Mu L, Wu B. Numerical research of solid-liquid phase change process in porous media. Shanghai, China: IEEE Computer Society; 2011. p. 650-4.

[89] Tao YB, He YL. Numerical study on thermal energy storage performance of phase change material under non-steady-state inlet boundary. Applied Energy. 2011;88:4172-9.

[90] Heim D, Clarke JA. Numerical modelling and thermal simulation of PCM-gypsum composites with ESP-r. Energy and Buildings. 2004;36:795-805.

[91] Darkwa K, O'Callaghan PW, Tetlow D. Phase-change drywalls in a passive-solar building. Applied Energy. 2006;83:425-35.

[92] Yuan F, Medina MA. Proposed modifications for models of heat transfer problems involving partially melted phase change processes. Journal of ASTM International. 2009;6:JAI102059 (20 pp.).

[93] Cao Y, Faghri A. A numerical analysis of phase-change problems including natural convection. Transactions of the ASME Journal of Heat Transfer. 1990;112:812-16.

[94] Zhanhua M, Yuwen Z. Solid velocity correction schemes for a temperature transforming model for convection phase change. International Journal of Numerical Methods for Heat & Fluid Flow. 2006;16:204-25.

[95] Humphries WR, Griggs EI. A design handbook for phase change thermal control and energy storage devices. NASA STI/Recon Technical Report N. 1977;78:15434.

[96] Reid RC, Prausnitz JM, Poling BE. The properties of gases and liquids. 1987.

[97] Patankar SV. Numerical Heat Transfer and Fluid Flow, Hemisphere, New York, 1980. Vol. 1980;1:25-39.

[98] Hirt CW, Nichols BD. Volume of fluid (VOF) method for the dynamics of free boundaries. Journal of Computational Physics. 1981;39:201-25.

[99] Takeda S, Nagano K, Mochida T, Shimakura K. Development of a ventilation system utilizing thermal energy storage for granules containing phase change material. Solar Energy. 2004;77:329-38.

[100] Gau C, Viskanta R. Melting and solidification of a pure metal on a vertical wall. Journal of heat transfer. 1986;108:174-81.

[101] ANSYS FLUENT 12.0 User's Guide RA, Inc. 2009.

[102] Tatsidjodoung P, Le Pierres N, Luo L. A review of potential materials for thermal energy storage in building applications. Renewable and Sustainable Energy Reviews. 2013;18:327-49.

[103] Pal D, Joshi YK. Melting in a side heated tall enclosure by a uniformly dissipating heat source. International Journal of Heat and Mass Transfer. 2001;44:375-87.

[104] Kroeger PG, Ostrach S. The solution of a two-dimensional freezing problem including convection effects in the liquid region. International Journal of Heat and Mass Transfer. 1974;17:1191-207.

[105] Turnpenny JR, Etheridge DW, Reay DA. Novel ventilation cooling system for reducing air conditioning in buildings. I. Testing and theoretical modelling. Applied Thermal Engineering. 2000;20:1019-37.

[106] Zhou G, Yang Y, Xu H. Energy performance of a hybrid space-cooling system in an office building using SSPCM thermal storage and night ventilation. Solar Energy. 2011;85:477-85.

[107] oee.nrcan.gc.ca/sites/oee.nrcan.gc.../EMS_13_fans_and_pumps.pdf.

[108] Change C. Intergovernmental panel on climate change (IPCC). Cambridge University Press: Cambridge; 1995.

[109] Dincer I, Ermis K, Erek A. Heat transfer analysis of phase change process in a finned-tube thermal energy storage system using artificial neural network. International Journal of Heat and Mass Transfer. 2007;50:3163-75.

[110] Sanchez L, Sanchez P, De Lucas A, Carmona M, Rodriguez JF. Using Neural Networks or Linear Models to Predict the Characteristics of Microcapsules Containing Phase Change Materials. Macromolecular Symposia. 2010;287:162-7.

[111] www.climate.weatheroffice.gc.ca.

[112] A. El-Sawi, F. Haghighat, H. Akbari. Centralized latent heat thermal energy storage system: Model development and validation. Energy and Buildings, Energy and the Environment. 2013;http://dx.doi.org/10.1016/j.enbuild.2013.05.027.

[113] Zhou L, Haghighat F. Optimization of ventilation system design and operation in office environment, Part I: Methodology. Building and Environment. 2009;44:651-6.

[114] Magnier L, Haghighat F. Multiobjective optimization of building design using TRNSYS simulations, genetic algorithm, and Artificial Neural Network. Building and Environment. 2010;45:739-46.

[115] Farlow SJ. Self-organizing methods in modeling: GMDH type algorithms: CRC; 1984.

[116] Ivakhnenko AG. Polynomial theory of complex systems. IEEE Transactions on Systems, Man and Cybernetics. 1971;SMC-1:364-78.

Appendix (A): Integration of a LHTES System with TRANSYS and Characterizations of Building Envelope

TRANSYS consists of two interfaces (i.e., TRNBuild and Studio). The TRNBuild interface is used to model the building's envelope and internal gains (i.e., the ventilation and heating modes). The building's description file is processed by the TRNBUILD program and then two files are generated that will be used by a Type 56 component during a TRNSYS simulation. The Studio interface composes of components (Types) that are used for the simulation. For example, input data is introduced into the first box that will use it for calculations and then produce an output data. That output data will then become the input data that will be introduced in the next box, and this process will continue until all the Types have been utilized.

Type 56 is used to simulate the selected building envelope. This type makes it possible to load an external file of the extension *.bui, thus allowing internal inputs to the studio interface. There is a flexibility to adjustment and accommodate the inputs made by user for the simulation. Several modes of building heat exchange are taken into account in this type.

Type 9A is used to recall weather data obtained from the National Climate Data and Information Archive, Canada. Type 16A reads the meteorological solar radiation in order to calculate its contribution on each surface of the building envelope. Type 34 is used to simulate thermal barriers such as caps, awnings or balconies. These are usually added to the sides where the incident rays are concentrated. Thus, both Back and Street

types are employed for the calculation of this type. The heights of the angles of these barriers are provided using an external file. Type 108 is a function of the indoor temperature that is calculated in the building. The assembly equation is used to connect all of the conditions. For instance, when the indoor temperature exceeds a certain value, windows are more likely to be opened. In addition, when the speed of wind exceeds a certain value, windows are kept closed.

Figure A.1 shows the flow chart of the types used for the simulation in Studio. Each group of types is connected and highlighted in a recognizable box. The orange box represents the thermal response function of the centralized LHTES system. The green box is the ventilation system, and the blue one is the building model. The brown box represents the outdoor data used in the simulation. The gray box is for the calculation of the indoor air humidity.

A weather file that provides the air conditions for July, 2011, in Montreal, Canada is identified. It consists of the air temperature in °C, relative humidity as a percentage %, the dew point temperature in °C, the wind direction, degree, and speed (m/s), the atmospheric pressure in Pa, and the total horizontal solar radiation, J/m².

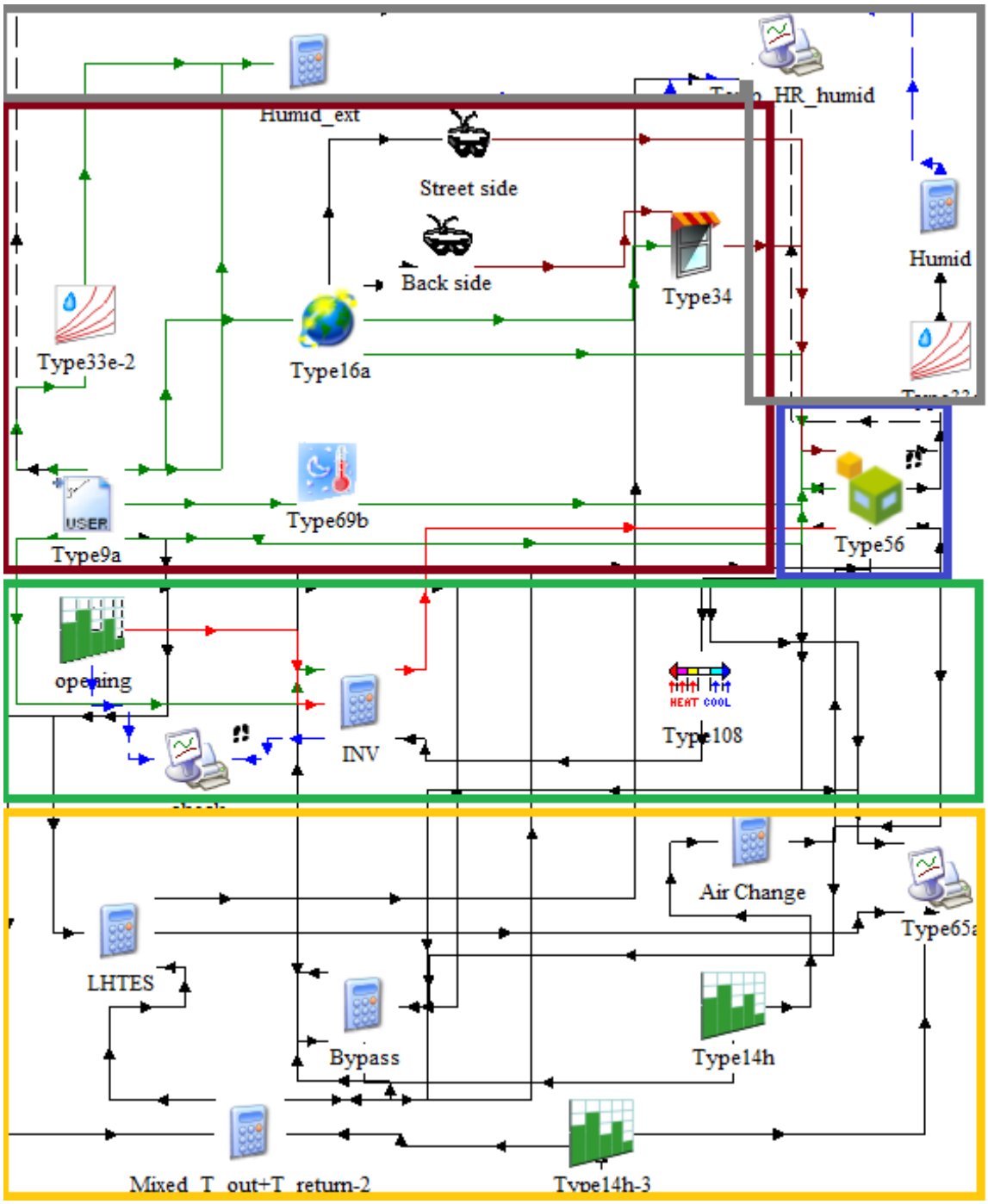

Figure A.1 Flow chart of the Types used for simulation in Studio

A.1 The building internal load

Internal heat gains in indoor air temperature and relative humidity contribute to a significant portion of the variation in building indoor air temperature and humidity. These are different from one dwelling to another depending on the habits of each building's occupants. According to the ISO standard 7730, a person sitting with moderate activity, produces about 120W of energy, and that same person generates 185W when doing more activity. Two persons are normally considered to be performing a moderate level of activity. In addition, appliances, such as computers, televisions, lights, refrigerators, etc. are taken into account based on the daily scheduled functions of normal activities.

A.2 Characterizations of building envelope

Attached wall
Inside
- plaster: 0.8 cm
- Horizontal slats + plaster - Ep: 1.2 cm (width: 2.5 cm spacing: 3.8 cm)
- Cleats: 2.5 cm (width: 2.5 cm - 28 cm spacing)
- Brick: 20 cm
- Cleats: 2.5 cm (width: 2.5 cm - 28 cm spacing)
- Horizontal + plaster boards: 1.2 cm (spacing: 3.8 cm)
- plaster: 0.8 cm

back

Interior floor
inside
- Wood floor: 3 cm
- Heavy wood joists: 30 cm (width: 7 cm - 40 cm spacing)
- Cleats: 2.5 cm (spacing: 28 cm)
- Slats + plaster: 1.2 cm (spacing: 3.8 cm)
- plaster: 0.8 cm

back

Roof
inside
- plaster: 0.8 cm

- Horizontal + plaster boards: 1.2 cm (spacing: 3.8 cm)
- Cleats: 2.5 cm (spacing: 28 cm)
- Heavy wood joists: 30 cm (spacing: 40 cm)
- Board: 2.5 cm
- Heavy wood joists: 45 cm (spacing: 40 cm)
- Board: 5 cm
- Coating bitumen: 1 cm

back

Internal wall

- plaster: 0.8 cm
- Horizontal + plaster boards: 1.2 cm (spacing: 3.8 cm)
- Vertical column: 6.4 cm (width: 4 cm - 28 cm spacing)
- Horizontal + plaster boards: 1.2 cm (spacing: 3.8 cm)
- plaster: 0.8 cm

Exterior wall

inside

- plaster: 0.8 cm
- Horizontal + plaster boards: 1.2 cm (spacing: 3.8 cm)
- Cleats: 2.5 cm (width: 2.5 cm - 28 cm spacing)
- Solid heavy wood: 7.5 cm
- Air gap: 2.5 cm
- Brick: 10 cm

back

Composite layers	Resistance [m².K/W]	Thickness [m]	Conductivity [kJ/h.m.K]
①Plaster + wood light	0.058	0.012	0.745
② Cleats + air	0.163	0.025	0.552
③ Joists + air 30 cm	0.219	0.300	4.937
④ Joists + air 45 cm	0.268	0.544	7.297
⑤ Amounts + air	0.170	0.064	1.355

Walls	Resistance [m^2.K/W]
Interior wall	0.332
Floor	0.594
Ceiling (roof)	0.902
Attached wall	2.366
Exterior wall	3.252

	% Material ①	% Material ②	Average density [kg/m3]	Capacitance medium [kJ/kg.k]
① Plaster + light wood	35 %	65 %	850	1.38
② Cleats + air	9 %	91 %	46	1.97
③ Joists + air 30 cm	20 %	80 %	131	2.39
④ Joists + air 45 cm	20 %	80 %	131	2.39
⑤ Amounts + air	14 %	86 %	71	1.98

Type of glazing	**Type of frame**
Double glazing U_g glazing = 2.79 W/m^2.K Solar factor g = 0.77	U_w frame wood = 2 W/m^2.K U_w insulated aluminum = 3 W/m^2.K $U_w$aluminium Profile = 4 W/m^2.K
Double window U_g glazing = 3.2 W/m^2.K Solar factor g = 0.60	
Single glazing U_g glazing = 5.73 W/m^2.K Solar factor g = 0.92	

Appendix (B): The SIMPLE Algorithm

This procedure is flourished by [97] for evaluating of flow filed. The name of SIMPLE stands for Semi-Implicit Method for Pressure-Linked Equations. The important operations can be summarized as following:

1- Guessing the pressure field p*.
2- Solving the momentum equations to obtain u*, v*, w*.
3- Solving the p' equation where p' is a correction pressure.
4- Calculating p by adding p' to p*.
5- Calculating u, v, and w from their starred values using the velocity−correction formulas.
6- Solving the discretization equation for other dependent variables, such as temperature, concentration, and turbulence quantities with source term.

Putting the corrected pressure p as a new guessed pressure p*, getting back to step 2, and repeating the entire procedure until a converged solution is achieved.

Appendix (C): A Code for Inlet Air-Temperature UDF

The following is a code used as user defined function (UDF) for implementing the inlet air-temperature based on hourly changes.

```
#include "udf.h"
real my_interpol()
{
        int i=0;
        int arr_no=168;
        real out_write;
        real time_min=CURRENT_TIME/60.0;
        real time_weather[]={0,60,120,180, 240};
        real temp_weather[]={288.85, 289.55, 289.05, 289.25, 287.25};
        while(time_weather[i]<time_min)
        {
                if(i==(arr_no-1))
                {
                        break;
                }
                else
                {
                        i+=1;
                }
        }
        out_write=temp_weather[i]+(temp_weather[i-1]-temp_weather[i])*(time_min-
time_weather[i])/(time_weather[i-1]-time_weather[i]);
        return out_write;
}
DEFINE_PROFILE(pressure_profile,t,i)
{
        face_t f;
        begin_f_loop(f,t)
        {
                F_PROFILE(f,t,i) = my_interpol();
        }
        end_f_loop(f,t)
}
```